

**REGIONAL-SCALE EVAPORANSPIRATION ESTIMATION  
USING VEGETATION INDEX AND SURFACE TEMPERATURE FROM  
NOAA SATELLITE AVHRR DATA**

**By**

**CHEN-HUNG TAN**

**A DISSERTATION PRESENTED TO THE GRADUATE SCHOOL  
OF THE UNIVERSITY OF FLORIDA IN PARTIAL FULFILLMENT  
OF THE REQUIREMENTS FOR THE DEGREE OF  
DOCTOR OF PHILOSOPHY**

**UNIVERSITY OF FLORIDA**

**1998**

Dedicated to my parents  
Chang-Ho and Min-Ho-Tae

## ACKNOWLEDGMENTS

First and foremost, I would like to express my sincere gratitude to my advisor, Dr. Sun-Fu Shih, for his guidance, support and patience. I am also thankful to Dr. Allen Orsman, Dr. George Snyder, Dr. Bruce Thomas and Dr. Byron Buhl for serving on my graduate committee.

I also greatly appreciate everyone at the Banning Sewerage Applications Laboratory who worked with me. Lab manager, Gabriela Lopez, was always there when I needed my certificate. Dr. Jonathan Jordan assisted in identifying Florida vegetation. Research assistants Leticia Chen, Chung-Chung Chen, and John Crisp, provided invaluable insight providing assistance. I would also like to thank the people who assisted with both the experiment and data collection. Maria Hsu and Deng Dyrnes of the St. Johns Water Management District set up the lysimeter experiment. Angela Chung and Brian Trickett of the South Florida Water Management District provided essential hydrological data, and Wayne Williams of the Agricultural and Biological Engineering Department generously made available his collection of detailed weather station data.

Finally, I thank my parents for their many years of love, support, and encouragement. I also wish to express my deepest gratitude to my wife, Yui Jung, not only for taking good care of our three daughters who arrived during my Ph.D. journey, but especially for always standing beside me through all the happiness and frustration.

## TABLE OF CONTENTS

|   | Page |
|---|------|
| ACKNOWLEDGMENTS                                 | ii   |
| LIST OF TABLES                                  | viii |
| LIST OF FIGURES                                 | x    |
| ABSTRACT  | xiii |
| CHAPTERS  |      |
| 1 INTRODUCTION                                  | 1    |
| 1.1 The Need for Regional ET Estimation         | 1    |
| 1.2 Statement of Problem                        | 2    |
| 1.3 Remote Sensing for ET Estimation            | 3    |
| 1.4 Research Objectives                         | 5    |
| 2 REVIEW OF LITERATURE                          | 6    |
| 2.1 Evapotranspiration Theory                   | 6    |
| 2.1.1 Physics of the Evapotranspiration Process | 6    |
| 2.1.2 Theoretical ET Estimation                 | 7    |
| 2.1.2.1 Energy balance approach                 | 7    |
| 2.1.2.2 Aerodynamic approach                    | 8    |
| 2.1.2.3 Continuum approach                      | 9    |
| 2.1.2.4 Early evaporation method                | 14   |
| 2.1.3 Potential ET and Reference ET             | 15   |
| 2.1.4 Crop Coefficients                         | 16   |
| 2.1.5 Evapotranspiration Studies in Florida     | 17   |
| 2.2 Remote Sensing Techniques and Capabilities  | 19   |
| 2.2.1 Field Spectroradiometry                   | 19   |
| 2.2.1.1 Spectral and spectral response curves   | 19   |
| 2.2.1.2 Spectral responses of vegetation        | 20   |
| 2.2.1.3 Spectral responses of soil and water    | 23   |

|         |  |    |
|---------|--|----|
| 3.2.1.4 | Field spectroradiometer measurements               | 29 |
| 3.2.2   | Vegetation indices                                 | 31 |
| 3.2.2.1 | Normalized difference vegetation index             | 32 |
| 3.2.2.2 | Difference vegetation index                        | 33 |
| 3.2.2.3 | Ratio vegetation index                             | 33 |
| 3.2.2.4 | Transformed vegetation index                       | 33 |
| 3.2.2.5 | Perpendicular vegetation index                     | 34 |
| 3.2.2.6 | Transformed vegetation index                       | 35 |
| 3.2.2.7 | Soil adjusted vegetation index                     | 36 |
| 3.2.3   | Thermal Remote Sensing                             | 37 |
| 3.2.3.1 | Pyrometry  | 37 |
| 3.2.3.2 | Surface temperature estimation                     | 41 |
| 3.2.3.3 | Single channel technique                           | 42 |
| 3.2.3.4 | Split window technique                             | 44 |
| 3.3     | Remote Sensing via ET Estimation                   | 47 |
| 3.3.1   | Empirical Method                                   | 48 |
| 3.3.2   | Simplified Energy Balance Method                   | 48 |
| 3.3.3   | Penman-Monteith Layer Method                       | 50 |
| 3.3.4   | Surface Parameterization Method                    | 50 |
| 3.3.4.1 | Surface albedo                                     | 51 |
| 3.3.4.2 | Surface roughness                                  | 52 |
| 3.3.4.3 | Soil Heat Flux                                     | 52 |
| 3.3.5   | Temperature and Vegetation Index Method            | 54 |
| 3.4     | Scale Consideration in Remote Sensing              | 55 |
| 3.4.1   | Spatial Temporal and Spectral Scales               | 55 |
| 3.4.2   | Optimum Spatial Resolution for Remote Sensing Data | 56 |
| 3.4.3   | Methods of Determining Optimum Scale               | 58 |
| 3.4.4   | Scale Selection for Regional ET Study              | 59 |
| 4       | METHODS AND MATERIALS                              | 60 |
| 4.1     | Field Spectroradiometry                            | 60 |
| 4.1.1   | Field Spectral Radiometer Measurements             | 60 |
| 4.1.2   | Normalized spectral comparisons                    | 62 |
| 4.1.3   | Selection of measuring bands                       | 62 |
| 4.1.4   | Comparison of Spectroradiometer and MODIS AVHRR    | 63 |
| 4.2     | Optimum Spatial Resolution                         | 63 |
| 4.2.1   | Image Resolution Degradation                       | 64 |
| 4.2.2   | Adams Local Coefficients of Variance               | 66 |
| 4.3     | MODIS AVHRR Data Collection and Processing         | 67 |
| 4.3.1   | MODIS TIGRIS V3 Routines                           | 67 |
| 4.3.2   | Processing of Satellite Data                       | 71 |
| 4.3.2.1 | Image and Data Extraction                          | 76 |

|         |  |     |
|---------|--|-----|
| 3.3.2.1 | Geometric Rectification and Geo-referencing                | 88  |
| 3.3.2.2 | Cloud Removal  | 89  |
| 3.3.3   | AVHRR Data Calibration                                     | 94  |
| 3.3.3.1 | Visible Channel Calibration                                | 95  |
| 3.3.3.2 | Thermal Channel Calibration                                | 97  |
| 3.4     | Regional ET Estimation Model                               | 99  |
| 3.4.1   | Revised ET by Surface Temperature Method                   | 99  |
| 3.4.2   | Relationship of Vegetation Index and Surface Temperature   | 99  |
| 3.4.2.1 | NDVI-DSTV relationship from field measurement              | 99  |
| 3.4.2.2 | NDVI-DSTV relationship from satellite data                 | 99  |
| 3.4.3   | ET Estimation from NDVI-DSTV Triangle                      | 99  |
| 3.4.4   | Geographic Information System                              | 100 |
| 3.5     | Model Verification   | 101 |
| 3.5.1   | Verification with Traditional ET Methods                   | 102 |
| 3.5.2   | Verification with Lyman ET                                 | 105 |
| 4       | RESULTS AND DISCUSSION                                     | 109 |
| 4.1     | Spectral Response  | 109 |
| 4.1.1   | Spectral and Cross Spectral Comparison                     | 109 |
| 4.1.1.1 | Normalized spectral comparison                             | 109 |
| 4.1.1.2 | Selection of discriminating bands                          | 114 |
| 4.1.1.3 | Spectral comparison  | 120 |
| 4.1.2   | Comparison of Spectral Characteristics and NOAA AVHRR      | 120 |
| 4.1.2.1 | Comparison of spectral bands and vegetation indices        | 120 |
| 4.1.2.2 | Comparison of correlations among derived bands             | 122 |
| 4.1.3   | Florida Vegetation Reflectance Database                    | 122 |
| 4.2     | Optimal Spatial Resolution                                 | 124 |
| 4.2.1   | Image Resolution Degradation                               | 124 |
| 4.2.2   | MLCV of Near Infrared Images                               | 124 |
| 4.2.3   | MLCV of Thermal Images                                     | 127 |
| 4.2.4   | MLCV and Optimum Spatial Resolution                        | 127 |
| 4.2.5   | Comparison of Near Infrared and Thermal Optimal Resolution | 132 |
| 4.3     | Regional Evapotranspiration Estimation                     | 137 |
| 4.3.1   | Field Temperature and NDVI Measurement                     | 137 |
| 4.3.2   | Image Processing of NOAA AVHRR                             | 137 |
| 4.3.3   | Processed ET at Optimal Spatial Resolution                 | 140 |
| 4.3.4   | NDVI and DSTV Triangle                                     | 140 |
| 4.3.5   | Regional ET Estimation                                     | 144 |
| 4.3.6   | Verification   | 147 |
| 4.3.6.1 | Verification with traditional ET methods                   | 147 |
| 4.3.6.2 | Verification with Lyman ET                                 | 148 |
| 4.3.7   | Regional ET in South Florida                               | 152 |

|   |     |
|---|-----|
| 1. CONCLUSION, AND FUTURE RESEARCH                          | 163 |
| 1.1 Conclusion  | 163 |
| 1.2 Recommendations for Further Research                    | 167 |
| APPENDICES  | 169 |
| 1. SPECTRUM REFLECTANCE CURVES FOR FLORIDA VEGETATION       | 169 |
| 2. SOURCE CODE FOR AVHRR DATA AND IMAGE PROCESSING          | 181 |
| 3. ALGORITHM AND SOURCE CODE FOR TRADITIONAL ET CALCULATION | 214 |
| REFERENCES  | 229 |
| GEOGRAPHICAL SKETCH   | 240 |

# LIST OF TABLES

| Table  | Page |
|--|------|
| 2.1 The multi-spectral reflectance and vegetation characteristics and their relationship in vegetation indices | 28   |
| 2.2 Equations for Tassled Cap transformation combinations  | 36   |
| 2.3 Split window formula for surface radiant temperature correction  | 62   |
| 2.4 Spatial, temporal and spectral coverages of Landsat, SPOT, ODES and NOAA satellites                        | 67   |
| 3.1 Spatial band, wavelength, spectral features, and ground resolution of Landsat Thematic Mapper              | 68   |
| 3.2 NOAA/AVHRR spatial coverage  | 69   |
| 3.3 NOAA/AVHRR orbit, ground coverage, and sensor characteristics  | 76   |
| 3.4 Data, acquisition time and orbit number of the NOAA AVHRR data   | 77   |
| 3.5 Format of SNOT data-physical record  | 86   |
| 3.6 Water temperature stations used in collection of marine surface temperature                                | 87   |
| 3.7 Extent of values assigned for the land surface cover classes in Florida                                    | 93   |
| 3.8 The seven land cover classes and locations of classes used in the mapping system                           | 94   |
| 3.9 Vegetation Maturity Coefficient (VMC) for agriculture, wet soil and dry soil conditions in south Florida   | 105  |
| 3.10 Land cover type and the assigned actual to potential ET ratio for each weather station                    | 107  |



|      |  |     |
|------|--|-----|
| 4.1  | Spectral difference of initial and average at 4 wavelength intervals at four dates. Test statistics were in parenthesis. Difference were calculated as average reflectance subtracted by initial reflectance.                                  | 108 |
| 4.2  | Normalized spectral difference of initial and average at 4-wavelength intervals at four dates. Test statistics were in parenthesis. Difference were calculated as normalized average reflectance subtracted by normalized initial reflectance. | 109 |
| 4.3  | Spectral responses of red (RDI) and near infrared (NIR) bands and the simulated vegetation indices by field radiometer and NOAA-AVHRR at Fort Drum marsh.  | 120 |
| 4.4  | Correlation analysis between spectroradiometer and NOAA-AVHRR spectral bands and derived vegetation indices. Data were calculated from measurements of average, initial and water at four dates.   | 122 |
| 4.5  | Size, location, mean and standard deviation (SD) for the selected urban, agriculture, wetland and mature land cover/cover types.   | 128 |
| 4.6  | Mean Local Coefficient of Variance (mLCV) for near infrared band for urban, agriculture, wetland, and mature land cover/cover. Bold number indicates peak value location.  | 128 |
| 4.7  | Mean Local Coefficient of Variance (mLCV) for thermal band for urban, agriculture, wetland, and mature land cover/cover. Bold number indicates peak value location.  | 130 |
| 4.8  | Field measurement of surface temperature and vegetation index for locally selected ground objects.   | 133 |
| 4.9  | Coefficients A and B of the energy balance equation, and the coefficient of determination ( $r^2$ ) from the regression analysis of $EO1$ vs $(A_e/ET)$ .  | 143 |
| 4.10 | $EO1$ , $NDVI$ and weighting factors for the eight selected land cover/cover.  | 155 |
| 4.11 | Eysenator recorded ET and remote sensing estimated ET for wetland marsh areas at four days.  | 160 |
| 4.12 | Eysenator recorded ET and remote sensing estimated ET for natural marsh at four days.  | 160 |

## LIST OF FIGURES

| Figure |  | Page |
|--------|--|------|
| 2.1    | Spectral reflectance curves of vegetation, soil and water in the visible, near infrared and middle infrared portions of EM radiation.  | 11   |
| 2.2    | Quantified diagram of a leaf's structure and its reflective characteristics at visible and near IR wavelengths.  | 13   |
| 2.3    | Average spectral response curves for a plant/leaf at six progresses from a healthy state through different stages of damage (from Martinis, 1973)  | 14   |
| 2.4    | Typical soil reflectance curves for five major types of curves. Types 1-3 were proposed by Condit (1972) and types 4 and 5 by Sauer and Baumgardner (1984)   | 17   |
| 2.5    | Viewing geometry for the bidirectional reflectance measurements in the field measurement. $\theta_i$ and $\theta_r$ are incident and reflected zenith angles, located in the vertical plane; $\phi_i$ and $\phi_r$ are incident and reflected azimuth angles, located in the horizontal plane.                                 | 30   |
| 3.1    | Locations of the four selected landscapes/covers: letter A stands for agricultural area (sugarcane and vegetable fields in Everglades Agricultural Area), W for wetlands (Everglades National Park and Water-Conservation Area), U for urban (residential area in west Fort Lauderdale), and dotted line for the mixture area. | 43   |
| 3.2    | Schematic diagram of INLCT. The INLCT is measured as the mean value of the coefficient of variance of a 3x3 pixel window moving across the image.  | 44   |
| 3.3    | Spectral response curves for NOAA-14 AVHRR channel 1   | 71   |
| 3.4    | Spectral response curves for NOAA-14 AVHRR channel 2   | 73   |
| 3.5    | Spectral response curves for NOAA-14 AVHRR channel 3   | 75   |

|      |  |     |
|------|--|-----|
| 3.6  | Spectral response curve for NOAA-AVHRR channel 4   | 78  |
| 3.7  | Spectral response curve for NOAA-AVHRR channel 3   | 79  |
| 3.8  | Schematic diagram of NOAA-AVHRR data preprocessing procedures  | 79  |
| 3.9  | The hypothetical triangle slope that would result from the relation between vegetation index and thermal surface temperature difference                          | 95  |
| 3.10 | Relationship of vegetation and moisture coefficient (VMC) from the three corner points (vegetation, wet land, and dry land) of the NDVI-DSTV triangle            | 96  |
| 3.11 | Boundary of the South Florida Water Management District study area and location of the ground meteorological stations  | 104 |
| 3.12 | Location of SCT experimental site in the Fort Drum Marsh, Holmes River County, Florida. Background coverage is 1993 black and white SPOT panchromatic imagery    | 107 |
| 3.13 | Swamp vegetation/vegetation boundary in the Fort Drum marsh experimental site. Photo shows swampy land with automatic water level gauge and the background marsh | 108 |
| 4.1  | Reflectance curves of cattail and swamp in the spectral wavelength from 350 nm to 1100 nm in Oct. 75, 1994   | 109 |
| 4.2  | Reflectance curves of cattail and swamp in the spectral wavelength from 350 nm to 1100 nm in Dec. 23, 1994   | 111 |
| 4.3  | Reflectance curves of cattail and swamp in the spectral wavelength from 350 nm to 1100 nm in Mar. 28, 1997   | 112 |
| 4.4  | Reflectance curves of cattail and swamp in the spectral wavelength from 350 nm to 1100 nm in May 14, 1997  | 113 |
| 4.5  | Normalized reflectance curves of swamp (Cochlosia paniculata) at four dates. Note that the curves are almost identical curves except in five spectral regions    | 113 |
| 4.6  | Normalized reflectance curves of cattail (Typha domingensis) at four dates. Note that the curves are almost identical curves except in five spectral regions     | 114 |

- 4.7 The normalized reflectance curves of sugarcane (*Colossium giganteum*) and wheat (*Triticum dicoccum*) are shown for different times of the year 107
- 4.8 Landsat TM images at four levels of spatial-resolution degradation. Images show a residential area west of Fort Lauderdale at 128 m (a), 500 m (b), 600 m (c), and 900 m (d) resolution 109
- 4.9 Graphs of NLCTV for the near infrared band as a function of spatial resolution for urban, agricultural, wetland, and mixture areas. As the peaks of the graphics showed, the best spatial resolution for urban, agricultural, and wetland are 60 m, 300 m and 1200 m, respectively 120
- 4.10 Graphs of NLCTV for the thermal band as a function of spatial resolution for urban, agricultural, wetland, and mixture areas. As the peaks of the graphics showed, the best spatial resolution for urban, agricultural, and wetland are 300 m, 450 m and 1100 m, respectively 121
- 4.11 Mean Local Coefficient of Variance (NLCTV) of the near infrared and thermal bands for urban land use/cover. Peaks of the near infrared and thermal bands are located at 60 and 300 m, respectively 123
- 4.12 Mean Local Coefficient of Variance (NLCTV) of the near infrared and thermal bands for agricultural land use/cover. Peaks of the near infrared and thermal bands are located at 300 and 450 m, respectively 124
- 4.13 Mean Local Coefficient of Variance (NLCTV) of the near infrared and thermal bands for wetland land use/cover. Peaks of the near infrared and thermal bands are located at 1200 and 1400 m, respectively 125
- 4.14 Mean Local Coefficient of Variance (NLCTV) of the near infrared and thermal bands for mixture land use/cover. Peaks of the near infrared and thermal bands are located at 300 and 600 m, respectively 126
- 4.15 Spectral reflectance curves for select of ground objects (asphalt, concrete, bare soil, grass, cabbage, water with 50 vegetation cover, water with 30% vegetation cover and water with 2% vegetation cover) as measured by hand-held radiometer 129
- 4.16 Raw NOAA AVHRR image of December 9, 1994 with state boundary as the background. The image is geometrically distorted due to scan skew and earth rotation 140

|      |   |     |
|------|---|-----|
| 4.17 | Orizontally rotated NOAA AVHRR image of December 9, 1996  | 142 |
| 4.18 | Normalized difference-vegetation index derived from NOAA-14 AVHRR image for December 9, 1996  | 143 |
| 4.19 | Land surface temperature derived from NOAA-14 AVHRR image for December 9, 1996  | 146 |
| 4.20 | Relationship of the difference between wet radiance and evapotranspiration ( $R_w - ET$ ) and the surface-to-air temperature relation ( $T_s - T_a$ ) on 11 Apr. 1997   | 147 |
| 4.21 | Simulated ET from the linear relationship between $R_w - ET$ and $R_w - ET_s$ versus ET calculated from ground-measured meteorological data for 4 dates   | 148 |
| 4.22 | NDVI and surface temperature relationship for the selected ground objects measured at field   | 150 |
| 4.23 | NDVI and diurnal temperature difference ( $T_d - T_n$ ) relationship for the selected ground objects measured at field  | 151 |
| 4.24 | NDVI and surface-air temperature difference ( $T_s - T_a$ ) relationship for the selected ground objects measured at field  | 152 |
| 4.25 | Satellite-derived normalized difference-vegetation index (NDVI) versus derived surface temperature difference ( $R_w - ET$ ) for seven land surface/cover types: Agriculture, urban, and marsh are the three corners of the NDVI- $R_w - ET$ triangle | 153 |
| 4.26 | Satellite-derived and ground-based data layers and the calculation of ET in the geographic information system   | 156 |
| 4.27 | ET estimated by the remote sensing method versus ET estimated by the traditional (Penman) method on the five days: ET values at the Ft. My. Bay weather station (BITE) on the five dates were identified  | 159 |
| 4.28 | Contour map of regional ET in south Florida by remote sensing method on May 26, 1997  | 161 |
| 4.29 | Contour map of regional ET in south Florida by interpolation of traditional ET method on May 26, 1997   | 164 |

*Abstract of Dissertation Presented to the Graduate School  
of the University of Florida in Partial Fulfillment of the  
Requirements for the Degree of Doctor of Philosophy*

**REGIONAL SCALE EVAPOTRANSPIRATION ESTIMATION  
USING VEGETATION INDEX AND SURFACE TEMPERATURE FROM  
NOAA SATELLITE AVHRR DATA**

**By**

**Chih-Hung Tsai**

**May 1992**

**Chairman: Dr. Ron F. Sklar**

**Major Department: Agricultural and Biological Engineering**

Measurement of the water vapor deficit of the land surface is critical to improving the management of the limited fresh water resources. Despite the importance of evapotranspiration in the hydrologic cycle, its magnitude, spatial and seasonal distributions, and its relation to environmental variables remains relatively unknown. In the state of Florida, evapotranspiration (ET) is second only to precipitation in magnitude within the hydrologic budget.

This research begins with the examination of the spatial response of surface objects in Florida by the use of a land field indicator. The relationship between the field indicator and satellite remote sensing data was then examined. The optimum spatial correlation between the fine scale indicator and the coarse scale satellite data was

also explained. Surface temperature and vegetation index were extracted from the NOAA satellite AVHRR data. The concept of a Normalized Difference Vegetation Index (NDVI) and Global Surface Temperature Variation (GSTV) triangle was introduced, based on the pattern of ground objects located in the NDVI-GSTV scattergram. The NDVI-GSTV triangle relationship was used to calculate the vegetation-soil moisture coefficient (VMC), for fractional contribution from various vegetation cover and soil moisture backgrounds. A geographic information system (GIS) was utilized to merge the satellite and ground-based data. Regional ET was then estimated from the data layers in the GIS.

Results from the land-land-atmosphere study indicate that spectral response can be used to determine the most appropriate spectral bands and reason for vegetation discrimination. Correlation study of satellite and weather observations indicates that they relate to each other most strongly in the frames of vegetation index. As to satellite imagery, to identify the best use activities for optimum spatial correlation at 680 nm and 860 nm for infrared and thermal bands, respectively. The conceptual NDVI-GSTV triangle was successfully verified with both ground and satellite observations and the relationship of NDVI-GSTV determined the fractional contribution from agriculture, wet and dry soil surfaces. Formulas for calculated VMC clearly displayed the fractional contributions of crop coefficients from vegetation, wet and dry soils. Results of ET estimation show that the algorithm did provide an efficient method for mapping the spatial variations in ET and making useful estimates of ET in south Florida.

## CHAPTER 1 INTRODUCTION

**Evapotranspiration (ET)** is the process by which water is transferred from the earth's surface into the atmosphere. It includes evaporation from soil and water surfaces and transpiration from vegetation. On land surfaces, about 60% of the precipitation received is expended through ET (Poston et al., 1986). Along with rainfall and runoff, it controls the availability of water at the earth's surface and directly affects human habitation and activities. Quantification of ET in the hydrologic budget, therefore, is essential when planning for the development of water resources of an area, estimating water supply potential, and understanding the ecological effects of development. In Florida, hydrologic studies have demonstrated that ET is second only to precipitation in magnitude within the hydrologic budget (Jones et al., 1984). Evapotranspiration can vary considerably among basins that contain different types of vegetation cover or different proportions of open water surfaces. Demands for water supply in Florida continue to increase, lowering the status of hydrologic budgets in areas where water supplies are being developed creates uncertainty (Bellido et al., 1990).

### 1.1 The Need for Regional ET Estimation

*Development of water resources for agricultural or other uses normally involves*



models on a regional scale. Hydrological modeling is often done on a scale which involves the analysis of ET from a region. Rosen (1983) reported that the need for measurement of ET over large areas has been a growing concern as efforts to test environmental models on global scales are intensified. ET patterns at a regional scale integrate factors such as change in land use, rainfall distribution and differences. The need to measure ET at a regional scale is increasing, and is an important matter in studies of global change (Curtis and Eddy, 1994).

### 1.2. *Estimation of Evapotranspiration*

Numerous equations on the basis of data from weather stations or ground measurements have been developed to estimate ET rates over the last fifty years (Penman, 1948; Tinsley and Polson, 1960; Blaney and Criddle, 1944; Penman et al., 1967; Christiansen, 1944; Rose et al., 1972). When applied to regional evapotranspiration estimates, most of these techniques, however, have been of limited usefulness for three reasons. First, they have been dependent on surface parameters that are difficult to measure over an extended area. Secondly, they provide point estimates. That is, these estimates are only applicable over a homogeneous area surrounding the location where the parameters were measured. The results may not actually apply to large heterogeneous areas. Thirdly, many estimated ET methods provide potential ET or reference ET, i.e., the ET with unlimited water supply, which is not the ground case. They have to depend on coefficients related to crop type or surface conditions to estimate actual ET. In regional scheduling, the concept of crop coefficients ( $K_c$ ) has been widely used to obtain

reference ET to crop ET. However, the application of crop coefficients on regional scale has several difficulties. For example, coefficients for natural vegetation cover, such as hardwood forest, coastal marsh, or cypress swamp, as opposed to field crops, are virtually constant due to the diverse, uncontrolled environment. Furthermore, crop coefficients are not constants. They change with crop growing stage and location of application. Even with the all-crop coefficients, it is still difficult to determine the ratio between reference ET and actual ET for an area with various vegetation growing at different stages. Despite the substantial and documented progress in ET estimations, as Hoopes et al. (1988) pointed out, the problem of estimating regional ET, as opposed to point ET, still represents a major research deficiency.

### 1.1 Remote Sensing for ET Estimation

Since the beginning of Earth remote sensing from satellites, remotely sensed observations of the Earth's surface have provided a promising source of data for examining the characteristics over land surfaces. Hydrologists and agricultural meteorologists have been searching for techniques to calculate regional evapotranspiration from data provided by satellites. Wilson et al. (1987) suggested that the only feasible means of mapping the spatial distribution of ET on a regional scale is to use remotely sensed data from satellite based sensors.

The foundation of satellite remote sensing is based on the knowledge of the spectral responses from objects on the ground. Spectral measurements using spectral radiometers are of crucial importance to remote sensing, both at the level of primary

research and operational applications. For vegetation property research as is well as the interpretation of satellite data, relationships must be developed between satellite sensed data and field measured spatial data. However, relationships between field spatial measurements and satellite remote sensing are still a topic to be explored, mainly because of the species mixing problem and the observational scale difference (i.e., fine resolution, small coverage in measurement data versus resolution, large coverage in satellite data). Field measurement measurements, while being close to the subject, are still a measure of the spectral response over the field of view of the instrument. In satellite remote sensing, the digital number of each image pixel element (pixel) is an aggregation of all responses from objects within the resolution area/footprint of the resolution of the satellite sensor. This leads to a question of spatial resolution of satellite data. Does there exist an optimal spatial resolution for detecting the characteristics on the ground for the subject area we wish to measure? In this study, the optimal ET as of interest and the optimal spatial resolution of the relevant optical and thermal property from each major land use/cover is derived.

Surface temperature and vegetation index are two of the most important surface parameters that can be obtained from the thermal and optical portions of satellite remote sensing, respectively. However, the relationship of surface temperature and vegetation index with respect to land cover/use has not been extensively studied. These two parameters are respectively correlated to the moisture availability and the vegetation condition which are the most important and difficult surface factors to be measured in the

**ET process:** Price (1996) reported that there is no advantage to using a sophisticated correlation model for ET estimation if the surface parameters required are not available for the region. The difficulties prompt the need to develop a simple algorithm for regional ET estimation.

#### 1.4. Research Objectives

The objectives of this study are therefore: 1) to study the field evapotranspiration and the linkage between field-spatial measurements and satellite remote sensing, 2) to find an optimum spatial resolution of remotely sensed data that can be used for regional scale studies in Florida, and 3) to study the relationship of vegetation index and surface temperature and use the satellite-derived NDVI and LSTV for regional scale ET estimation in Florida.

## CHAPTER I REVIEW OF LITERATURE

The study of regional ET using satellite remote sensing included at least three major disciplines: 1) evapotranspiration theory; 2) remote sensing theory and methods, and 3) satellite image processing techniques. The review of literature begins with the key concepts of the ET process and traditional methods of ET estimation. ET characteristics of Florida were also reviewed. Remote sensing theory from field radiometry to satellite image processing techniques was reviewed. Spectral characteristics of vegetation and soil, and the theory of optical and thermal remote sensing were then studied. The primary parameters that can be derived from remote sensing, vegetation index and surface temperature, were then introduced as a link between the ET estimation methods and remote sensing techniques. Early works of remote sensing methods for ET estimation were also studied. Finally, the wide consideration in remote sensing was also reviewed.

### 1.1 Evapotranspiration Theory

#### 1.1.1 Physics of the ET Process

ET includes evaporation from soil and free water surfaces as well as transpiration from photosynthetically active vegetation. Evapotranspiration from land surfaces is the result of several coupled processes including radiative exchanges, vapor transport, and

biological growth operating within a system involving the atmosphere, plants, and soil. There are three main factors that influence the process of ET. They are the supply of energy to provide the latent heat of vaporization, the supply of moisture at the evaporative surface, and the ability to transport the vapor away from the evaporative surface.

### 11.2 Traditional ET Estimation

Since the 1960s, a significant amount of research effort has been devoted to the study of ET. The various methods that have been used to estimate ET can be grouped into four broad categories: energy balance approach, aerodynamic approach, combination approach and instrument measurement (ddy correlation method).

#### 11.2.1 Energy balance approach

Evaporation and transpiration require a large amount of energy at the earth-atmosphere interface. Solar radiation usually supplies 80 to 90 percent of this energy and provides the basis for using ET. Hence, energy budget is one of the earliest methods used to estimate evaporation. The energy balance equation, in general form, can be expressed as

$$R_n = LE + H + G = P + A_n + \frac{\partial M}{\partial t} \quad (2.1)$$

where  $R_n$  = specific flux of net incoming radiation

$LE$  = latent heat of evapotranspiration,

$H$  = sensible heat flux from the surface to the atmosphere,

|                 |   |   |
|-----------------|---|---|
| $Q_{net}$       | = | specific flux of heat conducted into the earth,                                 |
| $P$             | = | energy flux stored as physicochemical energy in the products of photosynthesis, |
| $A_h$           | = | energy advection into the layer as specific flux,                               |
| $\frac{dH}{dt}$ | = | the rate of energy storage per unit area in the layer                           |

The exact form of several of the terms depends on the type of vegetation and time for which the energy balance is described. In many practical applications, especially over land surfaces, the terms  $P$ ,  $A_h$ , and  $dH/dt$  are of little consequence, so that Equation 2.1 assumes a much simpler form. The energy balance equation, after simplification, can be expressed as

$$R_n = Q_{net} + H + G \quad (2.2)$$

If the net incoming radiation, sensible heat flux, and ground heat flux can be measured or estimated, the evapotranspiration can be solved as

$$E = (R_n - H - G)/\lambda \quad (2.3)$$

in this formula,  $\lambda$  is the latent heat of vaporization. Equation 2.3 is called the energy balance equation for evapotranspiration.

### 2.1.2 Aerodynamic approach

Evapotranspiration can also be determined by calculating the ability to transport water vapor away from the land or vegetation surfaces. The transport rate is governed by the boundary gradient at the air near the surface and the wind speed across

the coefficient using the equation developed by Thornthwaite and Holzman (1939)

$$E = \frac{(\rho_a k^2 / \rho_a) (q_s - q_a) (q_s - q_a)}{[\ln(\rho_a / \rho_a)]^2} \quad (2.4)$$

where

- $k$  = von Karman constant, usually taken as 0.4,
- $\rho_a$  = density of air,
- $q_s$  = specific humidity, and
- $u$  = wind speed (measured at height  $z$ ).

### 3.1.3.2 Continuity approach

Evaporation may be computed by the aerodynamic method when there is enough energy supply and by the energy budget method when vapor transport is not a limiting factor. However, under normal conditions, both factors are limiting, so a method considering both factors is required (Thorn et al., 1988). Since the atmospheric transport mechanisms of sensible heat are similar to those of water vapor, Burrows (1928) assumed that the sensible heat flux and the latent heat flux are proportional, and the proportionality constant being called the Bowen ratio

$$B = \frac{H}{\lambda E} \quad (2.5)$$

When net radiation  $R_n$  and ground heat flux  $G$  are known, the evaporation rate can be written as a combination of the energy budget equation and the Bowen ratio



$$E = \frac{(E_2 - E_1)}{\Delta t - \beta \Delta t} \quad (2.6)$$

The value of  $\beta$  can be calculated from  $q$  values if air temperature and vapor pressure above the evaporating surface by vapor and momentum transport equations expressed as

$$E = -\rho_a E_v \frac{dq_a}{dt} \quad (2.7)$$

$$E = -\rho_a C_p E_s \frac{dT}{dt} \quad (2.8)$$

where

$\rho_a$  = density of air,

$E_v$  = vapor eddy diffusivity,

$q_a$  = specific humidity,

$T$  = temperature,

$C_p$  = specific heat at constant pressure, and

$E_s$  = heat diffusivity

Using measurements of  $q_a$  and  $T$  made at two levels  $z_1$  and  $z_2$ , the Bowen ratio is written as

or

$$\beta = \frac{C_p E_s (\bar{T}_1 - \bar{T}_2)}{L_v E_v (\bar{q}_1 - \bar{q}_2)} \quad (2.9)$$

By substituting  $5.423(y/z)$  for  $q_a$  and separating constants, the expression for the

Brown ratio becomes

$$\beta = \gamma \left( \frac{T_1 - T_2}{\tau_1 - \tau_2} \right) \quad (2.10)$$

where  $\gamma$  is also called the psychrometric constant

$$\gamma = \frac{C_p K_a P}{0.622 \Delta E_a} \quad (2.11)$$

and the ratio  $K_a$  and  $K_v$  of the heat and vapor diffusion is commonly taken as the 1 (Prestley and Taylor, 1955).

To determine Brown ratio  $\beta$ , measurements of temperature and vapor pressure are required at two different heights. A very important step in Papadakis analysis (Papadakis, 1981) is that he defines a gradient  $A$  of the outdoor water vapor pressure curve,

$$A = \frac{e_s^* - e_a^*}{T_s - T_a} \quad (2.12)$$

where  $e_s^* = e^*(T_s)$  is the corresponding saturation vapor pressure at air temperature  $T_s$  and  $e_a^* = e^*(T_a)$  is the vapor pressure at the wet surface. Since  $e_s > e_a$  for a saturated surface, the Brown ratio is expressed as

$$\beta = \frac{1}{A} \left( \frac{T_1 - T_2}{\tau_1 - \tau_2} \right) \quad (2.13)$$

Substitution of Equation 2.11 in Equation 2.13 yields

$$E_a \approx \left(1 + \frac{T_a}{20}\right) E - \frac{E}{h} \left( \frac{E_a - E_a^*}{E_a - E_a^*} \right) E \quad (2.11)$$

A bulk mass transfer equation can be used in the second term of E,

$$E = f(\bar{u}) (q_s - q_a) \quad (2.12)$$

where  $f(\bar{u})$  is a wind function. The Janke-Prandtl equation,

$$E_a E = \frac{h}{h+1} (E_a - E) + \frac{T_a}{h+1} E_a \quad (2.13)$$

where  $E_a$  is an aerodynamic term related to the drying power of air, defined by

$$E_a = E_a f(\bar{u}) (q_s - q_a) \quad (2.14)$$

Prandtl's equation combined the features of energy balance and aerodynamic and Equation 2.11 is the subject of numerous theoretical and experimental studies. The main feature in Prandtl's analysis is that it requires measurements of temperature, mean specific humidity, and wind speed at one height only. For this reason, it is very useful when measurements at several levels is needed for profile methods or when standard energy budget methods are unavailable or unsuited.

The combination equation derived by Prandtl was used to describe the evaporation from an open water surface or from short green vegetation easily supplied with water (potentially transpiring). A chief assumption of the method is that the vapor pressure at the surface is saturated so that the saturated vapor pressure curve and the gradient  $\Delta$  in Equation 2.11 can be applied. However, even when it is well supplied

with water at the roots, in general, an vegetation surface cannot be considered wet except after rainfall or dew formation (Beynon 1962). Thus, the specific humidity at the surface of the foliage is somewhat smaller than the saturation value at the corresponding temperature and Penman's equation is no longer applicable. The lack of generality in Penman's equation was satisfactorily corrected by Monteith (1965) who combined energy balance, aerodynamics and surface processes in an evaporation equation formally valid for vegetation of any type in any state of water stress. In Monteith's approach, the surface specific humidity  $q_s$  was replaced by the saturation value at the stomatal conductance of the foliage elements and a bulk stomatal resistance was introduced to characterize the transfer between the stomatal conductance and the leaf surface. When the vegetation is not actually wet, the surface vapor pressure  $e_s$  is not equal to  $e_s^*$ . However, they can be related by

$$(q_s - q_a) = \left( \frac{z_d}{z_s + z_a} \right) (q_s^* - q_a) \quad (2.16)$$

where  $e_s$  is the actual vapor pressure at the  $z_s$ ,  $z_s$  is the diffusion resistance of an layer, and  $z_a$  the aerodynamic resistance. Using this equation, instead of Equation 2.12 as the Bowen ratio, and substituting into Equation 2.14, one obtains

$$LE = \frac{R_n}{R_n + \gamma} (R_n + \gamma) \frac{P(e_s^* - e_a)}{z_s + z_a} \quad (2.17)$$

with

$$r' = \gamma \left( 1 + \frac{z_s}{z_a} \right) \quad (2.18)$$

|                |   |
|----------------|---|
| where $\delta$ | = change of sensible vapor pressure with temperature, |
| $\gamma$       | = psychrometric constant,                             |
| $\rho$         | = density of air                                      |
| $q_s$          | = specific heat of air at constant pressure           |
| $r_s$          | = aerodynamic resistance,                             |
| $r_a$          | = surface resistance of vegetation                    |

This equation, commonly called the Penman-Monteith equation (Monteith, 1973), not only considers thermodynamic and aerodynamic aspects, but also includes the aerodynamic resistance to sensible heat and vapor transfer, and the surface resistance to vapor transfer. The aerodynamic resistance describes the effect of the physical roughness of the evaporating surface on the transfer of energy and mass to atmosphere. The surface resistance, which is primarily related to the bulk stomatal resistance (Thom, 1975), describes the biological control over the rate of transpiration. Brutsaert (1982) also indicated that when this concept is used as the control of ET over dry soil it may also account for the resistance through the upper layer of the soil.

#### 3.1.1.4 Edley correlation method

The eddy correlation is a direct measurement of mass transfer that requires complex instrumentation and well trained personnel to obtain accurate results (Turner et al., 1981). The mass vertical flux of water vapor based on the eddy flux theory, is written as:

$$E = \frac{6.8125}{P} \bar{\rho} \bar{w}^2 z \quad (2.27)$$

where  $E$  = evaporation in mm/hr. density,

$P$  = atmospheric pressure;

$\bar{\rho}$  = air density,

$\bar{w}$  = instantaneous deviation of vertical wind speed from the mean vertical wind at height  $z$ , and

$\bar{p}$  = instantaneous deviation of the partial water vapor pressure from the mean vapor pressure at height  $z$ .

The instruments required for the eddy correlation method are a vertical anemometer for  $w$ , and vapor pressure sensor for  $e$ . The eddy correlation method is feasible for field use in remote measurements with adequate funds (Rosenberg et al., 1980; Warner et al., 1985). Feasible is adequate if there is sufficient upward homogeneity in the vegetation cover so that the surface layer equilibrates with the vegetation cover from ground surface to at least the height of the instrument. This upward distance generally is considered to be about 100 times the instrumentation height (Warner, 1985).

### 2.2.1 Potential ET and Reference ET

Potential ET is defined as the quantity of water evaporated from an extensive free water surface no restricted by existing atmospheric conditions (Monteith, 1957). A concept similar to potential ET is reference ET. Reference ET is definition ET from a well watered reference crop maintained at a given standard height. Therefore, potential

ET can be defined exclusively from meteorological conditions, while reference ET is dependent on the reference crop selected. Typically grass is used as the reference crop. However, other crops, such as alfalfa, have also been used (Jensen et al., 1990). Numerous studies have been devoted to the estimation of ET from meteorological observations, Jensen et al. (1990), Rötter et al. (1992) and Rötter et al. (1993). These studies each provided a comparative review of a range of potential ET estimation methods.

#### 2.1.4 Crop Coefficients

The ET from a particular crop at a specified growth stage is often related to the ET of a reference crop through the use of a crop coefficient,  $K_c$  (Jensen, 1983). The crop coefficients are derived from experimental data and have an empirical basis. Drenth and Pruitt (1977) compiled a list of crop coefficients for a variety of crops. Wright (1982) also derived crop coefficients for various crops at Kimberly, Idaho, from two irrigating cycles. Crop coefficients relate ET for each crop to a specific reference crop. Therefore, when selecting and using published crop coefficients, the correct reference-crop ET must be used to derive a reliable estimation. Since they are empirically developed, crop coefficients are also location dependent. Hargreaves (1964) suggested that crop coefficients should be applied under climatic conditions similar to the conditions where they were developed.

#### 2.1.5 *Evapotranspiration, Buckhorn, Florida*

In Florida, the narrowly distributed marsh and ET has been well recognized (Pearland and Polun, 1988; Rengwirth et al., 1990). Statewide marsh averages 0.03 billion

gallons per day and daily average ET is estimated to be about 112 billion gallons with the rate being the highest in southern coastal Florida and lowest in the Keys and northwest Florida (Furnish and Patten, 1984). A study of potential ET characteristics in Florida conducted by Samra et al. (1984) concluded that the annual potential ET at 1400 mm at West Palm Beach is only 1175 mm or 10.6mm/day. Annual variability was found to be 10% in the summer and 30% in winter months.

Evapotranspiration from forest and water bodies studies within Florida also showed high spatial and temporal variability. Skogerboe et al. (1982) conducted a landscape monthly ET study using Penman, pan evaporation, Thornthwaite, Blaney-Criddle, and water budget methods in the Everglades Agricultural Area. They concluded that the Penman method provided the closest prediction while pan evaporation and the Blaney-Criddle method could be used for limited data availability. ET data requirements in south

Florida were studied by Stolt (1981, 1982) and the results showed that solar radiation and air temperature are the most important factors among numerous other climatological data (pan evaporation, rainfall). Higher air wind velocity, maximum and minimum soil temperature, percent moisture retained on foliage, relative humidity). According to the results (Stolt, 1982) the ET was influenced 44% from solar radiation, 24% from mean air temperature, 7% from wind speed, and 24% from relative humidity. This indicates that if sufficient climatological data are not available for using sophisticated model, an alternative method should be chosen based on the solar radiation and temperature.

Kowalski (1984) estimated ET for the Rainbow and Silver Springs basins using a regional water budget approach. He concluded that ET accounted for about 79.7% (ET's index)



of the annual model of 51 Florida over a 30-year period and the wet season (June through September) ET rate was about twice the ET rate during the dry season (October through May).

ET of crops and vegetation in Florida were also studied by several researchers. Subased Ralls (1963) studied pan evaporation in relation to pan elevation, experiment rate and vegetation leaf area index (LAI) at the Dreyfus Agricultural Area. They found that maximum pan evaporation corresponded to low LAI in the vegetation field and a major difference in evaporation caused by elevations occurred at the period when the LAI was less than one. Benson (1964) studied ET of Pinewood-crest trees with four water table treatments using drainage lysimeters and concluded that the water table treatments did not significantly affect ET rates. A study of ET from areas of native vegetation in north central Florida was conducted by Redlake et al. (1966). Using energy balance (Bowen ratio (TBR)) and eddy correlation methods, he estimated 1,018 mm per year for the dry prairie type, 990 mm per year for the marsh type, 1040 mm per year for the pine flatwood type, and 930 mm per year for the cypress swamp type. Another study of ET from vegetation (sawgrass, dog fennel, dwarf bursera, and sugarcane) was conducted by Benson (1964) in a reclaimed area of Lake Wales Ridge, Florida. He estimated daily ET ranging from 0.2 mm per day in late December 1963 to about 1 mm per day in mid-July 1964. He also suggested that the simple Priestley-Taylor model would be preferable to the Penman-Monteith model for general vegetative studies since the Priestley-Taylor model is a good estimator of ET, is comparatively less complex, and requires fewer parameters.

## 2.2 Remote Sensing Techniques and Capabilities

### 2.2.1 Field Spectrometers

Field spectrometry is a technique of fundamental importance in remote sensing, both at the level of primary research and in operational applications. For fundamental vegetation property research as well as the interpretation of satellite data, relationships must be developed between remotely sensed spectral data and agronomic variables such as leaf area index, biomass, and fractional ground cover.

#### 2.2.1.1 Spectra and spectral response curves

Wavelengths of electromagnetic energy arriving at the earth's surface are either reflected, absorbed or transmitted. The proportion of the energy reflected, absorbed or transmitted will be dependent on the type and condition of the surface. The proportion of reflected energy will also vary between wavelengths, so that distinct peaks in certain spectral bands can often be clearly differentiated in other spectral bands. Different objects generally have spectral reflectance curves of different shapes and this forms a basis for identifying the object from remotely sensed data. The shape of the spectral reflectance curve of an object is often called its spectral signature. Spectral reflectance curves of typical vegetation, soil and water in the visible to middle infrared bands of the electromagnetic spectrum are shown in Figure 2.1. It is obvious that deep oceanic regions on the ground have considerably different reflectance characteristics in the visible and near infrared regions.

### 2.2.1.3 Spectral character of vegetation

A leaf is built of layers of structural tissues capable matter which are pigmented, water-filled cells and air spaces. Each of the three features (pigmentation, physiological structure, and water content) have an effect on the reflectance, absorption, and transmittance properties of a green leaf. Leaf physiology determines internal reflection by means of discontinuities in the refractive indices within the leaf. Four primary pigments are contained in higher plants, namely, chlorophyll *a*, chlorophyll *b*, carotenoid and xanthophyll, all of which absorb visible light for photosynthesis. Chlorophyll *a* absorbs at wavelengths of 0.43  $\mu\text{m}$  and 0.68  $\mu\text{m}$  and chlorophyll *b* at wavelengths 0.45  $\mu\text{m}$  and 0.65  $\mu\text{m}$ . The carotenoid pigments, carotenoid and xanthophyll, both absorb blue to green light at a number of wavelengths (Waringham, 1974; Curran, 1983). It is the combined effects of the leaf pigments and the physiological structure that produce the characteristic reflectance property for vegetation. The spectral character of light reflected by a normal plant leaf is controlled by two groups of cells (Figure 2.2). The long, narrow cells below the upper epidermis are the palisade cells. They contain many chloroplasts with chlorophyll pigments that absorb most blue and red light for photosynthesis and efficiently reflect green light. The chlorophyll absorption features are centered at 0.43  $\mu\text{m}$  and 0.68  $\mu\text{m}$ , while the area between the two features fills in the portions of the visible spectrum which results in the green color of plants. Leaf reflectance is reduced also as a result of absorption by three major water absorption bands that occur near wavelengths of 1.4  $\mu\text{m}$ , 1.9  $\mu\text{m}$  and 3.3  $\mu\text{m}$  and three minor water absorption bands

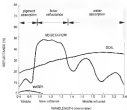


**Figure 2.1** Spectral reflectance curves of vegetation, soil and water in the visible, near infrared and middle infrared portions of EM radiation (adapted from Lillesand and Kiefer 1987)

that occur near wavelengths of 0.66  $\mu\text{m}$  and 1.1  $\mu\text{m}$  (Chavez, 1989). Table 3.1 shows the relationship between multi-spectral reflectance and vegetation amount for five wavelengths as defined by Tucker and Moreau (1979) for a grass canopy. These relationships provide information for the detection of vegetation covered by remote sensed multi-spectral wavelengths.

The vegetation spectral reflectance curve also provides a good indication for monitoring vegetation condition. The steep rise in reflectance of vegetation beyond 0.7  $\mu\text{m}$  is called the red edge of the chlorophyll band (Huete et al., 1987) and the slope of the red edge has been related to chlorophyll concentrations in the leaves (Baker et al., 1989). As vegetation becomes senescent, the infrared reflectance does not significantly decrease (Worley, 1973; Tucker et al., 1971), however, the breakdown of plant pigments causes a rise in blue and red reflectance. This results in a positive relationship between all wavelengths and vegetation amount. If the vegetation is deceased, the cell wall structure is damaged and the high absorbance between 0.7 and 1.3  $\mu\text{m}$  is reduced, which provides a diagnostic remote sensing technique for assessing the condition of plants. The shape and characteristic change in the reflectance of vegetation at about 0.7  $\mu\text{m}$  is the basis of a number of techniques for measuring the amount of vegetation present in a remotely sensed image (Huete et al., 1987).

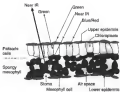


**Figure 1.2** Detailed diagram of a leaf's structure and an infection characteristic at middle and near IR wavelengths (adapted from Avery and Berber, 1997)

**Table 2.1** The multi-spectral reflectance and vegetation characteristics and their relationship to vegetation stress.

| Wavelength                    | Characteristics   | Relationship to vegetation stress <sup>a</sup> |
|-------------------------------|---|--|
| Ultraviolet/vis<br>100-500 nm | Strong chlorophyll <i>a</i> and carotenoid absorption       | Strong negative                                |
| Green<br>500-600 nm           | Reduced level of pigment absorption                         | Weak positive                                  |
| Green/red<br>600-700 nm       | Strong chlorophyll <i>a</i> absorption                      | Strong negative                                |
| Far red<br>700-1400 nm        | Transition between strong absorption and strong reflectance | Weak negative                                  |
| Near infrared<br>1100-1300 nm | High vegetation reflectance                                 | Strong positive                                |

<sup>a</sup> adapted from Tucker and Moreau, 1986.

Spectral reflectance curves of vegetation can also be used for early stress detection. When a healthy plant becomes stressed by some type of stress in its environment changes occur in its spectral curves. These stresses include nutrient deprivation, prolonged submergence by flood water, nutrient deficiency, plant diseases, and accumulation of soil salts (Schmidt, 1978). Figure 2.3 illustrates the changes in the typical reflectance properties of a plant leaf in a progression from a healthy state through different stages of damage.

### 2.2.1.3 Spectral responses of soil and water

Condit (1978) has classified 140 soil samples from 34 states into three general types according to the shape of their reflectance curves within the 0.4 to 1.0  $\mu\text{m}$  region of the spectrum (Figure 2.4). Type 1 curves have rather low reflectances with slightly increasing slope which gives them their characteristic to occur from 0.10 to about 1.0  $\mu\text{m}$ . Type 2 curves are characterized by a generally decreasing slope to about 0.6  $\mu\text{m}$  followed by a slight dip from 0.6 to 0.7  $\mu\text{m}$  with a continued decreasing slope beyond 0.75  $\mu\text{m}$ . This results in a typical convex shape from the visible to beyond 1.0  $\mu\text{m}$ . Type 3 soils are better drained and lower in organic matter than type 1 soils. Type 3 curves have a slightly decreasing steep slope to about 0.6  $\mu\text{m}$ , followed by a slight dip from 0.6 to 0.74  $\mu\text{m}$  with slope decreasing to zero area or becoming negative from 0.76 to 0.88  $\mu\text{m}$ . Beyond 0.88  $\mu\text{m}$  to 1.0  $\mu\text{m}$  the slope increases with wavelength. Type 3 soils have moderately high iron content. Condit was able to reproduce these curves within high degree of accuracy from measurements at five narrow band widths (0.02  $\mu\text{m}$ ) centered at 0.40, 0.54, 0.68, 0.74, and 0.82  $\mu\text{m}$ . Jones and Baumgardner (1985) modified two more types of soil reflectance curves similar to type 1 by extending the data out to 1.3  $\mu\text{m}$ . The type 4 reflectance behavior from 0.88 to 1.3  $\mu\text{m}$  was caused by high iron content and organic material. In type 3, the negative slope from 0.76 to 1.3  $\mu\text{m}$  resulted from very high iron and low organic concentrations. This was the only type that did not show a strong water absorption at 1.45  $\mu\text{m}$ .



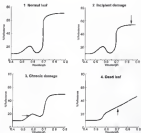


Figure 2.1 Average spectral response curves for a glass leaf as it progresses from a healthy state through different stages of damage (from Morita, 1979)

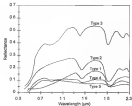


Figure 2.4 Typical soil reflectance curves for five major types of curves. Types 1-3 were proposed by Condit (1970) and types 4 and 5 by Sauer and Baumgardner (1990)

Although reflectance in all spectral regions is negatively correlated with organic, the region around 0.57  $\mu\text{m}$  is particularly useful for monitoring organic matter in lakes with close to or free of chlorophyll disturbances. Brown and Brown (1980) considered measurements at 0.3, 0.6, and 1.0  $\mu\text{m}$  to be essential for thorough classification of background soil reflectance. Absorption at 0.7 and 0.9  $\mu\text{m}$  are produced by dense iron compounds, while that at 1.0  $\mu\text{m}$  is caused by dissolved iron compounds.

The 0.4 to 1.0  $\mu\text{m}$  region is not useful for monitoring soil moisture content (Ragotzke et al., 1977) although the water reflectance curve is generally suppressed with increased moisture. The region centered at 2.2  $\mu\text{m}$  displays the highest correlation with soil moisture and is similarly important with vegetation.

Spectral reflectance of water is determined from vegetation, soils and non-vegetated targets on the ground. The most significant characteristic of water reflectance curves is the strong absorption at near infrared wavelengths (0.7 to 1.4  $\mu\text{m}$ ). Therefore, imaging and delineating water bodies with remote sensing data are performed most easily at the near infrared wavelengths (Lillesand and Kiefer, 1987). However, many factors, such as material suspended in the water, vegetation around in the water, turbidity, and so material at bottom of the water body, and so forth, can affect the reflectance of water.

#### 2.3.1.4 Field spectrometry measurement

Natural targets are usually illuminated by the whole hemisphere of the sky and thus, receive direct solar flux and scattered sky light. Interactions at the surface result in a proportion of this incident radiation being reflected, either directly from the surface, or

after multiple interactions within the surface of the material is involved in the incoming radiation. Natural targets are generally not perfectly-diffuse (Lambertian) reflectors and thus, the intensity of the reflected flux varies with the angle with which it leaves the surface. Consequently, the radiation environment comprises two hemispherical distributions of electromagnetic radiation, one incoming and one outgoing and, it is the interaction between these two which constitutes the focus of interest in field radiometry.

Radiation geometry of the field environment is shown in Figure 2.3. Note that the position of the primary source of radiation (the Sun) and the sensor are each defined by two angles, first, the angle from the vertical (the zenith angle,  $\theta$ ) and secondly, the angle measured in the horizontal plane from a reference direction (the azimuth angle,  $\phi$ ). The energy from the Sun and energy reflected to the sensor can be thought of as being confined to two slender elongated cones, each subtending a small angle at the target: rather, *zenith solid angles*, and measured in steradians ( $\text{sr}$ ). If these solid angles are sufficiently small, the reflectance of the target can be defined as

$$\rho(\theta_i, \phi_i; \theta_r, \phi_r) = \frac{dR(\theta_i, \phi_i)}{d\Omega(\theta_r, \phi_r)} \quad (2.22)$$

where  $d\Omega_i$  is the reflected radiance per unit solid angle and  $d\Omega_r$  is the radiance per unit solid angle, and the subscripts  $i$  and  $r$  denote incident and reflected rays respectively.

Both the radiance and the radiance vary as zenith and azimuth, hence, to specify completely the reflectance field at the target the reflectance must be measured at all possible combinations positions resulting in the 3-Dimensional reflectance distribution

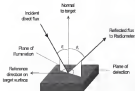


Figure 2.3 Naming geometry for the bidirectional reflectance measurements in the field environment.  $\theta_i$  and  $\theta_r$  are incident and reflected zenith angles, located in the vertical plane;  $\phi_i$  and  $\phi_r$  are azimuth and reflected azimuth angles, located in the horizontal plane.

function<sup>2</sup> (BRDF). However, in the field environment, measurement of BRDF on the target surface is not possible and an alternative is found through the standardization of reflected radiance by the use of a panel specified to be perfectly diffuse, completely reflecting and viewed under the same irradiance conditions and at the same geometry as the target. The radiance of the target is then measured as a proportion of the radiance of the standard panel.

### 3.1.3 Vegetation indices

A spectral vegetation index is obtained by isolating, differentiating, combining or transforming spectral data in response plant canopy characteristics. Its purpose is to differentiate vegetation from the soil background and to provide a numerical value that can be related to the various plant parameters. The vegetation index has been found to be very closely related to the green leaf area index (LAI) (Bastiaans et al., 1980; Hatfield et al., 1981), green biomass (Bastiaans et al., 1980; Hatfield et al., 1980; Anderson et al., 1982), the amount of absorbed photosynthetically active radiation (Gillis et al., 1985; Choudhury, 1987), fractional ground cover (Gillis et al., 1987) and vegetation moisture (Price, 1987).

The development of vegetation indices is guided by three general objectives including: (I) to enhance the relevant vegetation features, (II) to standardize the representation of vegetation spectral response (useful to compare regions or year to year comparisons) and, (III) to reduce the dimensionality of the data matrix if an index is not dimensionless which is derived from spectral data only (Rahmadegama, 1994).

Numerous formulae have been developed for assessing vegetation characteristics in the last twenty years. It is not possible within this study to cover all of the vegetation indices ever created. However, Perry and Lussichleger (1944) analysed the mathematical relationships of some five dozen vegetation indices derived the Landsat multi spectral scanner (MSS) and concluded that most of them are functionally related. Some of the most frequently used vegetation indices are discussed as follows:

### 1.1.2.1 Normalized difference vegetation index (NDVI)

The normalized difference vegetation index (NDVI) is defined as the ratio of the difference between the near infrared and red reflectances to their sum.

$$NDVI = \frac{NIR - R}{NIR + R} \quad (1.11)$$

The index is called normalized because it is divided by the sum of near-infrared and red near-infrared normalized for differences in solar spectral radiance. Vegetation areas will generate high values because of their relatively high infrared reflectance and low visible reflectance. In highly vegetated some areas, the NDVI typically ranges from 0.1 to 0.4, in proportion to the density and greenness of the plant canopy. Clouds, water, and snow, which have large visible reflectance than near infrared reflectance, will yield negative index values. Bare soil and bare rock areas have similar reflectances in the two bands and result in a NDVI near zero.

### 3.2.2.2 Difference vegetation index

The DVI is defined as the difference between the near infrared and red reflectance.

$$DVI = NI - R \quad (2.14)$$

It is similar to NDVI except without normalization (by dividing the sum).

However, NDVI is preferred to the simple DVI for vegetation monitoring because the NDVI compensates for changing illumination conditions, surface slope, aspect, and other extraneous factors.

### 3.2.2.3 Edge vegetation index (EVI)

EVI is the ratio of the near infrared and red reflectance. It is simple formula and

$$EVI = \frac{NI}{R} \quad (2.15)$$

can provide a good measure for the vegetation area, however, it may result in anomalously large values for low IR reflectance plants such as water bodies. EVI is related to NDVI as

$$EVI = \frac{1+NDVI}{1-NDVI} \quad \text{or} \quad NDVI = \frac{EVI-1}{EVI+1}$$

### 3.2.2.4 Transformed vegetation index (TVI)

The TVI has the same characteristics as NDVI except it added 0.5 to the NDVI as



$$PVV = \sqrt{\left( \frac{R_v - R_s}{R_v + R_s} \right)^2} = 0.5 \quad (2.26)$$

usual negative values and takes the square root of the result to produce the percent (Dearing et al., 1977).

### 2.2.2.3 Perpendicular vegetation index (PVI)

In agricultural systems, reflections from individual plants or individual rows of plants are closely intermingled with that from soil between plants and between rows of plants so that reflections are mixed, even in the least conditions. Mixing of soil and vegetation reflections can hinder the retrieval of the true vegetation conditions.

Richardson and Wiegand (1977) demonstrated that a plot of near infrared versus red reflectance for soils would fall on a straight line. As vegetation grows on the soil the red reflectance decreases and the near infrared increases. A vegetation point would lie away from this soil line with the perpendicular distance from the point to the soil line. The magnitude of the displacement with respect to the soil brightness line, which is called the perpendicular vegetation index, has been shown to be related to the amount of growing vegetation.

$$PVI = \sqrt{(R_{NIR} - R_{NIR}^s)^2 + (R_s - R_s^s)^2} \quad (2.27)$$

where  $R_{NIR}$  and  $R_s$  are reflectances for soil and vegetation respectively and  $R_{NIR}^s$  and  $R_s^s$  are soil reflectances for soil and vegetation respectively.

### 3.2.4.6 *Transformed cap transformation*

The "transformed cap" transformation of Korth and Thomas (1976) is a linear transformation based on the fact that the correlation between the visible and the near infrared bands of Landsat MSS data will project soil and vegetation information in agricultural regions into a single plane in multidimensional data space. The transformation states that MSS data such that the majority of information is contained in two components or features which are directly related to physical scene characteristics. The first component is similar to the soil line or the Perpendicular Vegetation Index, called the soil brightness index. The second, the orthogonal distance from the line to a vegetation point, is the greenness. The third component (yellowness) is orthogonal to both soil brightness and greenness, and the fourth component (called "brownish" because no features were evident) is orthogonal to the first three. Table 3.2 lists the coefficients and combinations of the four transformed components for Landsat MSS data.

The transformation coefficients of yellowness and brownish have been shown to indicate changes in-atmosphere layer conditions and, therefore, may be useful for indirect indication of the physical state of the atmosphere. Jackson et al. (1983) further showed that yellowness was sensitive to haze conditions and brownish was sensitive to water vapor absorption. However, disadvantages exist for the Transformed Cap transformation. First, the transformation is complex and time consuming which is a barrier for real time image processing. Basically, the transformation combinations in Table 3.2 are appropriate only to Landsat 3 MSS. For different sensors, and probably different field conditions if they

are very dissimilar to the field where the coefficients were derived, the transformation combinations must be evaluated individually.

Table 3.2: Equations for Thermal Cap transformation combinations

| Component                | Combination <sup>a</sup>                             |
|--------------------------|--|
| Soil brightness          | $0.13258354 + 0.40354553 + 0.47654554 + 0.34354557$  |
| Greenness                | $-0.28258354 - 0.44354555 + 0.37754556 + 0.38354557$ |
| Yellow soil <sup>b</sup> | $-0.35558354 + 0.47554555 + 0.37554556 + 0.44154557$ |
| Humidity                 | $-0.04558354 + 0.11154555 + 0.45254556 + 0.44254557$ |

<sup>a</sup> coefficients based on Landsat TMSS data

### 3.2.1.7 Soil adjusted vegetation index (SAVI)

Heale et al. (1983) found that at intermediate levels of vegetation cover, significant scattering and transmission of near infrared flux through the canopy produces a soil-reflected spectral signal that strongly resembles vegetation spectral signatures. This soil reflected influence depends on soil moisture content, soil roughness and can hinder the derivation of the actual vegetation condition. After analyzing a series of vegetation indices in near infrared soil wavelength space, Heale (1983) found that a shifting of the slopes of the reflectance spectra will account for first order soil-vegetation interactions and he proposed a soil adjusted vegetation index:

$$\text{SatV} = \left[ \frac{NM - B}{\rho(B - B + L)} \right] \approx (1 + L) \quad (2.28)$$

where  $L$  is an adjustment factor, for very low vegetation densities  $L = 1$ , intermediate vegetation densities  $L = 0.5$ , and higher density  $L = 0.25$ . Pharis also stated that a single value of  $L = 0.5$  can reduce soil noise considerably throughout the range in vegetation densities.

### 2.2.3 Thermal Remote Sensing

The earth surface can be thought to be a physical system which is periodically excited by the sun and which responds in two ways. First, the earth responds, by reflection, a portion of the energy which it receives from the sun, mainly in the visible and near infrared part of the electromagnetic spectrum. This part of the reflection, in principle, is the representation of the surface characteristics of the earth which are useful in determining vegetation moisture and conditions, delineating water body and forest types, discriminating soil and rock types, etc. Secondly, it receives part of the solar energy and emits directly in the thermal infrared portion of the electromagnetic spectrum. This emitted radiation is strongly related to the surface temperature and emissivity which can be used to infer the energy exchanges in the earth-atmosphere boundary.

#### 2.2.3.1 Physical Basis

All objects with temperatures above absolute zero emit electromagnetic (EM) energy. The magnitude and spectral distribution of this energy can be defined by Planck's equation for a perfect radiator:

$$M_\lambda = \pi B_\lambda(T) = \frac{2\pi hc^2}{\lambda^5 \exp\left(\frac{hc}{\lambda T}\right) - 1} \quad (2.28)$$

where  $B_\lambda$  is Planck's function,  $M_\lambda$  is the spectral radiant emittance, in  $\text{W m}^{-2} \mu\text{m}^{-1}$ ,  $h$  is Planck's constant,  $6.626 \times 10^{-34} \text{ J s}$ ,  $c$  is the speed of light,  $2.99792 \times 10^8 \text{ m s}^{-1}$ ,  $\lambda$  is the wavelength, in  $\mu\text{m}$ ,  $k$  is the Boltzmann constant,  $1.38066 \times 10^{-23} \text{ J K}^{-1}$ , and  $T$  is the temperature in degrees Kelvin. This equation describes the spectral radiance of an object per unit area per wavelength. Since natural objects are not perfect blackbodies, the above equation needs to be corrected by multiplying by the emissivity  $\epsilon$  for different materials. The total radiant emittance from a surface at a given temperature can then be determined by integrating  $M_\lambda$  with respect to wavelength for all wavelengths, i.e.

$$M = \int_0^\infty \epsilon M_\lambda d\lambda = \int_0^\infty \frac{2\pi hc^2}{\lambda^5} \exp\left(\frac{hc}{\lambda T}\right) - 1 \Bigg|^{-1} d\lambda \\ = \sigma T^4 \quad (2.29)$$

where  $M$  is the radiant emittance in  $\text{W m}^{-2}$ , and  $\sigma$  is the Stefan-Boltzmann constant,  $5.67037 \times 10^{-8} \text{ W m}^{-2} \text{ K}^{-4}$ . This fourth-power relationship between temperature and radiant emittance is known as the Stefan-Boltzmann equation. As electromagnetic radiation propagates through the atmosphere, it will weakly interact with various gases or water vapor it encounters in two ways: absorption and scattering. In absorption, a fraction of the energy passing through a volume element of the atmosphere is absorbed by atmospheric constituents and re-emitted in different directions and probably over a different range of wavelengths. In scattering, a fraction of the radiant energy passing

through the atmosphere is retarded by the atmospheric particles. In other case, the energy is lost from its original direction and the combined effect of scattering and absorption is called atmospheric attenuation. Therefore, it is natural to perform correction of the atmospheric effect to improve the quality of remotely sensed data. Atmospheric correction algorithms basically require two steps. First, the optical characteristics of the atmosphere and its effect can be modeled by the radiative-transfer algorithms or, measured by using spectral features of the target and the atmosphere (e.g., water bodies in clear sky/cloud conditions). Secondly, the images are adjusted by formulas/algorithms that derived the corrected target optical characteristics from the measured reference.

Considering both radiant sources in the ground and atmosphere, the energy going through a unit surface from a unit space-angle per unit time and unit spectral interval can be written in the form of the radiative transfer equation (Choudhury, 1997)

$$\frac{dI_{\lambda}}{ds} = -k_{\lambda} \rho_{wv} (I_{\lambda} - I_{\lambda}^0) \quad (2.11)$$

where  $I_{\lambda}$  is the intensity of radiation at wavelength  $\lambda$  passing through an absorbing and emitting layer,  $s$  the path length,  $I_{\lambda}^0$  spectral source,  $\rho_{wv}$  the density of water vapor, and  $k_{\lambda}$  the absorption coefficient optical depth. This equation states that the incoming spectral radiance  $I_{\lambda}$  reduces more for a greater spectral-optical depth along a direction  $s$  and that  $I_{\lambda}$  may be increased by a source  $I_{\lambda}^0$ . For a random mean or thermal infrared emission coming from the spectral source  $I_{\lambda}^0$  can be reduced to the blackbody radiation of the layer given by the

Planck's function  $\epsilon_{\lambda}$ , which merely depends on temperature  $T$ . After integrating Equation 2.14 along the scattering path between the surface and the top of the atmosphere with total optical depth  $\tau_{\lambda}^0$ , we obtain the spectral radiance  $I_{\lambda}$  emerging at the top of the atmosphere

$$\begin{aligned} I_{\lambda} = & \epsilon_{\lambda} B_{\lambda}(T_s) \exp(-\tau_{\lambda}^0) + \int_0^{\tau_{\lambda}^0} B_{\lambda}(T) \epsilon_{\lambda} \exp(-\tau_{\lambda}) d\tau_{\lambda} \\ & + (1-\epsilon_{\lambda}) \int_0^{\tau_{\lambda}^0} B_{\lambda}(T) \epsilon_{\lambda} \exp(-\tau_{\lambda}) d\tau_{\lambda} \exp(-\tau_{\lambda}^0) \end{aligned} \quad (2.15)$$

where  $\tau_{\lambda}$  is the optical thickness of the atmosphere along path  $s$

$$\tau_{\lambda} = \int_0^s k_{\lambda} \rho_{\text{atm}} ds \quad (2.16)$$

The first term on the right-hand side of Equation 2.15 represents the contribution to the surface temperature  $T_s$  via Planck's function  $B_{\lambda}(T_s)$ . Surface emissivity  $\epsilon_{\lambda}$  compensates the blackbody emission for the actual surfaces. In addition, spectral transmission of the atmosphere  $\epsilon_{\lambda}$  further attenuates the surface emission. The second term represents the contribution to the measured radiance resulting from the upwelling radiance scattered by the atmosphere towards the sensor, and the third term is the downward atmospheric radiance emitted by the atmosphere that is reflected (refracted)  $(1-\epsilon_{\lambda})$  by the land surface and attenuated along the upwelling path to the sensor. This equation indicates that surface emissivity and the atmosphere's condition are main factors that will influence the accuracy of satellite derived temperatures. It also shows the

satellite borne sensors are designed to work in one of the atmospheric windows for which molecular absorption is small and the atmosphere is highly transmittable.

### 2.2.1.2 Surface temperature estimation techniques

Since the late 1960s, satellite thermal infrared measurements have been utilized to provide estimates of sea surface temperatures (La Violette and Chelton, 1984; Curran and Rao, 1984). With the passage of time, and the production of improved satellite sensors, a large amount of study has been done to determine sea surface temperature from satellite radiance. For instance, to estimate sea surface temperature, the split-window method utilizes the spectral differential absorption of the atmosphere in two different satellite channels (McCluskey et al., 1982; Simpson et al., 1983; Hu et al., 1986) or uses the operational atmospheric sounding system (Scott and Chelton, 1987), or the angular differential absorption in one channel (Chelton et al., 1982). The estimation of sea surface temperature from a compositance and the channel accuracies are usually in the range of  $0.2^{\circ}\text{K}$  (e.g. Barnes, 1982; Chang, 1988). However, the results can not be directly applied to land surface mainly because of the following obstacles (Price, 1984; Becker and Li, 1988): 1) variability of the land surface is difficult to define and is generally different from sea. Furthermore, land surfaces are usually inhomogeneous, that is, a large range of land use may exist within the resolution of one satellite pixel which makes the determination of the effective emissivity difficult (Carettoni et al., 1988); 2) because the ground surface temperature within one satellite pixel is changing, it is not feasible to seek accurate ground truth verifications for satellite derived surface temperatures. Thus, not, the



radiance, may vary by several degrees over distances of tens of meters (Vaccaro et al., 1981) and temperature variations between upwind and downwind areas can be greatly driven. Despite the difficulties mentioned, scientists have been successfully searching for algorithms to extract surface temperature from satellite data.

### 2.2.3.1 Single channel method

Surface temperature estimated from single satellite channel is based on the solution of the radiative transfer equation (Equation 2.14) and the inverse of Planck's function (Equation 2.79). For cloud-free locations, the thermal spectral atmospheric window is relatively transparent to radiation except for the effects of atmospheric water vapor (Price, 1981). The integral in Equation 2.30 suggests that atmospheric emission is independent of surface radiation. Denoting the atmospheric emission and surface reflected atmospheric emission terms by  $\epsilon$ , and using symbol  $\alpha$  to represent atmospheric attenuation, the satellite observed radiation  $R_{sat}$  can be expressed as

$$R_{sat} = (1 - \alpha) R_{gsr} + \epsilon \quad (2.34)$$

This equation represents an aggregated outcome of the atmospheric effects in the solution of radiative transfer equation and expresses that the satellite observed radiation is linearly related to ground emission.

For typical surface temperature ranges (e.g., 270 to 330 degrees Kelvin), Slater (1980) pointed out that the Planck equation and its inverse are nearly linear in thermal infrared wavelengths. Consequently, the relationship between the surface radiant temperature  $T_s$  and satellite observed brightness temperature  $T_b$  can be expressed as

$$T_s = \alpha T_b + \beta \quad (2.13)$$

The surface radiant temperature, which in the atmosphere atmosphere corrected black body temperature at ground surface, is still subject to the influence of emissivity. For most natural surfaces in the 10–12  $\mu$ m thermal spectral region, emissivity values generally have magnitude greater than 0.95 (Sobolev and Efremov, 1982). Also, at these wavelengths, Slater (1982) found that the radiance,  $R$ , is proportional to the temperature raised to the 4.5th power,  $R \propto T^{4.5}$ . Thus, from the surface temperature  $T_s$ , one may obtain the surface kinetic (physical) temperature  $T$ , using the relation

$$\alpha(T_s/T)^{4.5} = \alpha(T_b/T)^{4.5} \quad (2.14)$$

so that

$$T_s = \frac{T_b}{\alpha^{0.222}} \quad (2.15)$$

Price (1983) further combined and combined with Equation 2.13 to

$$T_s = \left( \frac{2.5 - \alpha}{4.5} \right) \ln T_b + \beta \quad (2.16)$$

Sligh (1983) argued that the parameters in the Stefan-Boltzmann-type relation are temperature dependent and the 4.5th power equation will lead to significant errors at low temperatures. He suggested that the surface kinetic temperature,  $T_s$ , may derive directly from the integration of Planck's equation

$$\frac{1}{\Delta t} \left\{ \frac{C_p \delta^2}{\exp\left(\frac{C_p \delta^2}{T_g}\right) - 1} \right\} \Delta t = \frac{1}{\Delta t} \left\{ \frac{C_p \delta^2}{\exp\left(\frac{C_p \delta^2}{T_g}\right) - 1} \right\} \Delta t \quad (2.38)$$

where  $\delta$  is the control wave number in  $\mu\text{m}^{-1}$ ,  $C_p$  and  $C_g$  are constants, and have the result:

$$T_g = \frac{C_g \delta}{\ln \left[ 1 + \exp\left(\frac{C_p \delta^2}{T_g}\right) \right]} \quad (2.40)$$

The difference between equations 2.38 and 2.40, however, is less than one degree K for most natural surfaces with emissivity greater than 0.95. For global or regional surface temperature comparisons the simplicity of the Stefan-Boltzmann type equation (Equation 2.36) is preferred. However, for accurate point evaluation particularly for the city or town surfaces, the flight equation (Equation 2.40) or the split window technique is recommended.

#### 2.2.14 Split window technique

Surface temperature measured from two adjacent satellite thermal channels, generally called split window technique, was initially proposed by Arking and Kiehl (1980) for sea surface temperature (SST) estimation. Split window technique is based on the relation measured at two different wavelengths with a constant difference in absorption and can be used to determine the atmospheric transmission of the surface radiance so that surface temperature can be derived (Friedlander et al., 1979; 1980a,b, 1982). The general form of the split window surface temperature  $T_s$  is obtained by a

linear combination of two brightness temperatures,  $T_1$  and  $T_2$ , measured at two adjacent, adjacent channels

$$T_s = a_0 + a_1 T_1 + a_2 T_2 \quad (2.46)$$

Various methods (Singh 1985, McClure et al., 1983, Ho et al., 1986, Barton et al., 1988) have been proposed to obtain the coefficients  $a_0$ ,  $a_1$ ,  $a_2$ . Several split window formulae which give the surface radiant temperature  $T_s$  as a linear combination of temperatures given by the AVHRR channels 4 and 5,  $T_4$  and  $T_5$ , are tabulated in Table 2.3

Table 2.3 Split window formulae for surface radiant temperature estimation.

| Split Window Equations   | References                   |
|--|------------------------------|
| $T_s = T_4 + 2.6(T_5 - T_4) - 0.2$                                     | Donchamps and Pinoges (1980) |
| $T_s = T_4 + 5.13(T_5 - T_4) - 0.45$                                   | McClure et al. (1983)        |
| $T_s = T_4 + 0.30(T_5 - T_4)$  | Price (1984)                 |
| $T_s = T_4 + 0.48(T_5 - T_4) - 0.45$                                   | Li and McInnes (1984)        |
| $T_s = T_4 + 1.54(T_5 - T_4) - 0.40(T_4 - 10 \text{ } ^\circ\text{C})$ | Vincent (1984)               |

The split window technique is now used operationally over oceans with a claimed accuracy of 0.2°C (Kerr et al., 1980). This accuracy is possible principally because there is very little difference between sea surface temperature and air temperature near the surface and because the emissivity of the sea is nearly one and is constant over large areas. It is more difficult to use for land surfaces. The main difference is the effect of

surface emissivity, which is generally lower than unity, and must be taken into account in all cases. Lapierre and Kuo (1985) have mentioned that the split window technique used directly over land surface can result in errors that reach 3°K. Bédard (1987) also pointed out that if concentrations  $\epsilon_1$  and  $\epsilon_2$  in the two channels being considered are assumed to be unity, the error  $\Delta T$  generated in land surface temperature, by using the split window method, is significant and is of the order of

$$\Delta T = \frac{30(\epsilon_1 - \epsilon_2)}{\epsilon_1} - \frac{300(\epsilon_1 - \epsilon_2)}{\epsilon_1} \quad (2.42)$$

where  $\epsilon_1, \epsilon_2 \in [0, 1]$ .

Obviously, as the above equation, the closer  $\epsilon_1$  is to 1, the smaller the error in the land surface temperature calculation. That is, the channel split window method will provide good results over water, slightly less over fully vegetated areas, and generally poor results over dry land soil.

Theoretical investigation of the split window technique over land surfaces has been extensively examined in the last few years. Becker and Li (1990), after linearizing the radiative transfer equations, derived a series of equations which show that the coefficients of the split window technique for land surface temperature depends on spectral characteristics not on atmospheric conditions. The equation and coefficients they derived from the actual emissivity values are

$$T_s = A_0 + p \left( \frac{T_1 - T_2}{\epsilon_1} \right) + M \left( \frac{T_1 - T_2}{\epsilon_1} \right) \quad (2.43)$$

with  $A_0 = 1.274$ ,

$$P = 1 + 0.1948(1 - \alpha)/\alpha + 0.4824\alpha/\alpha^2,$$

$$M = 6.26 + 0.88(1 - \alpha)/\alpha + 0.1333\alpha/\alpha^2,$$

where  $\alpha^*(x) = \alpha_0/2$  and  $\Delta\alpha^*(x) = \alpha_0/2$ ,  $\alpha_0$  and  $\Delta\alpha_0$  corresponding to surface observations of channel 4 and channel 3 of NOAA/AVHRRS.

Seckler, Schlem *et al.* (1994), by linearization of the Planck's equation and atmospheric transmission, derived a split window equation whose coefficients depend on atmospheric water vapor, viewing angle, and channel surface observation. They concluded that in order to get an error below 0.4 K on land surface temperature, it is necessary to have an accuracy measurement with an accuracy of 0.001.

These derived split window methods, although theoretically possible, are difficult to implement, mainly because the channel-dependent model values are difficult to measure. Data availability, surface characteristics of spatial area, and the accuracy required for research are the key factors determining the method in surface temperature estimation from satellite data. Single channel method provides the most direct approach while split window technique effectively overcomes the atmospheric influence.

### 2.3 Remote Sensing of FT Parameters

Since the beginning of Earth remote sensing from satellites, remotely sensed observations of the Earth's surface provide a promising source of data for systematically measuring characteristics over land surfaces. Hydrologists and agricultural meteorologists have been searching for techniques to calculate FT from data provided by

satellites. The studies involving remote sensing techniques and ET estimation can be divided into four major categories: 1) empirical methods, 2) simplified energy balance methods, 3) numerical boundary layer methods, 4) surface parameterization methods and 5) spatial system methods.

### 2.3.1 Empirical Methods

Empirical relationships between the quantities that can be measured from a satellite and evapotranspiration have been recognized early. Allen et al. (1977) found a linear relationship between evaporation and wet thermal radiation. Minner (1979) obtained evapotranspiration as a bilinear function of the remotely-sensed temperature and surface albedo. Beggs and Rose (1982) have shown that, at a given location, there exists a good correlation between the monthly surface temperature and daily evapotranspiration. Katt et al. (1987) found a close relationship between the Normalized Difference Vegetation Index (NDVI) derived from NOAA High Resolution Visible Transmission (HRPT) data, and the actual evapotranspiration with a time lags of 20 days.

#### 2.3.1.1 Simplified Energy Balance Methods

Various researchers have related satellite derived surface temperature to a simplified energy balance equation for ET estimation. Holman et al. (1976) used software system derived surface temperature in conjunction with ground-measured solar radiation, wind speed, air temperature, and crop growth condition parameters to calculate daily ET based on an energy balance equation. Jackson et al. (1977) simplified the energy balance equation in which the daily evapotranspiration value is given as a function

of the instantaneous value of the difference between the surface temperature and the air temperature both measured over midday ( $T_s - T_a$ ). This equation is expressed as

$$ET = R_n - R(T_s - T_a) + A \quad (2.44)$$

where  $R_n$  is the daily value of the net radiation, and  $A$  and  $B$  are constants depending on the place of application. This equation has become the subject of many subsequent studies (Carlson and Poffenberger, 1978; Carlson et al., 1982; Laguarda, 1991; Nouranlou et al., 1983; Rashed et al., 1983; Seguin and Itier, 1983; Vidal and Perrier, 1987). These studies either theoretically justified the formula or proposed various means to determine the coefficients  $A$  and  $B$ . The advantage of this equation (Equation 2.44) is its simplicity, which requires minimal amounts of ground-based meteorological data (net radiation and temperature). Gurney and Hall (1962) used the Seasat Capacity Mapping Mission satellite to estimate ET over the Atlantic sub-tropics. Thalerstein and Nouranlou (1992) used the thermal infrared images of crop-lands with a Deschler digital scanner, in addition to wind velocity, crop type and height, to estimate potential ET of selected crops. They also developed a method to convert instantaneous crop temperature into 24-hour ET values. Vidal and Perrier (1986) developed a method to map the surface temperature from thermal IR data using data from the NOAA TIROS satellite and to map the ET of vegetation from surface temperatures. Some other studies similarly utilized once-daily remote estimates of surface temperature and ground-based data to evaluate the daily evapotranspiration based on surface energy balance (Gurney and Carlson, 1980; Hayfield et al., 1981, 1984; Laguarda et al., 1985; Senelise, 1987).



### 2.1.3 Numerical Boundary Layer Methods

Numerical algorithms for deriving surface values of temperature and fluxes at the scale of 100 km by 100 km, usually for climatological purposes, are required to provide input data for mesoscale general circulation models (GCMs). Simplified land surface and vegetation models and numerical methods also have been employed in solving surface energy budget equations. Wetzel and Chang (1980) utilized one dimensional boundary layer/vegetation/cell model and a explicit numerical method for the computation of grid-cell average evapotranspiration over heterogeneous areas. Tiedtke et al. (1988) applied the same boundary layer/vegetation/cell model with variable diurnal surface temperatures and introduced a representative canopy structure to simulate daily evapotranspiration distribution. Important experiments combining field measurements with recently issued data, such as (EURO-ISOBIOT) in France (Andrieu et al., 1988) and the First International Strategic Land Surface Climatology Project (ISLSCP) Field Experiment (FIFE) (Sellers et al., 1988) in USA, has been designed to map ET and surface parameters. Pan (1990) used a medium-range forecast model to simulate the surface fluxes occurring in the atmospheric boundary layer. Numerical weather prediction models have been used for simulating surface sensible and latent heat fluxes (Stieglitz and Munn, 1982; Tiel et al., 1988).

### 2.1.4 Surface Parameterization Method

Several surface parameters related to the calculation of ET are determined by remote sensing techniques. The surface parameterization is more relevant to the sat

radiation energy is the sum of the difference between the incoming and reflected short-wave solar radiation

$$R_n = R_s = \alpha R_s^0 = \alpha_s \alpha R_s^0 = \alpha_s \rho R_s^0 \quad (2.43)$$

where  $R_s$  is the incoming solar radiation,  $\alpha$  the surface albedo,  $\alpha_s$  the surface emissivity,  $T_s$  and  $T_a$  the air and surface temperatures (K), respectively, and  $\sigma$  is the Stefan-Boltzmann constant ( $5.670 \cdot 10^{-8} \text{ W m}^{-2} \text{ K}^{-4}$ ). Among these parameters, surface albedo, emissivity, and surface temperature can be estimated from remote sensing techniques. In addition to the air radiation, soil heat flux is another parameter that is related to ET and can be estimated by remote sensing techniques.

### 2.3.4.1 Surface albedo

Pinker (1983) and Pinker and Tang (1994), considering sun-sensor-observer geometry and the integration of spectral reflectance with respect to wavelength, satellite zenith angle and solar zenith angle, derived an equation of surface albedo from spectral albedo. Wydoski et al. (1987) reported a linear relationship between the broad and narrow band albedo which can be approximated by

$$\alpha = -0.70 + 0.36\alpha_1 + 0.73\alpha_2 \quad (2.44)$$

where subscripts 1 and 2 denote visible (channel 1) and near-infrared (channel 2) observed albedos, respectively.

### 3.3.4.2 Surface emissivity

Surface emissivity,  $\epsilon_s$ , is a factor that describes how efficiently an object radiates energy compared to a blackbody at the same temperature. The emissivity of terrestrial surfaces may vary significantly as a result of differences in soil texture, mineral composition, degree and nature of wetness, and a difference in vegetation cover (Van de Griend, 1991). The emissivity of natural surfaces has been traditionally determined by means of a emissivity box (Barnett and Kjaer, 1965) and by active methods (Bocher et al 1981). However, it is practically impossible to acquire the small effective emissivity of a particular pixel from individual measurements. Therefore, various methods (Aho and Canadian, 1981; Ding and Li, 1995; Van de Griend and Owe, 1993) have been proposed to estimate surface emissivity by remote sensing techniques. The empirical relationship suggested by Van de Griend and Owe (1993) gives the surface emissivity as a function of NDVI:

$$\epsilon_s = 1.0084 + 0.047 \ln (NDVI) \quad (3.47)$$

A theoretical based equation derived from the Planck radiation formula by Aho and Canadian (1981) gives surface emissivity as a function of two adjacent thermal-band observations and their wavelengths and is expressed as

$$\epsilon_s = \exp \left( \frac{4(T_{a2} - T_{a1})}{T_{a2} T_{a1} (\lambda_1^{-1} - \lambda_2^{-1})} \right) \quad (3.48)$$

where  $\epsilon_s$  is emissivity ( $\epsilon_s = 1.414 \times 10^3$  in  $K_2$ ), and  $T_{a1}$  and  $T_{a2}$  the radiated temperatures observed by two thermal sensor at central wavelengths of  $\lambda_1$  and  $\lambda_2$ , respectively.

### 2.3.4.3 Soil heat flux

Ground heat flux,  $Q$ , is given by the soil heat conduction equation as

$$Q = -k_s \frac{\partial T_s}{\partial z} \quad (2.48)$$

where  $T_s$  is the temperature of the soil and  $k_s$  is the thermal conductivity of the soil.  $Q$  is dependent on soil moisture and the amount of vegetation cover so the ground-based measurements of the soil heat flux cannot be extrapolated to large areas. In the energy budget equation, the soil heat flux obtains a very small quantity of available energy during daytime and this is almost balanced with nighttime radiative loss. An alternative approach to calculate soil heat flux from remote sensed data is to make it proportional to another term in the energy balance equation. Indeed, many researchers (Choudhury et al., 1986; Ragunath et al. (1983; Miao et al. (1973) have estimated that the magnitude of  $Q$  is highly related to the net solar radiation,  $R_n$ . Miao et al. (1973) found that the ratio of soil heat flux to net solar radiation is about 0.3 for dry soils and 0.5 for wet conditions. For vegetation surfaces under full cover, Minchin (1973) suggested values for the ratio would most likely be between 0.05 and 0.1. Ragunath et al. (1983) reported that the soil heat flux was approximately 1.8% of net radiation for bare soil and sparse canopy and less than 1.0% under a well developed plant canopy. The empirical relationship between  $Q/R_n$  and crop height  $h$ , obtained by Ragunath et al. (1983) was

$$Q = (0.1 - 0.002h) R_n \quad (2.49)$$

Choudhury et al. (1986) expressed the ratio as an exponential function of leaf area

index (LAI) yielding a correlation of 0.9. For regional energy balance studies, typically little information about crop height and leaf area is available. Thus, the two mentioned two methods cannot directly apply to the calculation of  $G$  by remote sensing methods. However, there are indications that remote sensed vegetation indices may be a good replacement for plant physiology, leaf area index and percent cover (Joshi et al., 1990; Goudry et al., 1991; Price, 1993). Indeed, Kustas et al. (1990) showed a linear relationship between  $G/R_n$  and the normalized difference vegetation index (NDVI) from observations of different vegetation types and soil surface conditions. The ground leaf flux in their analysis can be expressed as

$$G = (0.125 - 0.368 \text{ NDVI}) R_n \quad (2.11)$$

### 2.1.1 Temperature and Vegetation Index Method

Many studies on radiometric surface temperatures have focused on the widely observed negative correlation between surface temperature and remotely sensed measurements of actively transpiring vegetation such as NDVI (Joshi et al., 1990; Menon and Kustas, 1994; and Monte et al., 1994). Shuttleworth and Wallace (1980) adopted the Penman-Monteith equation (Monteith, 1965) to account for energy partitioning between crop and soil.

Gilkes et al. (1993) used a relation between NDVI and surface temperature derived from multi-spectral remote measurements to define surface fluxes. Over a large area, a plot of NDVI versus surface temperature forms a triangular distribution that is due to the distribution of soil moisture and vegetation cover. Schmugge and Becker (1991) also

observed the NDVI and surface temperature relationship with ET. Hansen et al. (1983) showed that pixels of both low NDVI and surface temperature correspond to areas of high soil moisture.

Pace (1990) developed a method for mixing contextual information (the slope of the vegetation index - surface temperature line and the slope of the wet soil - dry soil line) in AVHRR data to help with interpretation. Catterall et al. (1990) found that spatial variations in surface radiometer temperature are related to variations in the vertical variation of soil-water content, modulated by fractional vegetation cover. Based on theoretical and experimental evidence, Minnis et al. (1994) proposed a concept termed the vegetation index/temperature response, which combines vegetation indices with composite surface temperature measurements to allow application of Crop Water Stress Index (CWSI) theory to partially vegetated fields without knowledge of foliage temperature.

## 2.4 Remote Characterization in Remote Imaging

### 2.4.1 Spatial, Temporal, and Spectral Resolutions

The useful use of satellite data in remote sensing studies is often dependent on the correct selection of spatial, temporal, and spectral scales of the sensor. At a high spatial resolution of several tens of meters, a satellite can provide a spatially comprehensive view of land surfaces. However, the low frequency of the data may not be adequate to monitor hydrology and phenology variations. This is the case with the LANDSAT Thematic Mapper (TM) and the SPOT High-Resolution Visible (HRV) sub-sensor, which

have repetitive cycles of 14 and 24-days, respectively. The low temporal coverage limits the practical utility of these satellites in many types of applications such as, monitoring vegetation dynamics, measuring drought and flood conditions, and observing regional environmental change. On the other hand, satellites with very high temporal frequency but low spatial resolution sensors, such as GOES Visible and Infrared Spin-Scan Radiometer (VISSS) which have a 30-minute observatory frequency and an average resolution of 4 km by 4 km, may not be adequate for heterogeneous land surface characterization and vegetation distributions. The spatial scale identification which range the electro-magnetic radiations is able to be detected by the sensors. This is also an important consideration in the selection of satellite data. The spatial scale determines the information a satellite can extract from the land surface. Land use/cover and vegetation studies usually need several visible and infrared bands for land use classification and vegetation indices calculations. Land surface temperature and meteorological studies require thermal band. The spatial, temporal and spectral scales need to be determined in remote sensing applications. Table 2-4 lists the satellite image pixel size, time intervals and spectral coverages of the most commonly used satellites.

### 2.4.2 Optimum Spatial Resolution for Remote Sensed Data

Progress in the new satellites and improved sensors provide a variety of choices for large scale land surface studies. Systems, such as Landsat Thematic Mapper, SPOT, NOAA-AVHRR, and new satellites in planning, furnish users of digital satellite imagery

Table 2.4 Spatial, temporal and spectral coverage of Landsat, SPOT, GOES and NOAA satellites

| Satellite | Sensor                               | Pixel size   | Time interval | No. of Bands | Spectral Coverage         |
|-----------|--------------------------------------|--------------|---------------|--------------|---------------------------|
| Landsat   | MSS<br>TM                            | 79-m<br>30-m | 18 days       | 4<br>7       | VIS, NIR<br>VIS, NIR, TIR |
| SPOT      | HRV <sup>1</sup><br>HRV <sup>2</sup> | 30-m<br>10-m | 26 days       | 3            | VIS, NIR<br>VIS           |
| GOES      | VISSR                                | 1 km         | 30 min        | 3            | VIS, TIR                  |
| NOAA      | AVHRR                                | 1.1 km       | 12 hours      | 3            | VIS, NIR, TIR             |

<sup>1</sup> multi-spectral mode

<sup>2</sup> panchromatic mode

a choice of image scales ranging from 3 m to 4 km. As an increasing amount of satellite data becomes available, the selection process among different spatial resolutions becomes more difficult. Several studies (Latty and Mueller, 1981; Chaffin, 1987; Townsend and Justice, 1988) pointed out that imagery of fine spatial resolution, which vary as a function of the inherent spatial structure of the land-cover/land-use category of interest, does not necessarily improve per-pixel accuracy. Several factors influence the choice of an appropriate scale for a particular application. These include the information desired about the ground scene, the analysis methods to be used to extract the information and, the spatial structure of the scene itself (Woodcock and Strahler, 1987).



### 2.4.3 Methods of Determining Optimum Scale

To select an appropriate data scale, the spatial structure of images is a determining factor. The spatial structure of images is expected to be primarily related to the relationship between the size of the objects on the scene and spatial resolution. Molodtsov and Tsvetov (1972) used a geographic variance method for hierarchical geographical regions to quantitatively analyze the scale effects of geographic phenomena. They argued that geographical processes operate at different scales and that one can determine "where the action is" by calculating the statistical variances of the data at different levels of geographic units. Woodcock and Strahler (1967) developed a measure of local image variance to aid in selecting an appropriate image scale for a variety of land cover types. Their local variance is measured as the mean value of the standard deviation of a window moving across the image. The standard deviation of the window is computed and the means of these values over the entire image is taken as an indication of the local variability of the image. Miller and Briggs (1969) used a texture algorithm to study the heterogeneity under a variety of burning treatments on a natural prairie area. They concluded that their run-test algorithm values reflect the degree of textured contrast throughout the image; the higher the resulting textured number, the greater the degree of contrast in the landscape was. All the above geographic variances, local variance methods and the texture analysis method are based on the assumption that the variability of the geographic data changes with scale and resolution, and that the scale at which the maximum variability occurs is where most of the process operates.

#### 3.4.4 Selection Algorithms for Regional HT Models

The data required for evapotranspiration study must fulfill three major conditions. First, they must provide spatial quality that is sufficient for good spatial resolution to identify the best candidate on the ground. Second, the information must also meet the temporal quality that strictly fit need for frequent observation. Third, they should have spectral bands in the visible and thermal range in order to provide vegetation and temperature properties simultaneously. Regional scale evapotranspiration studies, due to their highly temporal variations and low spatial requirements, are often carried out using sensors with higher time frequency data and intermediate spatial resolution such as the AVHRR of the NOAA satellite.

## CHAPTER 5 METHODS AND MATERIALS

### 5.1 Field Spectroradiometry

A spectroradiometer was used to collect spectral responses from ground objects in the field. A collection of the response curves of Florida vegetation and soil were measured during 1994 to 1997. Background and overall spectral responses from a different source were used to 1) determine the most efficient spectral bands for discriminating between the two similar natural vegetation, and 2) determine the most desired source to distinguish between these two vegetation. The relationship between data from field spectroradiometer and from NOAA satellite was also established.

#### 5.1.1 Field Spectral Radiometer Measurement

In the field, radiometric reflectances were measured by a Geophysical and Environmental Research Corporation (GER) Spectroradiometer model GER 500 (GER, 1994). It is a portable spectroradiometer covering the ultraviolet (UV), visible, and near-infrared (NIR) wavelengths from 300 nm to 1600 nm. It uses a diffraction grating with a silicon diode array which has 1024 diode detectors that provide the capability to read 112 spectral bands (GER, 1994). With a spectral resolution of 1.7  $\mu\text{m}$ , the GER 500 spectroradiometer collects 512 discrete samples from 0.31  $\mu\text{m}$  to 1.61  $\mu\text{m}$  in 0.2 seconds.

Up to 400 spectral readings can be stored for subsequent down loading and analysis using a personal computer with a standard RS232 serial port and GRS Research operating software. A Spectronics diffuse white standard panel (SRT-09-00), calibrated by Labsphere (Labsphere, Inc., North Sutton, NH), was used for reflectance calibration. The reflectance of a target can be calculated as:

$$SR_{\text{tar}} = \frac{Rad_{\text{tar}}}{Rad_{\text{ref}}} \times 100\% \quad (1)$$

where  $SR_{\text{tar}}$  = spectral reflectance of a target (%);

$Rad_{\text{tar}}$  = target radiance ( $\text{W m}^{-2} \text{nm}^{-1} \text{sr}^{-1} \times 10^{-15}$ );

$Rad_{\text{ref}}$  = reference radiance ( $\text{W m}^{-2} \text{nm}^{-1} \text{sr}^{-1} \times 10^{-15}$ ).

The reference radiance is a measurement of the Spectronics panel under the same light and geometric conditions as the target measurement. Spectronics diffuse reflectance material is a commercially available poly-tetrafluoroethylene (PTFE) compound which maintains strong spatial and spectral uniformity and stability over time (Stowatz et al., 1997). It provides a calibrated reflectance value of 92% to 99% and a spectrality flat over the UV-VIS-NIR spectrum.

Spectral reflectance from vegetation and soil was collected with the GRS1500 spectroradiometer. Each sample was measured three to five times from different viewing angles and each measurement was calibrated with Spectronics panel. Mean reflectance at each wavelength was calculated over the measured target reflectances and 95% confidence intervals of the reflectance curves were calculated as:

$$\frac{\bar{x}}{s} \sqrt{\frac{d}{n}} \quad (3-2)$$

- where  $\bar{x}$  = sample mean,  
 $s$  = sample standard deviation,  
 $t_{\alpha/2}$  = test statistic with  $(n-1)$  degrees of freedom  
 $\alpha$  = 0.10 for 90% confidence level  
 $n$  = number of samples

### 3.1.2 Normalized spectral comparison

In order to better compare the difference in the shape of vegetation and forest reflectance curves, each reflectance was normalized with respect to the mean value of the entire curve. Normalized curves eliminated the reflectance intensity difference induced by growing conditions and, as a result, the spectral variation between vegetation species could be identified.

### 3.1.3 Selection of discrimination bands

In order to locate the bands for better discriminating between vegetation and forest, the spectrum was divided into five narrow bands, namely blue (425-475 nm), green (525-575 nm), and red (625-675 nm), near infrared (725-800 nm), and short infrared wave (825-875 nm). The mean spectral difference in these five bands was compared for the original reflectances and the normalized reflectances. A test statistic ( $T/S$ ) similar to the paired  $t$ -test was used to determine the better bands as follows:

$$L_{1,2} = \frac{\left| \frac{\sum_{i=1}^n P_{\text{measured},i} - \sum_{i=1}^n P_{\text{model},i}}{\sqrt{\frac{P_{\text{measured}}^2 + P_{\text{model}}^2}{2}}} \right|}{2} \quad (3.3)$$

where  $\overline{P_{\text{measured}}}$  is the sample mean for band 1, and var is the sample variance for the entire measured spectrum.

### 3.1.4 Comparison of Spectroradiometer and MODIS AVHRR

Spectral reflectance of the subcanopy in the soil and near infrared bands were extracted to compare with the band 1 (red) and band 2 (near infrared) reflectance of the MODIS AVHRR data. In order to match the redband range of the MODIS AVHRR, the band reflectance of the spectroradiometer was averaged by averaging the reflectance range from 0.58 to 0.68  $\mu\text{m}$ . And similarly, near-infrared reflectance was obtained by averaging the range from 0.77 to 1.00  $\mu\text{m}$  to match the near infrared band of the MODIS AVHRR. Reflections of vegetation, rainfall and open water on the aboveground data were used in the comparison. Satellite reflectances were acquired from the calibrated bands 1 and 2 of MODIS AVHRR images at the first 2 days (vegetation and rainfall) march. Three vegetation indices, NDVI, SAVI, and SAVI<sub>2</sub>, were also generated from the soil and near infrared reflectance.

## 3.2 Optimal Spatial Resolution

The land surface in south Florida is a mixture of urban, agriculture and, most importantly, a significant amount of wetlands which creates a unique geographical feature different than most other states. The study of the optimal spatial resolution in south

Florida was descriptive focused on three three major land cover/cover types. Agricultural land was selected from the sugarcane and vegetable fields in the Everglades Agricultural Area. Urban land/cover was selected from the commercial and residential areas in west Fort Lauderdale, and wetland was selected from marshes in the Everglades National Park. In addition, marshes inland with all three types of land cover plus part of Lake Okechobee and pasture land west of Everglades Agricultural Area, labeled wetlands, was also investigated in this study. Figure 3.1 illustrates the location of the four selected land cover/cover areas. Letter A represents agricultural area, W, wetlands, U, urban, and dashed line covers the marsh area.

### 3.3.3 Image Resolution Degradation

A georectified Landsat Thematic Mapper (TM)-image taken on April 5, 1994 supplied image data used to study optical spatial resolution. The spectral bands and ground resolution of Landsat TM are listed in Table 3.1.

Table 3.1 Spectral band, wavelength, spectral resolution, and ground resolution of Landsat Thematic Mapper (Lillesand and Kiefer 1987)

| Band | Wavelength (nm) | Spectral Resolution | Ground Resolution, (m) |
|------|-----------------|---------------------|------------------------|
| 1    | 0.45-0.52       | Blue                | 30                     |
| 2    | 0.52-0.60       | Green               | 30                     |
| 3    | 0.63-0.69       | Red                 | 30                     |
| 4    | 0.75-0.90       | Near infrared       | 30                     |
| 5    | 1.55-1.75       | Mid infrared        | 30                     |
| 6    | 10.4-12.5       | Thermal infrared    | 120                    |
| 7    | 2.08-2.13       | Mid infrared        | 30                     |

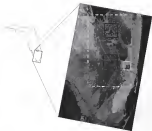


**Figure 3-1** Locations of the four selected land use/cover. Letter A stands for agricultural area (sugarcane and vegetable fields at Evangelical Agricultural Area); W for wetlands (Evangelical National Park and Water Conservation Area); O for open, grassy area at west Fort Leavenworth, and dashed line for the reserve area.



The near infrared band and the thermal band of the TdI were used for the optimal and the thermal portion of the experiment to determine optimal spatial resolution. The near infrared band was selected due to its capability to highly discriminate between vegetation and water.

The sub-images of the four areas of interest (urban, agriculture, wetland and marine), were cropped from the original 38 m-resolution Landsat TdI south Florida images. Each sub-image was then degraded to coarser resolutions by averaging neighboring pixels with a convolutional mask of 2, 3, 4, 5, 6, 8, 10, 20, 30, 40, 60, and 100 in order to create resolutions of 40, 60, 120, 150, 180, 240, 300, 400, 600, 1200, 1500 and 1800 m, respectively. These resolution-degraded images were then used for optimal spatial resolution determination.

### 3.3.3 Mean Local Coefficient of Variance

The spatial structure of images is primarily related to the relationship between the size of the object in the scene and spatial resolution and, when selecting an appropriate scale of data, the spatial structure of images is a determining factor. Woodcock and Kinsler (1987) developed a measure of local image variance to aid in selecting an appropriate image scale for a variety of land cover types. However, the local variance for each land-use type can not be computed in each other due to the high variability of the calculated variance. Furthermore, the variance calculated from one satellite can not be compared with data from other satellites or the chronologic data of the same satellite due to the difference in atmospheric conditions, sun-satellite-sensor geometry and sensor

effects. In this study, a new image-quality, Mean Local Coefficient of Variance (MLCV), was introduced and used to study the appropriate spatial resolution. The MLCV is measured as the mean value of the coefficient of variance of a 3x3 pixel window moving across the image (Figure 3.2). The coefficient of variance (CV) of the nine pixel values in the 3x3 wrap is computed and the mean of these CV over the entire image is treated as an indication of the local variability of the image. The reason for using an indication as that of the spatial resolution is considerably finer than the objects in the scene, most of the measurements on the image will be highly correlated with their neighbors, and a measure of local CV will be low. If the resolution is matching an approximate size of the objects on the ground, the likelihood of neighboring pixels being similar decreases and the local CV increases. Graphs of local coefficient of variance as a function of spatial resolution can then be used to measure spatial structure of images.

### 3.3 NOAA-AVHRR Data Calibration and Image Processing

#### 3.3.1 NOAA-TIR/GS-N Satellite

Since 1960, the National Aeronautics and Space Administration (NASA) and National Oceanic and Atmospheric Administration (NOAA) have launched and operated a series of Polar Orbiting Environmental Satellites (POES). This series of satellites commenced with TIROS-N, continued with NOAA-6 to NOAA-14, and is the longest-lived and most influential series of Earth observing satellites ever launched (Hestberg and Emery 1992). The NOAA satellites were initially designed to observe Earth's weather and cloud patterns. However, with the successful experiments in extracting information



**Figure 3.1** Schematic diagram of MLCV. The MLCV is measured as the mean value of the coefficient of variation of a 3×3 pixel window moving across the image.

from the Earth's surface, scientists have found that the NOAA satellites have a wide range of applications, not only in meteorology and climatology, but also in land surface studies.

The orbits of the NOAA satellites are near-polar, sun-synchronous, and with an orbital period of approximately 102 minutes, perform 14.1 orbits per day. Since the number of orbits per day is not an integer, the exact sub-orbital tracks do not repeat each daily frame; however, the local solar time of the satellite's passage is essentially the same for a given latitude. The primary environmental sensor for the NOAA satellites is the *Advanced Very High Resolution Radiometer (AVHRR)* which is a five channel scanning radiometer sensing in the visible, near infrared, and thermal infrared windows regions. The channel widths and features are tabulated in Table 3.2.

Table 3.2 NOAA/AVHRR spectral ranges

| Channel | Spectral ranges          | Description        |
|---------|--------------------------|--------------------|
| 1       | 0.65-0.68 $\mu\text{m}$  | visible (red)      |
| 2       | 0.725-1.05 $\mu\text{m}$ | reflected infrared |
| 3       | 1.55-2.12 $\mu\text{m}$  | near infrared      |
| 4       | 10.3-11.3 $\mu\text{m}$  | thermal infrared   |
| 5       | 11.3-12.5 $\mu\text{m}$  | thermal infrared   |

AVHRR channels 1 and 2 were designed to detect clouds, land-water boundaries, amount of snow and ice, the frequency of monsoon rainfall, and to measure

horizontal vegetation employing the computation of the vegetation indices. Channels 1, 4, and 3 were designed to be used to measure the temperature of clouds and the sea surface and for night-time cloud mapping. Current applications have the extended three original objectives.

The AVHRR is a scanning radiometer utilizing a rotating scan mirror at a rate of 360- $\mu$ sec. The instantaneous Field of View (IFOV) for all channels is approximately 1.4 milliradians leading to a resolution at the nadir (at-point off) 1.1 km for a nominal altitude of 435 km. The instrument has been designed in such a way that the IFOV of the channels can be made equivalent within  $\pm 1$  milliradians. The instantaneous field of view was chosen so that the satellite motion along its orbit would cause successive scan lines to be contiguous at the sub-point (nadirally, 100%). Figures 3.3 through 3.7 provide the spectral response curves for the NOAA-14 satellite. Note that the AVHRR sensors have near uniform distributions over their sensitive ranges. The analog data output from the sensors is digitized to a 16-bit precision digital number on board the satellite at a rate of 75,516 samples per second per channel. A total of 2048 samples is obtained per channel per scan. The instrument and sensor characteristics of NOAA-AVHRR are listed in Table 3.3.

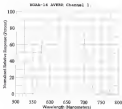
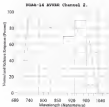


Figure 3.3 Spectral response curve for WGA-14 AVH8 channel 1 (adapted from Roberts, 1991)



**Figure 3-4** Spectral response curve for NOAA-16 AVHRR, channel 2 (adapted from Kubicki, 1993)

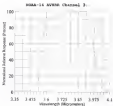


Figure 3.5 Spectral response curve for NDAA-14 AYBIR, channel 3 (adapted from Redwell, 1987)



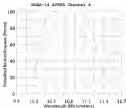


Figure 3.8 Spectral response curve for MOA-14 AVIRIS channel 4 (adapted from Kalivas, 1997)

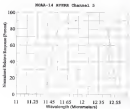


Figure 3-1 Spectral response curve for M3AA-14 ASTRON channel 5 (adapted from Kottrell, 1994)

Table 3.3 NOAA/AVHRR orbit, ground coverage and sensor characteristics.

|                   |   |
|-------------------|---|
| Orbit height      | 870 km  |
| Orbit inclination | 98.6 degrees  |
| Orbit period      | 101.58 min  |
| Scan angle        | 55.4 degrees on either side of nadir  |
| Ground coverage   | 2800 km   |
| IFOV              | 1.3 milliradians  |
| Ground resolution | 1.1 km (nadir), 2.4 km (max. off-angle along track)<br>6.8 km (max. off-angle across track)   |
| Image width       | 2048 pixels   |
| Quantization      | 18-bit binary (Digital Number 0 to 65535)   |
| Calibration       | space (now obsolete) for Channels 1 and 2<br><br>Wavelength surface radiance spectrally (TNO K) and space (J<br>K) for Channels 3, 4, and 5 |

Based on data circumstances, five day and-night pairs of NOAA/AVHRR images were used in this study. The images were obtained from the NOAA satellite archive archive (NAA) using the File Transfer Protocol (FTP) to transfer the images through the internet. The data processing time, and total number are listed in Table 3.4

Table 3.4 Date, overpassing time and orbit number of the NOAA-AVHRR data.

| Date       | Satellite | day/night | Overpassing<br>time (GMT) | Orbit<br>number |
|------------|-----------|-----------|---------------------------|-----------------|
| 08-18-1994 | NOAA-14   | day       | 07:10:10                  | 0442528         |
| 08-19-1994 | NOAA-14   | night     | 07:43:10                  | 0443535         |
| 08-24-1994 | NOAA-14   | day       | 07:17:43                  | 0446008         |
| 08-25-1994 | NOAA-14   | night     | 07:42:33                  | 0447537         |
| 12-09-1994 | NOAA-14   | night     | 07:28:31                  | 1001513         |
| 12-09-1994 | NOAA-14   | day       | 08:54:36                  | 1002522         |
| 01-24-1997 | NOAA-14   | night     | 07:46:38                  | 1132110         |
| 01-24-1997 | NOAA-14   | day       | 08:10:46                  | 1133040         |
| 05-30-1997 | NOAA-14   | night     | 07:34:36                  | 1244342         |
| 05-30-1997 | NOAA-14   | day       | 07:34:57                  | 1244549         |

### 3.3.2 Processing of NOAA-AVHRR Data

Information collected from satellite sensors provides large amounts of data and is transmitted in complex formats. Raw AVHRR data come with auxiliary data such as calibration coefficients, solar zenith angles, earth locations, and images in packed 10-bit radiometric resolution. The raw images contain both radiometric and geospatial values which have to be retrieved in order to quantitatively analyze and overlay other datasets. However, commercially available software packages were inadequate for the processing of AVHRR data as the raw data images were required. Research was conducted to address the AVHRR processing problem and a set of programs written in C language were developed to facilitate the data and image preprocessing procedures. The computer

programs include procedures to extract raw images and auxiliary data, correct radiometric errors using the calibration coefficients, correct geometric errors using the earth locations, output solar zenith angles and telemetry data. The program also included subroutines to read the uplink-down images from descending ground tracks and subroutines to save images in raw, ILAQ (Carlson et al., 1983) and VICAR (TREMBLE 1993) file formats. The descriptions of subroutines and program codes are listed in Appendix 3. A schematic diagram of the preprocessing of AVHRR/NOPT data is illustrated in Figure 3.8.

### 3.5.2.1 Images and data extraction

The AVHRR/NOPT image obtained from NOAA/NESD contained about 10 minutes of data covering a ground swath of 4500 km (along track) versus 2500 km (across track). The recorded radiation pairs consisted of about 1000 scanlines and each scanline was comprised of 2560 pixels. The 8-sensor radiance data was written on tape as two physical records per scanline. The data was digitized as 16-bit products and ordered as local coordinates by element format (area element 1 band 1, 2, 3, 4, 5, temperature element 2 band 1, 2, 3, 4, 5, etc). The solar zenith angle and earth locations (latitude and longitude) are sampled every 40 pixels starting at point 25 of each scanline and were embedded in the data record. The format of the NOPT physical record is shown in Table 3.9.



Table 3.5 Format of ISPT data (physical record)

| Byte number | Content in ISPT data file  |
|-------------|--|
| 1-2         | 2 bytes of scan line number  |
| 3-8         | 2-48 year, 5-bit day of year<br>21-48 millisecond-GMT time of day                    |
| 9-12        | 4 bytes of quality indicators  |
| 13-22       | 48 bytes of subimage coefficients<br>4-byte slope intercept coefficient for subimage |
| 23          | number of meaningful north-south and east-west location points appended to scan      |
| 24-104      | 81 bytes of solar zenith angles**  |
| 105-304     | 200 bytes of earth locations**   |
| 305-448     | 144 bytes of telemetry data  |
| 449-14304   | 13856 bytes of LAC/ISPT image data   |
| 14305-14800 | 496 bytes unused   |

\* A physical record (14800 bytes) are composed of two logical records (7400 bytes).

\*\* solar zenith and earth location data are sampled every 48 points starting at point 23

The image data in AVISAR tape are packed as three 18-bit samples in 8 byte (three-byte) groups, right-justified, with the first two bits zero, as illustrated below:



The packed format was extended to arrange the image data with as much spectral information and as few spaces between the image elements as possible. However, this packed-data format can not be read by most computer programs and needs special efforts to extract. The NOAA AVISAR processing software version by us was able to unpack the data and reform it so that the individual 18 bit samples were stored in consecutive pairs of bytes (i.e. 36-bit data in a 16 bit word) in a two-field data structure and interleaved. The data from the same channels were also rearranged and stored in sequence so that the original line-scanned interleaved format becomes a consecutive channel for each scanline (BTL format). The physical data header which contains calibration coefficients, earth locations, solar zenith angles and telemetry code was also read by the unpacking procedure and stored in a separate header file for further analysis.

### 3.3.3 Geometric rectification and sun-referencing

Rawline images are subjected to different geometric deformations due to the Earth's rotation, obliqueness, curvature, speed, attitude, and altitude variations of the satellite. The raw data and the projection of spherical surface on a flat image also



contributes to geometric errors. These deformations, if not properly accounted for, will prevent meaningful comparisons among data from ground-truthing and images acquired from different sources, and will also hinder further applications of the geographical information system.

Geometric rectification of the AVHRR images were performed with the following four major steps: (1) establishing a set of ground-control points (GCPs). GCPs are points whose coordinates can be identified with precision on both the satellite image and the map. Depending on the image resolution, the GCPs may be a lake, a highway intersection, or a permanent land feature. For NOAA AVHRR images of Florida, dependable ground control points are the distinct shoreline features and permanent water bodies; (2) converting the GCP coordinates to a Universal Transverse Mercator (UTM) coordinate. The geo-rectification transformation equations are based on least squares adjustment of both x and y distances in a plane. The geodesic coordinate (latitude/longitude) is not a plane projection, and when applied at a small area, the discrepancy may not be noticeable. However, it is important to use a plane projection in large coverage. The HSPF processing program is capable of converting the geodesic coordinates to UTM coordinates; (3) establishing mapping equation. Two first order polynomial equations were used to map the GCP coordinates (UTM easting and northing) to the corresponding AVHRR image coordinates (line/column) to the program. The image distortion caused by rotation, skew, translation and scale change was eliminated by the first order transformation. The mapping equation is as follows:

$$u = a_0 + a_1x + a_2y \quad (3-4)$$

$$r = h_0 + h_1x + h_2y \quad (3.5)$$

where  $x$  is the image line,  $y$  the image column,  $r$  the UTM column,  $z$  the UTM rowing,  $h_0$  and  $h_1$  are the mapping coefficients to be determined. This transformation is widely used and is sufficient to fit satellite images on UTM maps when the former does not coincide significantly. Least square technique was used in the program to estimate the transformation coefficients. The two-sum of square given

$$\sum_i (x - (h_0 + h_1x + h_2y))^2 \quad (3.6)$$

and

$$\sum_i (y - (h_0 + h_1x + h_2y))^2 \quad (3.7)$$

are differentiated with respect to the six unknowns and the resulting six equations are solved simultaneously; and (4) resampling. Resampling is a process of forming a new rectified image by choosing values from the original image. The nearest neighbor resampling scheme was used in the program.

### 3.1.1.3 Cloud Screening

Cloud contamination is one of the major problems in obtaining surface parameters from satellite observations (Dwyer, 1988; Stephens, 1988). For water surface temperature or vegetation index studies, cloud contaminated pixels should be excluded from the analysis. Clouds generally have a higher reflectance in short-wave channels and a lower thermal emissive than the earth's surface in thermal channels. Therefore, a certain digital number threshold can be set by statistically observing pixels containing clouds and identifying all pixels exceeding the threshold as cloud contaminated. It is

Frankignoul, 1994). This procedure is most effective in the thermal spectrum as warm clouds are often invisible in the reflecting spectral range (Frans, 1999). Clouds in the night-time images are even more difficult to detect, not only due to the considerable visible channels, but also due to turbulent low clouds at night (Scaudron, 1990). In contrast to day-time images, band 3 of the AVHRR (3.7  $\mu\text{m}$ ) night-time images appear broadly similar to the corresponding 11  $\mu\text{m}$  images. However, Hsu (CNTS) reported that the sensitivity of low clouds at 3.7  $\mu\text{m}$  wavelength is significantly less than at 11  $\mu\text{m}$  producing a significant difference in measured brightness temperature between the two bands which is normally much greater than the difference caused by atmospheric absorption. Since both day and night-time AVHRR images are to be used, the cloud cover condition was determined in two stages using both the daytime scans from the thermal infrared bands 3 and 5, and then visible band 1. The first step was the temperature difference detected at 3.7 and 11  $\mu\text{m}$  (band 3 and band 5 of AVHRR data). If the brightness temperature difference ( $T_{3.7} - T_{11}$ ) is greater than 2°C, then the pixel was flagged as cloud contaminated. The 2°C was suggested by Scaudron (1990) and proved appropriate in Florida (Shih and Tai, 1997). The second step was to examine whether the HRPT image was discernible using the visible band 1 to supplement the cloud classification. The cloud cover areas were then delineated and eliminated in this study.

### 3.1.3 AVHRR Data Calibration

Calibration is a process that converts the digital number in the image to meaningful surface characteristics. AVHRR visible data values (Channels 1 and 2) may

be reported as absolute and *ANYBR* thermal data values (Channels 3 and 4, and 5) may be converted to temperature values

### 3.3.3.1 Visible Channel Calibration

*ANYBR* visible channels (channel 3 and channel 5) are designed to provide conversion between the digital numbers and surface reflectivity (albedo). The percent albedo measured by the visible channel *i* is computed as a function of the input data value as follows:

$$A_i = 3.2C_i + 1 \quad (3-4)$$

where *A<sub>i</sub>* is the percent albedo measured by channel *i*, *C<sub>i</sub>* is the input data value, *a*, *b*, *c*, and *d*, are the scaled slope and intercept values, respectively. The scaled slopes and intercepts were calculated from the calibration coefficients extracted from BRPT data file (Kutner, 1997).

### 3.3.3.2 Thermal Channel Calibration

The thermal channels (channel 3, 4, and 5) are designed and calibrated together based on well as as space to provide direct conversion between digital numbers and radiant temperature. The conversion of radiant temperature from energy is performed using the inverse of Planck's radiation equation

$$T_d(C) = \frac{C_1 \cdot C}{\ln(1 + \frac{C_2 \cdot C^2}{R_1})} \quad (3-5)$$

where  $T$  = surface temperature ( $K_s$ ) for the energy value  $E$ ,

$n$  = canal wave number of the channel filter ( $\text{m}^{-1}$ ),

$C_1$  = constant ( $1.93644 \times 10^{-8}$  milliwatts/ $\text{cm}^2$ -steradian- $\text{cm}^2$ ),

$C_2$  = constant ( $458415$ -cm  $K_s$ ),

$E$  = energy measured by the sensor (channel 1) and

$$E_s = E_0 C + I$$

where  $E_0$  and  $I$  are scaled slope and intercept described above.

The temperature obtained by this procedure is radiant temperature, which needs further adjustment for atmospheric attenuation and surface emissivity. The atmospheric correction of brightness temperature was performed by the water-body radiance technique. Hourly water surface temperatures at four stations in Lake Okauchee were obtained from the South Florida Water Management District. The water surface temperatures were used since they provided large homogeneous surface temperatures with uniform emissivity. Surface water and emissivities are listed in Table 2.4.

The atmospheric-corrected radiant temperature is the actual surface temperature only when the emissivity is equal to 1.0. For most surfaces, where the emissivity is not equal to 1.0, a further adjustment needs to be undertaken. Emissivity adjustments were performed using the Stefan-Boltzmann relationship as follows:

**Table 3.4** Water temperature stations used for calibration of satellite surface temperature.

| Station ID | CO   | Station Description              | Lat    | Long   |
|------------|------|----------------------------------|--------|--------|
| L002+T0    | 0028 | Lake Okechobee Tower North (90)  | 270207 | 804713 |
| L003+T0    | 0044 | Lake Okechobee Tower West (90)   | 269714 | 803828 |
| L004+T0    | 0044 | Lake Okechobee Tower South (90)  | 264920 | 804428 |
| L000+T0    | 0044 | L000 Weather Station on Lake Oke | 265405 | 804721 |

Emmissivity values were assigned to each Florida land temperature based on values found in literature (Salisbury and D'Arra, 1993; Lefrand and Kerlin, 1987; Ross, 1990; Goggin, 1944). The emissivity values of Florida land surfaces used as surface temperature adjustments were listed in Table 3.3. These values are generally higher than values obtained from laboratory measurements due to the large area coverage and they are close to the average earth land surface emissivity value of 0.96.

Table 3.7      Sensitivity values for the lead wetland classes in Florida.

| Class | Lead wetland <sup>1</sup>        | Sensitivity |
|-------|----------------------------------|-------------|
| 1     | Coastal scrub                    | 0.95        |
| 2     | Bay prairie                      | 0.94        |
| 3     | Parclands                        | 0.97        |
| 4     | Scrub pine scrub                 | 0.96        |
| 5     | Kanifell                         | 0.93        |
| 6     | Scrub oak scrub                  | 0.96        |
| 7     | Mixed hardwood-pine forests      | 0.97        |
| 8     | Hardwood hammocks and forests    | 0.97        |
| 9     | Tropical hardwood hammocks       | 0.97        |
| 10    | Coastal salt marsh               | 0.98        |
| 11    | Freshwater marsh and wet prairie | 0.95        |
| 12    | Cypress swamp                    | 0.95        |
| 13    | Hardwood swamp                   | 0.99        |
| 14    | Bay swamp                        | 0.98        |
| 15    | Shrub swamp                      | 0.98        |
| 16    | Mangrove swamp                   | 0.98        |
| 17    | Buttonbush hardwoods             | 0.97        |
| 18    | Open water                       | 0.95        |
| 19    | Grassland (agriculture)          | 0.98        |
| 20    | Shrub-salt brushland             | 0.97        |
| 21    | Exotic plant communities         | 0.97        |
| 22    | Burns                            | 0.94        |

<sup>1</sup>Lead wetland types were adapted from the classes in Florida Lead Cover (Florida Game and Freshwater Fish Commission, 1992).

### 3.4 Rational ET Estimation Model

#### 3.4.1 Rational ET Estimation with Surface Temperature

The relation between latent heat flux,  $LE$ , and surface temperature can be expressed as

$$LE = (R_d - a) + a(R_a + aT_s^4) + Q = \frac{P(\rho T_s^4 - T_a^4)}{r_s} \quad (3.11)$$

- where  $LE$  = latent heat flux into the air  
 $R_d$  = downward short-wave radiation flux ( $W\ m^{-2}$ )  
 $a$  = surface reflectance coefficient  
 $\alpha$  = surface emissivity coefficient  
 $R_a$  = long wave atmospheric radiation flux ( $W\ m^{-2}$ )  
 $\sigma$  = Stefan-Boltzmann constant ( $5.67 \times 10^{-8}\ W\ m^{-2}\ K^{-4}$ )  
 $\rho$  = density of the moist air ( $kg\ m^{-3}$ )  
 $c_p$  = specific heat of moist air ( $J\ kg^{-1}\ K^{-1}$ )  
 $r_s$  = turbulent diffusion resistance ( $s\ m^{-1}$ )  
 $T_a$  = air temperature ( $K$ )  
 $T_s$  = surface temperature ( $K$ ), and  
 $Q$  = ground heat flux into the soil ( $W\ m^{-2}$ )

It can be seen from Equation 3.11 that the latent heat flux depends on a number of meteorological and surface parameters. Surface temperature,  $T_s$ , can be directly measured



by thermal infrared satellite observations. The diffusion resistance,  $r_{ds}$ , depends on wind velocity,  $v$ , and roughness length of the evaporating surface,  $z_0$ . As a first approximation,  $r_{ds}$ ,  $R_{ds}$ ,  $R_s$  and  $\tau$  can be taken as constants over a regional area. The surface parameters (surface albedo, roughness length and roughness length  $z_0$ ) can be determined in the field or derived from satellite image data.

This energy balance equation contains many parameters, several of which are insensitive to ET estimation. A simplified form was first proposed by Jensen et al. (1977) and further adapted by Begum and Thor (1981), Norman et al. (1982) and Begum et al. (1989). Using this approach the daily ET value,  $ET_d$ , is given as a function of the instantaneous value of the difference between the surface temperature and the air temperature (both measured at noon) and of the daily value for the net radiation,  $R_{nd}$ ,

$$R_{nd} - ET_d \cdot A = B(T_s - T_a) \quad (3.12)$$

where  $R_{nd}$ ,  $ET_d$  are in energy unit ( $W \text{ m}^{-2}$ ),

$T_s$ ,  $T_a$  is temperature unit ( $^{\circ}C$ ), and

$A$  ( $W \text{ m}^{-2}$ ), and  $B$  ( $W \text{ m}^{-2} \text{ }^{\circ}C^{-1}$ ) are constants

Theoretical justification for Equation 3.12 can be found by reference to the surface energy balance integrated over a one-day period. The  $B$  value as given in Equation 3.11 can be neglected over a 24-hour period. The constant  $A$  is an average of both contributions for the daily integrated sensible-heat flux. The surface temperature vs. air temperature variation ( $T_s - T_a$ ) is defined as  $\Delta T_p$  for this study. According to the

latitude, the constants  $A$  and  $B$  vary with location. Jackson et al. (1977) obtained  $A = 0$  and  $B = 0.04$  for the Phoenix, AZ area, while Sugan and Inou (1983) obtained  $A = 1$  and  $B = 0.23$  for the area of La Cane, France.

Ground-based meteorological data were accessed from the hydrological database for the 34 stations of the SPWMD. The data were used for calculating Equation 3.12, including air temperature, net radiation and the parameters used for potential ET calculations. Air temperature and net radiation values at the ground stations were interpolated to their temperature and radiation map layers with a grid size equal to the NOAA satellite ground resolution (1 km). A kriging method with a linear variogram was used to formulate the grid using the SURFER software (Golden Software, Inc., Golden, CO) for both air temperature and net radiation. Both air temperature and radiation maps, as well as satellite-derived surface temperature maps, were then georegistered and re-registered into the IDRISI vector geographic information system (Eastman, 1995) for further calculations. Potential ET at the 34 ground stations was calculated based on the modified Penman combination equation (Jackson et al., 1990) and stored in the GIS database as point coverages. It should be noted that both air temperature and net radiation have been interpolated to all points throughout the entire study area. The ET data could be estimated based on the local surface characteristics, using satellite-derived surface temperature, ground-based air temperature, and ground-based net radiation.

The relationship of the difference between net radiation and potential ET,  $(R_n - ET)$ , and the  $(\bar{P}_2/\bar{P}_1)$  values in Equation 3.12 was analyzed using a regression technique involving data from the 34 ground stations. The established relation could then used to

calculate ET values at all grid points using surface temperature, air temperature, and air radiation.

### 3.4.2 Relationship of Vaporization Index and Surface Temperature

Surface temperature is primarily dependent on the thermal inertia of the soil after meteorological inputs to the soil surface have been accounted for (Fingman and Chancy, 1981). Thermal inertia is a measure of the thermal resistance of a material to temperature changes. Some materials, e.g., dry soil, have low thermal inertia and exhibit wide diurnal ranges of temperature. Others, e.g., wet soils, have high thermal inertia and their observed diurnal temperature ranges are relatively less. The soil of the NWSA, similar to deserts in regions at 34-36 and 42-46 hours where surface temperatures are near the daily maximum and minimum, respectively. The diurnal difference of these two temperatures has been proven useful in determining thermal inertia and soil moisture (Van de Griend et al., 1982). Several studies (Jackson et al., 1977; Jackson, 1981; Salmeron, 1983) verified that, over bare soil, variations in surface temperature tend to be highly correlated with variations in surface water content.

The NWSA-GETV triangle approach (Figure 3-5) is based on the hypothesis that a triangle shape would result from a plot of vegetation index versus measured diurnal surface temperature variation. The top of the triangle corresponds to full vegetation-covered areas. The base of the triangle corresponds to areas with less vegetation index, either bare soil, forests or urban area. In between the triangle top and base, the major portion of the triangle corresponds to land with various fractional vegetation cover. The

the points at the base of the triangle correspond respectively to high and low drought surface temperature relative and low vegetation index.

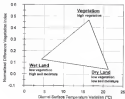


**Figure 3-9** The hypothetical triangle shape that would result from the relation between vegetation index and diurnal surface temperature difference.

The two base points also correspond to the water content of the surface. This is due to the high thermal inertia of water molecules which absorb high amounts of solar energy with little temperature change. The lowest right corner of the NDVI-DSTV triangle, with low vegetation index and high surface temperatures, is the location of dry soil based on the while the lowest left point is the location of moist soil.

#### 3.4.2.1 NDVI-DSTV triangle from field measurements

The NDVI-DSTV triangle concept was evaluated using the field measurements of surface reflectance and surface temperature. Several ground-covers, including asphalt, concrete surface, dry soil, wet soil, grass, cabbage, water with 0% vegetation cover, water with 75% vegetation cover, and water with 95% vegetation-cover were measured from ground level to evaluate the NDVI-DSTV triangle relationship.

Field surface temperatures were collected on several days coincident with NOAA satellite overpass times (0230h and 1430h). Surface reflectance temperatures of selected land covers were measured with an Ecoson thermometer (Model 210) hand-held infrared thermometer with an accuracy of  $\pm 0.1^{\circ}\text{C}$ . Surface reflectance temperatures were taken in the four directions and averages were computed. Field spectral reflectances were measured with CE314-0150 hand-held spectroradiometer following the procedures stated in section 3.1.2.

#### 3.1.2

#### 3.4.2.2 NDVI-DSTV triangle from satellite data

The NDVI-DSTV triangle relationship from NOAA-AVHRR was verified by plotting the scatterplots of NDVI and DSTV for seven major land cover types to verify

Florida. The land cover types and the locations of each type used in the watergram are listed in Table 3.8. Locations of the land cover were obtained from the classified Landsat TM images of the Florida Land Cover (Florida State and Fresh Water Park Commission, 1992).

Table 3.8 The seven land cover types and locations of chosen used in the watergram

| Name        | Land cover type            | Location of where used in watergram |
|-------------|----------------------------|-------------------------------------|
| Agriculture | green land and agriculture | agriculture fields in GSA's         |
| Pine        | pine land                  | west of J.W. Coker WMA              |
| Forest      | hardwood forest            | east of Naples, Collier county      |
| Marsh       | fresh-water marsh          | Everglades National Park            |
| Prairie     | dry prairie                | east Du Soto-county                 |
| Swamp       | cypress swamp              | Big Cypress National Preserve       |
| Urban       | houses and urban land      | urban center of Miami               |

#### 3.4.3 ET Estimation from SURFADSTN triangle

ET rate is dominated by two general categories of parameters: meteorological and surface. Meteorological parameters can be obtained from ground stations and their values, generally can be interpolated to sites without measurements. On the other hand, surface parameters are difficult to measure over large areas and can not be interpolated to other sites since different locations may have significantly different land-use/cover types.

Vegetation characteristics and soil moisture content are the major surface parameters that affect ET rate. Presence of green vegetation is a major determinant of ET from the land surface due to enhanced surface roughness increasing turbulent exchange of water vapor and plant roots extracting water from the soil more rapidly than the water can diffuse in the soil surface (Gash and Choudhury, 1991). The vegetation characteristics which are related to the ET rate include type of vegetation, plant density, and vigor. A quantitative description of vegetation and soil characteristics, however, is difficult to acquire at regional scale. Data observed by satellite sensors covering mostly constant areas with constant vegetation density and soil moisture content. Each pixel of the satellite image can be considered a combination of the responses from these sub-pixel areas. The fraction of vegetation cover and soil moisture in a region could be inferred based on their relationships with NDVI and DSTV, respectively.

Considering the large ground cover of each AVHRR pixel ( $\sim 1 \text{ km}^2$ ), it is assumed that there is homogeneity within each area corresponding to a satellite measurement. In Florida, each area can be considered as a mixture of vegetation, wet soil, and dry soil. The surface temperature and vegetation index sensed by satellite are also considered to be a mixture of the surface temperature and vegetation index from vegetation, wet soil, and dry soil. Letting subscripts  $v$  correspond to vegetation,  $w$  to wet soil, and  $d$  to dry soil, the temperature and vegetation index at point  $i$  can be written as

$$T_i = w_1 T_v + w_2 T_w + w_3 T_d \quad (3.10)$$

$$\text{NDVI}_i = w_1 \text{NDVI}_v + w_2 \text{NDVI}_w + w_3 \text{NDVI}_d \quad (3.14)$$

where  $w_1$ ,  $w_2$ , and  $w_3$  are weighting factors corresponding to the vegetation, moist soil and dry soil, respectively

Similarly, day-time and night-time temperature can be written as

$$T_{day} = w_1 T_{day} + w_2 T_{m, day} + w_3 T_{d, day} \quad (3.15)$$

$$T_{night} = w_1 T_{day} + w_2 T_{m, night} + w_3 T_{d, night} \quad (3.16)$$

Their difference,  $\Delta T_{day}$ , can be written as

$$\Delta T_{day} = w_1 \Delta T_{day} + w_2 \Delta T_{m, day} + w_3 \Delta T_{d, day} \quad (3.17)$$

Combining Equations (3.14) and (3.17), adding the third equation,  $w_1 + w_2 + w_3 = 1$ , and denoting  $T$  as  $\Delta T_{day}$  and  $V$  as  $NCVI$ , the weighting factors can be solved as

$$w_1 = \frac{T_2 P_3 - P_3 (T_2 - T_1) + T_3 P_2 - T_2 P_3}{T_2 P_3 - P_3 (T_2 - T_1) + T_3 P_2 - T_2 P_3} \quad (3.18)$$

$$w_2 = \frac{T_2 P_3 - P_3 (T_2 - T_1) + T_3 P_2 - T_2 P_3}{T_2 P_3 - P_3 (T_2 - T_1) + T_3 P_2 - T_2 P_3} \quad (3.19)$$

$$w_3 = \frac{T_2 P_3 - P_3 (T_2 - T_1) + T_3 P_2 - T_2 P_3}{T_2 P_3 - P_3 (T_2 - T_1) + T_3 P_2 - T_2 P_3} \quad (3.20)$$

The calculation of the weighting factors depends on the vegetation index and diurnal surface temperature variation of the three cover types and the procedure can be easily written into programs and determined efficiently



A new coefficient, vegetation and moisture coefficient (VMC), is introduced in this study. The VMC, defined as the ratio of actual and potential ETL, is similar in function to the crop coefficient but used for natural land cover. However, the VMC is different from the crop-coefficient in that it is not only related to the vegetation type but also related to the soil moisture content as is evident in the NDVI-DSTV plot. The VMC is known *i* with distant surface temperature variation (DSTV) and vegetation index (NDVI), can be written as the sum of the weighted values from vegetation, wet land and dry land (Figure 3) (8):

$$\begin{aligned} \text{VMC}(DSTV, NDVI) = w_1 \cdot \text{VMC}(\text{vegetation}) + w_2 \cdot \text{VMC}(\text{wet land}) \\ + w_3 \cdot \text{VMC}(\text{dry land}) \end{aligned} \quad (13)$$

This approach was based on the consideration that values of many properties are easier to compare for the extremes (full vegetation and bare soil) than for intermediate points. An important issue in applying this method is to find three distinct land water/cover types (i.e., vegetation, wet land and dry land) that are homogeneous and large-enough to be detected by satellite remote sensing, that the VMC can be estimated. The various land water/cover types in south Florida are well suited for the application of this approach. The sugarcane fields in the Everglades Agricultural Area are large homogeneous agricultural areas and have well documented crop-coefficients. The abundant wetlands in south Florida are good representations of large homogeneous wet land. The urban centers in the Atlantic coastal ridge, the West Palm Beach and Miami area are similar in the properties

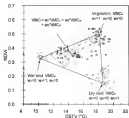


Figure 3.10 Relationship of vegetation and moisture coefficient (VMC) from the three corner points (Competition, wet limit, and dry limit) of the MDV-MDV triangle.

of dry land. The VMC for the vegetation, wet land and dry land are listed in Table 2.9. Monthly VMC of vegetation are determined by the ratio of vegetation ET and potential ET reported by Skiff and Charles (1980) and Jones et al. (1984). VMC of wet land was assumed a value of 0.95 indicating the ET is close to the potential ET ( $ET_p$ ). VMC of dry land was assumed a value of 0.05 indicating the ET is much smaller than the potential ET due to high percentage of buildings and pavement in urban areas.

Table 2.9 Vegetation Moisture Coefficient (VMC) for vegetation, wet land and dry land conditions in south Florida.

|                               | Jan  | Feb  | Mar  | Apr  | May  | Jun  | Jul  | Aug  | Sep  | Oct  | Nov  | Dec  |
|-------------------------------|------|------|------|------|------|------|------|------|------|------|------|------|
| <b>Vegetation<sup>1</sup></b> | 0.53 | 0.12 | 0.02 | 0.56 | 0.33 | 0.96 | 1.02 | 1.08 | 0.95 | 1.16 | 1.01 | 1.00 |
| <b>Wet Land<sup>2</sup></b>   | 0.95 | 0.95 | 0.95 | 0.95 | 0.95 | 0.95 | 0.95 | 0.95 | 0.95 | 0.95 | 0.95 | 0.95 |
| <b>Dry Land<sup>3</sup></b>   | 0.05 | 0.05 | 0.05 | 0.05 | 0.05 | 0.05 | 0.05 | 0.05 | 0.05 | 0.05 | 0.05 | 0.05 |

<sup>1</sup> Crop coefficients of vegetation from Skiff and Charles (1980) and Jones et al. (1984).

<sup>2</sup> assumed wet land surface ET close to  $ET_p$ .

<sup>3</sup> assumed dry land surface ET much smaller than  $ET_p$ .

Potential ET values were calculated with meteorological parameters from the ground network and interpolated to all areas in south Florida. The potential ET can be interpolated due the fact that they are determined from meteorological data which are considered less dependent of surface conditions. Actual ET values were computed as the result of multiplying potential ET by the VMC derived from satellite data.

$$ET_i = VMC_i \cdot ET_{pot,i} \quad (3.25)$$

where:  $ET_i$  = actual ET for pixel  $i$ ,

$VMC_i$  = vegetation and moisture coefficient for pixel  $i$ ,

$ET_{pot,i}$  = potential ET calculated by traditional method and extrapolated to pixel location  $i$ .

#### 3.4.4 Geographic Information System

In order to efficiently manage and manipulate the satellite images and ground data, the geographic information system (GIS) was used to manage the large amount of satellite and ground data. The GIS was implemented by the ERDAS Imagine software package (ERDAS, 1995). Satellite derived day and night time surface temperatures, diurnal surface temperature variation, land use/cover classes, albedo, and vegetation index were stored in the GIS. The weighting factor terms ( $\alpha_1$ ,  $\alpha_2$ ,  $\alpha_3$ ), vegetation and moisture coefficient ( $VMC$ ), extrapolated potential ET and actual ET were calculated in the GIS system. Regional ET was computed by summing up ET at the pixels within the region of interest.

#### 3.5 Model Validation

Validation of satellite-derived regional ET is difficult due to lack of ET records representing areas large enough to compare with satellite-derived values. Traditional ET estimation methods, regardless how complex, still represent a point estimation. In fact, the remote sensing ET estimation method in this study still utilized traditional ET

methods with ground measured meteorological data for potential ET estimation. Only the complex, surface-dependent crop coefficients (vegetation and moisture index) which are difficult to measure by traditional methods, were determined by remote sensing methods. Based on these limitations, verification of the model was twofold: 1) compare point ET at weather stations by traditional ET estimation method and by remote sensing method, 2) compare ET at wetland (lysimeter area). The lysimeters were located within a large marsh area and are designed to measure actual ET values from the large homogeneous marsh.

### 3.5.1 Verification with Traditional ET Methods

The meteorological data from 26 stations, including pan evaporation, solar radiation, air temperature, relative humidity, atmospheric pressure, and wind speed, were obtained from the South Florida Water Management District (SFWMD). Using the meteorological data from the ground stations, the ET was estimated by remote sensing method were compared with those by traditional ET estimation methods. Potential ET at the remote sensing method was measured by the Penman method. ET estimated by the Penman method was used to compare the results from the remote sensing method. The crop coefficients were assigned for each weather station based on its land use/cover type in the Florida land cover map (Florida Ocean and Fresh Water Pub Commission, 1992). The land cover type and the assigned crop-coefficient for each weather station are listed in Table 3.36. Boundary of the SFWMD study area and location of the ground meteorological stations is illustrated in Figure 3.11.

Table 3.18 Local cover type and the assigned crop coefficient for each weather station.

| Station Name | UTM     |           | Crop<br>Coeff. <sup>1</sup> | Local Use/Cover Type <sup>2</sup> |
|--------------|---------|-----------|-----------------------------|-----------------------------------|
|              | Easting | Northing  |                             |                                   |
| BELLE GL     | 534,823 | 3,048,298 | 0.70                        | Grass and Agriculture             |
| CPWH         | 519,382 | 3,056,889 | 0.70                        | Grass and Agriculture             |
| CLUPW        | 508,003 | 3,058,882 | 0.70                        | Grass and Agriculture             |
| FT. PI 2     | 566,240 | 3,054,893 | 0.70                        | Forelands                         |
| FT. PIER     | 544,003 | 3,059,876 | 0.70                        | Grass and Agriculture             |
| INDS1        | 491,386 | 3,058,084 | 0.40                        | Shrub and Deciduous               |
| JRTH         | 546,589 | 3,189,494 | 0.50                        | Marshy/ Swamp                     |
| KINGS IS     | 456,118 | 3,339,269 | 0.60                        | Dry Prairie                       |
| L. ALFLEX    | 409,380 | 3,308,000 | 0.80                        | Marshland Swamp                   |
| L. 000       | 521,867 | 3,368,773 | 1.00                        | Open Water                        |
| L. 004       | 582,262 | 3,361,772 | 1.00                        | Open Water                        |
| L. 006       | 521,413 | 3,366,594 | 1.00                        | Open Water                        |
| LEHIGH       | 623,280 | 3,363,883 | 0.70                        | Grass and Agriculture             |
| LONDON       | 623,408 | 3,351,294 | 0.40                        | Shrub and Deciduous               |
| LZAB         | 528,800 | 3,833,340 | 1.00                        | Open Water                        |
| MARTINWP     | 370,040 | 3,833,438 | 0.60                        | Barren                            |
| MEITS        | 608,248 | 3,751,608 | 0.50                        | Crescent Salt Marsh               |
| MI 48 SPW    | 510,139 | 3,894,543 | 0.80                        | Shrub Swamp                       |
| MOA          | 540,838 | 3,851,348 | 0.60                        | Barren                            |
| MO 1W        | 440,404 | 3,184,294 | 0.70                        | Grass and Agriculture             |
| MOAC         | 448,639 | 3,038,460 | 0.80                        | Freshwater Shrub & Wet Prairie    |
| STEW         | 448,871 | 3,863,979 | 0.70                        | Grass and Agriculture             |
| STAT         | 370,716 | 3,892,413 | 0.80                        | Shrub Swamp                       |
| TAMTRAB      | 617,849 | 3,348,850 | 0.50                        | Freshwater Shrub & Wet Prairie    |
| VERO 4W      | 558,275 | 3,056,668 | 0.70                        | Foreland                          |
| WPS LIND     | 566,282 | 3,390,813 | 0.40                        | Barren                            |

<sup>1</sup> value assigned<sup>2</sup> local weather type from Florida Land Cover (Florida Game and Fresh Water Fish Commission, 1992)

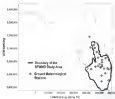


Figure 3.13 Boundary of the South Florida Water Management District study area and location of the ground meteorological stations

### 1.4.2 *Yachere marsh* Lymanets ET

The experimental sites were located on the upper St. John's river basin 28 miles west of Fort Smith and 15 miles east of Yachere junction on highway 68 (Figure 3.12). This is a fresh water marsh area where cattail (*Cyperus albugineus*) and sumpweed (*Cratogeomys punctulatus*) are the dominant vegetation. The west and north side of the marsh is an agricultural area covered by soybean and divided in grow-strips.

ET estimated by the remote sensing method was compared with the lymanets ET at two marsh environments. These lymanets were installed in the marsh area. To monitor the actual ET and vegetation growth, the lymanets were in similar ET than a large homogeneous marsh area. The lymanets were installed within marsh area with the vegetation, meteorological conditions and fresh being the same as surrounding vegetation. Lymanet 1 (30°41'18" W, 27°38'51" N) located in a cattail marsh, was placed cattail extracted from the surrounding marsh. Lymanet 2 (30°40'14" W, 27°39'12" N), located in a sumpweed marsh, was placed sumpweed extracted from the surrounding marsh. Lymanet 3 (30°41'34" W, 27°39'13" N) was an open water tank without any vegetation. Figure 3.11 shows the sumpweed lymanet and the meteorological water level gauge and water pond installed in the Fort Smith marsh. The lymanets were placed inside their respective environment in order to provide sufficient fresh and minimum water deficit. The main component of the lymanet is a 3.54 m diameter and 0.9 m deep polyethylene tank. Water levels in the lymanets were monitored with using capacitive gauges. Fluctuation in water level in the lymanets was regulated between 0.51 and 1.83 m by submersed inflow and outflow pump and flow meters. Data was



stored in CR10 data logger (Campbell Scientific, Inc.) and could be manually downloaded or transmitted through radio transmission.

ET of the lysimeter was computed by the water balance equation expressed as

$$ET_t = R + I - O + \Delta L \quad (1.30)$$

where  $ET_t$  = evapotranspiration for given period  $t$  (mm)

$R$  = rainfall (mm)

$I$  = inflow by water pump (mm)

$O$  = outflow by water pump (mm)

$\Delta L = D_t - D_{t-1}$ , change in water level in lysimeter for period  $t$  (mm)

A weather station was installed between lysimeter 1 and 2 to measure the meteorological parameters in the marsh. Solar radiation, net radiation, photosynthetically active flux density, air temperature, relative humidity, atmospheric pressure, wind speed and rainfall were recorded at 10 minute intervals.

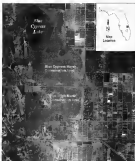


Figure 3.12 Location of RT experimental site in the Fort DeSoto Islands, Indian River County, Florida. Background coverage is 1995 black and white SPOT pseudo-color imagery.



**Figure 3-15**    *Sawgrass evapotranspiration lysimeter on the Fort Drum marsh experimental site. Photo shows sawgrass tank with automatic water level gauge and the background marsh.*

## CHAPTER 4 RESULTS AND DISCUSSION

### 4.1 Spectral Responses

#### 4.1.1 Response and Calculated Spectral Comparison

Reflectance from *unguis* (*Calceolaria pinnatifida*), *catali* (*Typha domingensis*) and the Spectralon standard white panel were measured by GPR 1100 spectroradiometer at the Fort Bragg ET experimental site on Oct. 19, 1994 (Dec. 23, 1994, Mar. 28, 1997 and May 30, 1997). Spectral reflectances were calculated with the target radiance divided by the standard white radiance. Reflectances of *catali* and *unguis* against the spectral wavelengths for the four dates, ranging from 350 nm to 1100 nm, are plotted in Figure 4.1 to Figure 4.4, respectively. Each reflectance curve averaged three to five measurements from different angles and was independently colorized. As shown on these four curves, *catali* averaged higher reflectance in the red to infrared spectrum in three of the four measuring dates (Dec., and Mar., 1994 and May, 1997). The percent of reflectance was directly related to the vegetation growing condition as, the reflectance percentage increased from near transparent in Oct. 1994 to mature in late May 1997.

#### 4.1.1.1 Normalized spectral comparison

In order to better compare the difference in the shape of *unguis* and *catali*

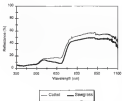


Figure 4.1 Reflectance curves of coral and sargassum in the spectral wavelength from 300 nm to 1100 nm in Oct, 1995, 1996

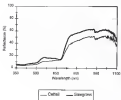


Figure 4-1 Reflectance curves of cellulose and gaseous water in the spectral wavelength from 200 nm to 1100 nm at Dec. 21, 1996

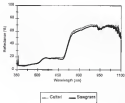


Figure 4.1 Reflectance curves of cellulose and cellulose in the spectral wavelength from 300 nm to 1100 nm at Mar. 28, 1997

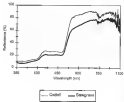


Figure 4.4 Reflectance curves of cotton and caryopsis on the opening wavelength from 300 nm to 1000 nm on May 10, 1997



reflectance curves, each reflectance was normalized with respect to the mean value of the entire curve. Normalized curves eliminated the intensity difference caused by overall growing medium soil, as a result, the spectral variation between vegetation species could be more clearly revealed. Figure 4.5 and 4.6 illustrates the normalized composite and actual spectral reflectance curves. As expected, since the shape of leaf reflectance is a unique representation of leaf structure, the four normalized curves of each vegetation displayed highly similar shapes. The first dates of normalized composite and actual curves are plotted in Figure 4.7. Actual and composite, both being without noise, with the exception of a few spectral regions, displayed similar normalized curves.

#### 4.1.1.2 Selection of discriminative bands

In order to locate the bands for more efficiently discriminating between composite and actual, the spectrum was divided into five narrow bands: blue (423–473 nm), green (523–573 nm), and (623–673 nm), near infrared (723–808 nm), and first infrared (908 nm). The mean spectral difference of these five bands was computed for the original reflectance and the normalized reflectance in Table 4.1 and 4.2, respectively. As evident in the two tables, the reflectance difference of the normalized curves reduced significantly. The most consistent deviation occurred at the red, near infrared and the first NIR mean bands indicating that these three spectral regions, 623–673 nm, 723–808 nm, and 908 nm should be given higher priority in band selection for discriminating between composite and actual.

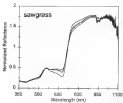


Figure 4.5 Normalized reflectance curves of corgones (*Cichlasoma jamaicensis*) at four dates. Note that the curves are almost identical curves except in few spectral regions.

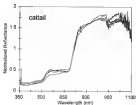


Figure 4.6 Normalized reflectance curves of catfish (*Cyprin donkeyensis*) at five dates. Note that the curves are almost identical curves except at few spectral regions.

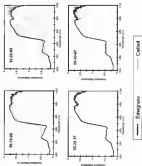


Figure 4.7

The annual/semi-annual curves of average (O-cubitus (average)) and critical (D-pole (average)) are shown for different years of the year

Table 4.1 Spectral difference of actual and program RGB wavelength primary on four dates. Test statistics are in parentheses. Differences are calculated as program reference subtracted by actual reference

| Wavelength<br>(nm) | Interval<br>location | Date                |                     |                     |                      |
|--------------------|----------------------|---------------------|---------------------|---------------------|----------------------|
|                    |                      | 12-18-96            | 12-22-96            | 02-18-97            | 03-18-97             |
| 425-475            | blue                 | -0.4642<br>(0.0034) | 2.2287<br>(0.1833)  | -0.2589<br>(0.0002) | -0.6178<br>(0.0004)  |
| 475-575            | green                | -1.5254<br>(0.1683) | 5.7569<br>(0.2744)  | -4.4544<br>(0.0002) | -9.8348<br>(0.1797)  |
| 475-675            | red                  | -1.7107<br>(0.3462) | 2.5279<br>(0.1267)  | -1.8698<br>(0.0714) | -6.8027<br>(0.1997)  |
| 735-800            | IR                   | -6.4624<br>(0.3048) | 12.6202<br>(0.0002) | -3.1518<br>(0.1267) | -77.5821<br>(0.2787) |
| 610-675            | first NIR range      | -1.4187<br>(0.3424) | 11.1171<br>(0.0282) | -1.2871<br>(0.0009) | -9.4842<br>(0.5179)  |
| 780-790            | red-green            | -5.3854<br>(0.2112) | 7.3149<br>(0.0472)  | -1.7452<br>(0.0002) | -4.4568<br>(0.2942)  |

**Table 4.2** Normalized spectral difference of actual and assigned color wavelength intervals on four dates. Test statistics are in parentheses. Differences are calculated as normalized average reflectance subtracted by normalized actual reflectance

| Wavelength<br>[nm] | Interval<br>location | Date                |                     |                     |                     |
|--------------------|----------------------|---------------------|---------------------|---------------------|---------------------|
|                    |                      | 12-21-96            | 11-23-96            | 05-29-97            | 05-30-97            |
| 425-475            | blue                 | 0.0195<br>(0.0304)  | 0.0364<br>(0.0344)  | 0.0009<br>(0.0040)  | -0.0132<br>(0.0194) |
| 525-575            | green                | 0.0144<br>(0.0329)  | 0.0073<br>(0.0340)  | 0.0146<br>(0.0327)  | -0.0231<br>(0.0404) |
| 625-675            | red                  | -0.1041<br>(0.1704) | -0.0309<br>(0.0377) | -0.0250<br>(0.0400) | -0.0115<br>(0.0366) |
| 725-800            | NIR                  | 0.0431<br>(0.0977)  | 0.0661<br>(0.0998)  | -0.0430<br>(0.0341) | -0.0923<br>(0.1484) |
| 925-975            | first NIR region     | -0.0301<br>(0.0773) | -0.0427<br>(0.0646) | -0.0398<br>(0.0633) | 0.1020<br>(0.1943)  |
| 110-1000           | whole spectrum       | 0.0000<br>(0.0000)  | 0.0000<br>(0.0000)  | 0.0000<br>(0.0000)  | 0.0000<br>(0.0000)  |

<sup>1</sup> average reflectance subtracted by actual reflectance

#### 4.1.1.5 Seasonal comparison

Vegetation with similar spectral responses are difficult to separate in satellite image classification. With spectral measurements from field spectrometers made in different seasons, it is possible to identify the best season for discriminating similar vegetation types. In Figure 4.7, the normalized reflectance curves are shown for different times of the year. These curves indicate that winter (Oct. 19, 1996 and Dec. 21, 1996) is better season for discriminating between meadow and cotton. This may be due to the fact that meadow meadows become dry and stay off during winter while most cotton leaves stay

#### 4.1.1.6 Comparison of Spectroradiometer and MODIS-AVHRR

The relationship between spectroradiometer and MODIS-AVHRR were evaluated through the red, near infrared bands and their derived vegetation indices. The results are compared in the follow section.

##### 4.1.1.1 Comparison of spectral bands and vegetation indices

Spectral responses of red and near infrared bands, as well as generated vegetation indices from spectroradiometer and from MODIS-AVHRR on the four dates are listed in Table-4.3. Due to the available data archive in the MODIS Satellite Archive Archive, AVHRR data from the nearest available dates of Oct. 21, 1996 and Dec. 24, 1996 were used to compare against the field measurements of Oct. 19, 1996 and Dec. 20, 1996, respectively. The date differences were considered negligible due to the relative invariance of vegetation in such a short time interval. As indicated by Table-4.3, the field

Table 4.3 Special responses of (M2D) and non-refined (M2) heads and the selected vegetation indices by field measurement and MODIS AVHRR at Fort Duess marsh.

| Date     | Vegetation | M2D (M2D) |                  |      |                   | M2 (M2) |       |      |                   |
|----------|------------|-----------|------------------|------|-------------------|---------|-------|------|-------------------|
|          |            | REF       | M2D <sup>1</sup> | NDVI | SAVI <sup>2</sup> | REF     | NDVI  | SAVI | SAVI <sup>2</sup> |
| 08-10-07 | Control    | 14.44     | 33.39            | 0.29 | 0.52              | 0.79    | 02.09 | 0.15 | 0.32              |
|          | Barangosa  | 18.52     | 44.31            | 0.39 | 0.69              | 0.86    | 02.07 | 0.20 | 0.40              |
|          | Water      | 2.67      | 1.39             | 0.24 | -0.11             | 2.68    | 1.60  | 0.08 | -0.24             |
| 12-26-07 | Control    | 19.45     | 40.88            | 0.39 | 0.61              | 0.82    | 01.88 | 0.11 | 0.31              |
|          | Barangosa  | 12.95     | 28.41            | 0.24 | 0.50              | 0.86    | 02.29 | 0.20 | 0.40              |
| 01-09-07 | Control    | 18.82     | 64.26            | 0.39 | 0.69              | 0.83    | 02.09 | 0.14 | 0.32              |
|          | Barangosa  | 17.54     | 62.99            | 0.40 | 0.67              | 0.85    | 02.07 | —    | —                 |
| 05-30-07 | Control    | 21.22     | 80.45            | 0.52 | 0.74              | 0.82    | 02.16 | 0.20 | 0.40              |
|          | Barangosa  | 20.29     | 71.94            | 0.49 | 0.63              | 0.83    | 02.18 | 0.22 | 0.40              |

<sup>1</sup> spectral range 2.55 - 0.65  $\mu$ m was used to create MODIS AVHRR and band

<sup>2</sup> spectral range 2.75 - 1.85  $\mu$ m was used to create MODIS AVHRR near infrared band.

<sup>3</sup> the nearest available AVHRR date of 01-11-07 was used

<sup>4</sup> the nearest available AVHRR date of 02-24-07 was used.

<sup>5</sup> data was available due to cloud contamination.

<sup>6</sup> 1-0.1 to SAVI calculation.



spectroradiometer measurements were significantly higher than that of the satellite measurements, both regarding individual band reflectance and vegetation indices. This is not unexpected due to the significant difference in sensor resolution. Field reflectance was measured at a short distance with the subject vegetation occupying most of the view, while satellite measurements were taken from high above and inevitably aggregated with some non-vegetated background (open water, exposed soil surface) in the neighboring pixels.

#### 4.1.3.2 Comparison of correlation among derived bands

The correlation of the spectral bands and vegetation indices between field and satellite measurements were further evaluated using regression analysis. The slope, intercept, and correlation coefficients of individual spectral bands and derived indices between field and satellite measurements are listed in Table 4.4. As shown, vegetation indices, in general, display a higher correlation than individual spectral bands except for the simple (B<sub>2</sub>/B<sub>1</sub>) ratio. This indicates that the derived vegetation indices generally better correspond to vegetation characteristics than do the individual spectral bands. Among the first vegetation indices, NDVI showed the highest correlation of 0.908.

#### 4.1.3 Results: Vegetation Reflectance Curves

Selected reflectance curves of Florida wetland/vegetation (cypress mangrove, *Spartina patens* wetlands), three Florida crops (sugarcane, citrus, corn) and common forest vegetation (pine, oak, palmetto) have been collected by the GBR-1500 spectroradiometer. Spectral reflectance was calibrated with a Spectralon white standard plate. The curves are

displayed in Appendix 1. Each vegetation response curve is an average of three to five measurements from different angles. The upper and lower 95% confidence intervals are also plotted with the mean curve.

**Table 4.4** Correlation analysis between geotransmittance and NDVI, SAVI2, spectral bands and derived vegetation indices. Data were calculated from measurements of vegetation, soil and water on four dates

| Band  | Description                           | Slope | Intercept | R <sup>2</sup> |
|-------|---------------------------------------|-------|-----------|----------------|
| B     | 0.58 - 0.68 $\mu\text{m}$             | 0.78  | 7.80      | 0.496          |
| IR    | 0.75 - 1.05 $\mu\text{m}$             | 1.84  | 23.35     | 0.613          |
| SAVI  | $\frac{B - R}{B + R}$                 | 0.63  | 3.71      | 0.794          |
| NDVI  | $\frac{IR - R}{IR + R}$               | 0.66  | 8.31      | 0.908          |
| SAVI2 | $\frac{IR - R}{IR + R + C} = (I + C)$ | 0.57  | 8.33      | 0.898          |

The collection of spectral response curves of Florida vegetation can be used as a spectral signature database. This database can aid in determining the appropriate number and range of spectral bands for vegetation discrimination.

## 4.2 Optical Remote Sensation

### 4.2.1 Image Resolution Degradation

The Landsat TM images were degraded to coarser resolutions by averaging their neighboring pixels within incremental units of 2, 3, 4, 5, 6, 8, 10, 16, 40, 50, and 100 to create image resolutions of 60, 90, 120, 150, 180, 240, 360, 400, 600, 1200, 1500 and 3000 m, respectively. Figure 4.8 illustrates the urban area in (a), 360 m (b), 600 m (c), and 900 m (d) spatial resolutions.

Using the original 30 m pixel size, the mean and standard deviation for each of the four land use/cover images was calculated with ERDAS IMAGINE (ERDAS, 1994) image processing software and the results are listed in Table 4.5. As expected, as a result of the high land cover variability in the urban area, the urban area had the highest standard deviation. On the other hand, due to relatively homogeneous land cover, wetland area produced the lowest standard deviation.

### 4.2.2 MLCV of Four Infrared Bands

The Intra-Local Coefficient of Variance for the near infrared band of the Landsat TM data was calculated for each of the four land use/cover types (urban, agriculture, wetland, and marsh) at 14 different spatial resolutions. The MLCV and its

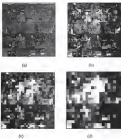


Figure 4.8

Random TIR images at four levels of spatial resolution degradation. Images show a roadstead seen from Loughside in (a) as (b), 30% as (c), and 50% as (d) resolution.

**Table 4.5** Size, location, area and standard deviation (S.D.) for the selected urban, agricultural, wetland, and mixed land use/cover types.

| Land Cover Type | No. of Pixels | Area <sup>a</sup> (Km <sup>2</sup> ) | Non-forest        |                   | Forest            |                   |
|-----------------|---------------|--------------------------------------|-------------------|-------------------|-------------------|-------------------|
|                 |               |                                      | Mean <sup>b</sup> | S.D. <sup>b</sup> | Mean <sup>b</sup> | S.D. <sup>b</sup> |
| Urban           | 140,000       | 324                                  | 70.66             | 20.83             | 156.87            | 4.28              |
| Agriculture     | 1,300,000     | 1,880                                | 44.99             | 21.23             | 334.17            | 4.80              |
| Wetland         | 1,300,000     | 1,880                                | 46.44             | 9.82              | 339.43            | 1.43              |
| Mixed           | 13,000,000    | 18,468                               | 51.46             | 20.24             | 332.34            | 4.47              |

<sup>a</sup> Area was calculated with original pixel size 30 m × 30 m.

<sup>b</sup> Mean and Standard Deviation (S.D.) values are for the Digital Number (DN) of the entire image.

corresponding resolution are listed in Table 4.4. The graphs of MLCV, as a function of spatial resolution, are plotted in Figure 4.3. As the peaks of the graphs indicate, the peak of urban, agricultural, wetland and minimum forest are at 60 m, 300 m, 1200 m, and 300 m respectively.

#### 4.3.3 MLCV of Thermal Images

The Mean and Coefficient of Variance for the thermal band of the Landsat TM data was calculated for each of the four land use/cover types at 14 different spatial resolutions. The thermal band MLCV and its corresponding resolution are listed in Table 4.5. The graphs of MLCV, as a function of spatial resolution, are plotted in Figure 4.3b. As the peaks of the graphs indicate, the peak of urban, agricultural, wetland and minimum forest are at 300 m, 400 m, 1800 m, and 600 m respectively.

#### 4.3.4 MLCV and Optimum Spatial Resolution

These peaks in the graphs of MLCV against spatial resolution identify the optimal image resolution to be used in selecting the remote sensing images for classifying the land/cover/resolution. For example, the agricultural field in the Everglades Agricultural Area required an appropriate resolution of 300 m which is approximately the size of the sugarcane field in the area. When spatial resolution is considerably finer than the size of the sugarcane field, the neighbouring pixels are either a single stalk or clump of sugarcane, which are spectrally homogeneous and results a low MLCV. A similar low MLCV occurs when the spatial resolution is so coarse that the many different

**Table 4-4** Mean Land/Coefficient of Variation (ML/CV) for some urban/land use values, agriculture, wetland, and marine land use/cover. Bold number indicates peak value location.

| Spatial Resolution (meters) | Land/Cover/Type |        |         |               |
|-----------------------------|-----------------|--------|---------|---------------|
|                             | Urban           | Agro   | Wetland | Marine        |
| 30                          | 2.0398          | 0.9549 | 0.3004  | 0.4428        |
| 60                          | <b>2.4311</b>   | 1.3988 | 0.3495  | 0.4175        |
| 90                          | 2.3322          | 1.9803 | 0.3340  | 1.0088        |
| 120                         | 2.3962          | 2.2687 | 0.3380  | 1.0840        |
| 150                         | 2.3419          | 2.4963 | 0.3332  | 1.0878        |
| 180                         | 2.0179          | 2.6562 | 0.3309  | 1.1113        |
| 240                         | 1.7810          | 2.7928 | 0.3336  | 1.1321        |
| 300                         | 1.6075          | 2.6485 | 0.3333  | <b>1.1387</b> |
| 450                         | 1.3830          | 2.4993 | 0.3497  | 1.0893        |
| 600                         | 1.0045          | 2.6379 | 0.3719  | 1.0640        |
| 900                         | 0.7621          | 2.1887 | 0.3662  | 0.9948        |
| 1200                        | 0.5318          | 1.7873 | 0.4087  | 0.9458        |
| 1500                        | 0.6543          | 1.6726 | 0.3933  | 0.9794        |
| 1800                        |                 |        | 0.3734  | 0.9788        |

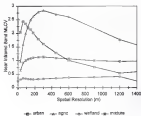


Figure 4-9 Near Infrared Band Mean Local Coefficient of Variance (MLCV) for urban, agriculture, wetland, and moderate land use/cover



**Table 4.3** Mean Local Coefficient of Variation (MLCV) for thermal load for urban, agricultural, wetland, and mixture land use/cover. Bold numbers indicate peak value location.

| Spatial Resolution (meter) | Land Use/Cover Type |               |               |               |
|----------------------------|---------------------|---------------|---------------|---------------|
|                            | Urban               | Agric.        | Wetland       | Mixture       |
| 50                         | 0.0067              | 0.0073        | 0.0008        | <b>0.0033</b> |
| 60                         | 0.0118              | 0.0093        | 0.0018        | <b>0.0061</b> |
| 70                         | 0.0184              | 0.0134        | 0.0024        | <b>0.0096</b> |
| 120                        | 0.0254              | 0.0230        | 0.0038        | <b>0.0136</b> |
| 150                        | 0.0264              | 0.0233        | 0.0040        | <b>0.0148</b> |
| 180                        | 0.0285              | 0.0292        | 0.0050        | <b>0.0163</b> |
| 240                        | 0.0302              | 0.0340        | 0.0055        | <b>0.0186</b> |
| 300                        | <b>0.0364</b>       | 0.0368        | 0.0068        | <b>0.0199</b> |
| 450                        | 0.0411              | <b>0.0384</b> | 0.0084        | <b>0.0213</b> |
| 600                        | 0.0507              | 0.0362        | 0.0089        | <b>0.0233</b> |
| 800                        | 0.0538              | 0.0376        | 0.0088        | <b>0.0258</b> |
| 1200                       | 0.0560              | 0.0396        | 0.0041        | <b>0.0285</b> |
| 1800                       | 0.0534              | 0.0564        | 0.0037        | <b>0.0299</b> |
| 2800                       |                     | 0.0585        | <b>0.0039</b> | <b>0.0296</b> |
| 3400                       |                     | 0.0582        | 0.0034        | <b>0.0285</b> |
| 7000                       |                     | 0.0588        | 0.0038        | <b>0.0288</b> |

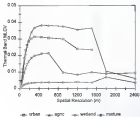


Figure 4.16 Thermal band Mean Local Coefficient of Variance (MLCV) for urban, agriculture, wetland, and pasture land use/cover

agricultural fields aggregated within a single pond. The appropriate resolution, therefore, is indicated by a peak in the MLCV graph, which occurs when the resolution is close to the dimension of the field and when the probability of having different pond values is high.

#### 4.3.3 Comparison of Near Infrared and Thermal Ground Resolutions

Graphs of near infrared and thermal band MLCV are functions of resolution are compared for the four land cover types (urban, agricultural, wetland, and moisture) in Figures 4.11 to 4.14, respectively.

Results suggesting the appropriate resolution for wetlands in south Florida is 1200 and 1800 m for near infrared and thermal band, respectively. This is approximately the same resolution of a weather satellite such as the NOAA/AVHRR, that which has 1400 m scale resolution. In other words, the spatial scale of the NOAA/AVHRR imagery is suitable for wetland studies in south Florida. The graph of the moisture band wetland had a peak at 300 m and 600 m, indicating that 300 m and 600 m is the preferred spatial resolutions for near infrared and thermal bands if only one resolution can be selected for the entire south Florida.

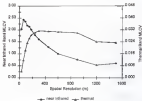


Figure 4.11 Mean Local Coefficient of Variance (MLCV) of the near infrared and thermal bands for urban land cover. Peaks of the near infrared and thermal bands are located at 100 and 300-m, respectively.

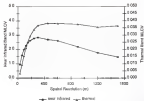


Figure 4.12: Mean Local Coefficients of Friction (MLCV) of the near-saturated and thermal loads for typical one-lane sections. Peaks of the near-saturated and thermal loads are located at 700 and 400 m, respectively.

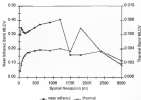


Figure 4-13 Mean Local Coefficient of Variance (MLCV) of the near infrared and thermal bands for wetland land restoration. Profiles of the near infrared and thermal bands are located at 1700 and 1800 m, respectively.

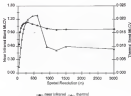


Figure 4.14 Mean Local Coefficients of Variation (MLCV) of the near infrared and thermal bands for various land use/cover. Points of the near infrared and thermal bands are located at 100 and 600 m, respectively.

## 4.1 Regional Environmental Information

### 4.1.1 Field Temperature and NDVI Measurements

Field surface temperatures were collected on several days coincident with NOAA satellite overpass times (0130h and 1430h). Surface radiative temperatures of selected land covers were measured with an Epperson International hand-held infrared thermometer (model 115). Surface radiative temperatures were taken in the four cardinal directions (North, East, South, and West) and averages were computed. Field land cover specimens were measured with a GER-1500 field spectra-radiometer and downloaded to computer via RS232 port for further analysis. Surface temperature and NDVI derived from field measured spectrum reflectance curves for several selected ground covers (asphalt, concrete, dry bare soil, wet bare soil, grass, tillage, water with 0% vegetation cover, water with 10% vegetation cover and water with 80% vegetation cover) are listed in Table 4.1. Spectrum reflectance curves for vegetation, soil and water samples for the selected ground objects are plotted in Figure 4.15.

### 4.1.2 Image Processing of NOAA AVHRR

NOAA AVHRR data in 16-bit packed format were acquired from the NOAA Satellite Active Archive via the internet file transfer and processed by my AVHRR processing program and ENVI4.8 images software package. Raw images and auxiliary data were extracted. Figure 4.16 illustrates the raw Florida image from the NOAA satellite with the Florida state boundary in the background. It is evident that the image is



Table 4.1 Field measurements of surface temperatures and regression values for locally selected ground objects.

| Target                        | Mean<br>$T_s$<br>( $^{\circ}\text{C}$ ) | Mean<br>$T_s - T_a$<br>( $^{\circ}\text{C}$ ) | Mean<br>$T_s$<br>( $^{\circ}\text{C}$ ) | Mean<br>$T_s - T_a$<br>( $^{\circ}\text{C}$ ) | Frequency |
|-------------------------------|---|---|---|---|-----------|
| Asphalt                       | 38.31                                   | 13.21   | 9.58                                    | 28.77   | 0.003     |
| Concrete                      | 33.80                                   | 7.87  | 8.58                                    | 25.22   | 0.181     |
| Dry floor ball                | 30.60                                   | 1.47  | 8.48                                    | 22.12   | 0.881     |
| Wet floor ball                | 18.46                                   | 3.67  | 18.70                                   | 7.93  | 0.881     |
| Grass                         | 15.18                                   | -4.60   | 20.28                                   | 3.10  | 0.688     |
| Cluggage                      | 13.88                                   | -4.85   | 8.93                                    | 4.95  | 0.186     |
| Waste with<br>50% veg. cover  | 17.93                                   | -1.23   | 11.58                                   | 3.00  | 0.500     |
| Waste with<br>100% veg. cover | 17.47                                   | -3.30   | 11.18                                   | 3.87  | 0.188     |
| Waste with<br>50% veg. cover  | 14.28                                   | -3.57   | 14.43                                   | 3.15  | 0.491     |

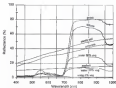


Figure 8.13 Spectral reflectance curves for selected ground objects (asphalt, concrete, bare soil, grass, cabbage, water with 10% vegetation cover, water with 30% vegetation cover and water with 60% vegetation cover) as measured by land-based reflectance

deformed due to scan skew and earth curvature. Geometric rectification was applied to correct the geometric deformations of the satellite images. Figure 4-17 shows the geo-rectified Florida image on December 9, 1994.

Normalized difference vegetation index (NDVI) was derived from the infrared and red bands of NOAA AVHRR data. NDVI in Florida ranged from -0.05 to 0.63 mainly depends on the plant density and vegetation type. Figure 4-18 illustrates the NDVI map of Florida. In the color scheme of NDVI map, the greener the color, the higher the NDVI. The upper St. John's river basin, Everglades Agricultural Area, and the southwest coast marsh display the highest NDVI. Open water bodies, urban areas, and wetland areas with low vegetation density display the lowest NDVI.

Surface temperature was derived and calibrated with the corresponding hourly lake surface temperature. Diurnal surface temperature was computed as the difference of the surface temperature at day-time pass (~1400h) and at night-time pass (~0300h). Figure 4-19 illustrates the satellite-derived surface temperature on Dec. 9, 1994. As shown, there is an apparent trend of temperature decreasing with latitude, the further north the location, the lower the surface temperature. Urban, metropolitan areas such as Miami, and West Palm Beach showed high surface temperature while lakes and wetlands displayed lower overall temperatures in the daytime satellite scans.



**Figure 4.16** Raw NOAA AVHRR image of December 8, 1998 with state boundary in the background. The image is geometrically-distorted due to scan skew and north rotation.



Figure 4-17 Geometrically rectified NOAA AVHRR image of December 9, 1998.



Figure 4.18 Normalized difference vegetation index derived from NOAA-AVHRR image for December 5, 1994.

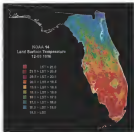


Figure 4-10 Land surface temperatures derived from NOAA-14 AVHRR images for December 8, 1996

### 4.3.3 Potential ET by Surface Temperature Method

The relationships between  $R_p/ET$  and  $SA/ET$  were calculated using a linear regression model and data from the 34 weather stations on four dates. The regression coefficients  $A$  and  $B$  of Equation 3.13 and the coefficient of determination ( $r^2$ ) are listed in Table 4.9.

Table 4.9 Coefficients  $A$  and  $B$  of the energy balance equation, and the coefficient of determination ( $r^2$ ) from the regression analysis of  $SA/ET$  vs  $(R_p/ET)$

| Date         | $A$         | $B$         | $r^2$ |
|--------------|-------------|-------------|-------|
| 14 Dec. 1989 | -0.48       | 0.26        | 0.44  |
| 30 May 1990  | -0.71       | 0.79        | 0.80  |
| 12 Dec. 1992 | -0.17       | 0.44        | 0.69  |
| 11 Apr. 1993 | -0.48       | 0.31        | 0.79  |
| Mean         | -0.49       | 0.45        |       |
| Std. Dev.    | $\pm 0.113$ | $\pm 0.267$ |       |

Coefficient  $A$ , the intercept of the  $R_p/ET$  and the  $T_p/T_a$  regression line, ranged from -0.48 to -0.71 with a mean of -0.49 and standard deviation of 0.113. Coefficient  $B$ , the slope of the regression line, ranged from 0.26 to 0.79 with a mean of 0.45 and standard deviation of 0.267. The results are in good agreement with the results concluded by other researchers. For instance, the average  $B$  value of 0.45 fell within the range of 0.23 as reported by Beggs and Ince (1982) and 0.64 as reported by Jackson et al. (1977).

Average of the  $r^2$  values is 0.73. Figure 4.26 illustrates the relationship between  $SA/ET$  and



( $R_{\text{net}}-ET$ ) on 11 Apr. 1993, and the regression line is expressed as follows:

$$R_{\text{net}} - ET_{\text{net}} = -0.40 + 0.30 (T_{\text{a}} - T_{\text{g}}) \quad r^2 = 0.74$$

As Table 4.3 shows, the wet season ranges (20 May 1990 and 11 Apr. 1993) appear to have higher  $r^2$  values (0.83 and 0.74) as compared with the other two dry season ranges (04 Dec. 1989 and 02 Dec. 1992) which had  $r^2$  values of 0.66 and 0.69. This might be due to the surface energy flux that is sensitive to the dense cover of vegetation grown in the wet season. In other words, using satellite derived surface temperature to estimate the regional ET in the wet season may be slightly better than that used in the dry season. However, further studies are necessary to support this observation.

ET estimated with the established relationship from the satellite-based data is plotted in Figure 4.20 against ET calculated from the ground-based data for the 34 stations. The relation of the satellite-based ET,  $ET_{\text{sat}}$ , and the ground-based ET,  $ET_{\text{gnd}}$ , is expressed as follows:

$$ET_{\text{sat}} = 0.78 + 0.79 \times ET_{\text{gnd}} \quad r^2 = 0.78$$

The  $r^2$  value of 0.78 implies that the satellite-based ET estimate is an indication of the ground-based ET estimation. However, the slope of regression was 0.79, not 1.0. This means that there was slight discrepancy between two approaches in ET estimation. In the meantime, it should be noted that the ground-based ET is a point estimation, while the satellite-derived ET is a manifestation of an 1 km<sup>2</sup> area. This spatial coverage difference could cause a deviation between two approaches.

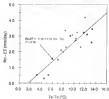


Fig. 4.20 Relationship of the difference between wet bulb and air temperatures and evapotranspiration ( $T_w - T_a$ ) and the surface-to-air temperature difference ( $T_s - T_a$ ) on 11 Apr. 1990.

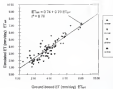


Fig. 4.21 Simulated ET from the linear relationship between  $\Delta QTP$  and  $E_p/ET$ , versus ET calculated from ground measured meteorological data for 4 dates

#### 4.3.4 NDVI and DIRT Triangle

Relationship of surface temperature and vegetation index was evaluated with both the field measured results and satellite data. Day-time (14:00 to 15:00) surface temperature  $T_s$ , air temperature  $T_a$ , night-time (01:00 to 02:00) surface temperature  $T_n$ , and spectral responses were measured at ground level with a thermal infrared thermometer and spectroradiometer. Figures 4.21 to 4.24 show the NDVI and surface temperature ( $T_s$ ), diurnal temperature difference ( $T_s - T_n$ ), and surface air temperature difference ( $T_s - T_a$ ) relationship for the selected ground objects, respectively. It can be seen that the points with the highest diurnal surface temperature difference are dry surfaces (pavement, concrete, dry bare soil); the points with the lowest diurnal surface temperature difference are wet surfaces (water covered by vegetation, wet bare soil), and the points with the highest vegetation index are grass and vegetables. These points generally form a triangle with dry surface, wet surface, and vegetation at three corners. Satellite derived NDVI and diurnal surface temperature deviation are plotted in Figure 4.25.

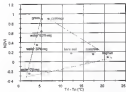


Figure 4.22. NDVI and diurnal temperature difference ( $T_d - T_a$ ) relationship for the selected ground objects measured in the field.

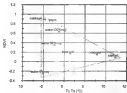


Figure 6.23  $(T_s - T_a)$  and surface air temperature difference ( $T_s - T_a$ ) relationship for the selected ground objects measured inside field.

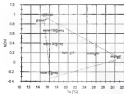
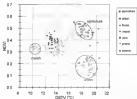


Figure 4.24 MDV1 and surface temperature relationship for the selected ground objects measured in the field



**Figure A.25** Satellite derived normalized difference vegetation index (NDVI) versus diurnal surface temperature difference (DDTV) for various land use/cover types. Agriculture, other, and forest are the three corners of the NDVI-DDTV triangle.



#### 4.3.5 Remote SE Estimation

The NDVI-DSTV triangle relationship was used to calculate weighting coefficients of VMC as defined in Equation 3.11 to 3.17. The DSTV, NDVI and weighting factors for the eight selected land cover/cover on Dec. 5, 1994 are listed in Table 4.16. Land cover types, Grass and Agriculture, Barren and Urban Land, and Fresh Water bodies, are assigned as the three corners (agriculture, dry land, and wet land) of NDVI-DSTV triangle, respectively. The DSTV and NDVI were average values of all pixels within the selected area. Weighting factors,  $w_1$ ,  $w_2$ ,  $w_3$ , indicate the membership of the selected land cover type is agriculture, wet land, and dry land, respectively.

As shown in Table 4.16, the mangrove swamp and open water swamp have higher values of  $w_3$  weighting from wet land (fresh water swamp). The VMC can be determined based on the NDVI-DSTV triangle relationship for locations with various fractions of vegetation cover and soil moisture due to the fact that the points at the corners of the NDVI-DSTV triangle are relatively easy to measure or can be reasonably assumed.

The potential ET values at ground weather station were computed by the Penman method and interpolated to the entire study area using the Kriging interpolation algorithm with linear variogram. The interpolation was implemented using the software package SURFER for Windows (Golden Software Co., Golden, CO).

Table 4.16: DSTV, NDVI and weighting factors for the eight selected land cover/cover on Dec. 5, 1996

| Land Cover Type <sup>1</sup> | DSTV    | NDVI   | $w_1$  | $w_2$   | $w_3$  |
|------------------------------|---------|--------|--------|---------|--------|
| Cropland and Agriculture     | 17.1832 | 0.4753 | 1.0000 | 0.8000  | 0.0000 |
| Barren and Urban Land        | 18.4907 | 0.1904 | 0.0000 | 0.8000  | 1.0000 |
| Fresh Water Marsh            | 16.1541 | 0.1364 | 0.0000 | 1.0000  | 0.0000 |
| Hardwood Forest              | 21.6245 | 0.3954 | 0.5685 | 0.2863  | 0.1234 |
| Mangrove Swamp               | 21.6074 | 0.2836 | 0.1000 | 0.6643  | 0.0000 |
| Forelands                    | 14.3082 | 0.2968 | 0.4932 | 0.4534  | 0.0434 |
| Dry Forest                   | 18.9514 | 0.4336 | 0.7648 | -0.0048 | 0.2429 |
| Cypress Swamp                | 15.7426 | 0.2046 | 0.2129 | 0.5479  | 0.2204 |

<sup>1</sup> Land cover types used in the Florida Land Cover Map (Florida Game and Fresh Water Fish Commission, 1992)

A geographic information system was constructed with NOAA AVHRR raw bands, monthly derived NDVI, surface temperatures, DSTV and Florida land use/cover map. Each of the data type was built as a data layer covering the study area in the GIS. The three weighting factors, NMC, and the interpolated potential ET, were also re-calculated and integrated into the GIS. The ET rates were then determined as the potential ET layer multiplying by the NMC layer for each of the grid cell in the GIS. Figure 4.16 illustrates the satellite derived and ground-based data layers and the calculation of ET in the geographic information system.



#### 4.3.4. Verification

Verification of ET from the remote sensing method was made with traditional ET methods and with parameter ET methods.

##### 4.3.4.1. Verification with traditional ET methods

The ET estimated by the remote sensing method versus ET estimated by traditional (Penman) method at 11 weather stations on the line depicted shown in Figure 4.17. Their relationship can be shown as

$$ET_{RS} = 1.823 ET_{Penman} - 0.702, \quad r^2 = 0.647, n = 21$$

where  $ET_{RS}$  is the remote sensing method ET, and  $ET_{Penman}$  is the Penman method ET.

The correlation coefficient does not indicate a strong relationship between the remote sensing ET and the traditional method ET. However, after a close inspection of the weighting factors and the VMC of the stations, an anomalous VMC value was found at station JRT3 (Jag Bay Weather Station, 15° 13' N, 80° 27' W). Station JRT3 was located at the southern tip of the Everglades National Park adjacent to the Florida Bay. Due to the low cultural efficiency of water, JRT3 displayed H2O values below zero that produced VMC values for JRT3 much lower than the crop coefficient used for mangrove swamp in traditional ET calculation. The relationship of remote sensing ET and the traditional method ET was re-evaluated excluding the five JRT3 points, and the relationship becomes

$$ET_{RS} = 1.095 ET_{Penman} - 0.888, \quad r^2 = 0.783, n = 16$$

The correlation coefficient was significant to indicate a positive relationship between the ET estimated by the remote sensing method and by the traditional method.

The NDVI-GSFF method can not be used with open water surface due to the negative NDVI which results in a negative WMC in the calculation. However, this problem is not difficult to solve, since water bodies are easily identified by remote sensing techniques. WMC values can be assigned to open water surfaces.

Locations located at the boundary of a large water body can create highly variable results due to large pixel scale and spectral signature mixing. The large ground coverage of satellite sensor could significantly the best use of water bodies as water if there is a high percentage of water present within the area of satellite field of view.

#### 4.3.4.3 Validation with lysimeter ET

Remote sensing estimated ET were compared with the lysimeter water balance ET. Tables 4.11 and 4.12 compare the remote sensing method estimated ET and the lysimeter measured ET for wetgrass and cereal, respectively.

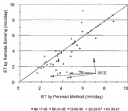


**Figure A.27** IT estimated by the remote sensing method versus IT estimated by the traditional (Perron) method on the five days. IT values at the Jet Day weather station (JETS) on the five days were identified.

Table 4.11: Eysenckian recorded ET and remote sensing estimated ET for wetgrass marsh area in four days

| Date       | Eysenckian<br>ET<br>(mm/day) | Peiman<br>ET <sub>0</sub><br>(mm/day) | NDVI            | DETV            | VMC  | R. S.<br>ET<br>(mm/day) | Error<br>ET (%) |
|------------|------------------------------|---------------------------------------|-----------------|-----------------|------|-------------------------|-----------------|
| 08-15-1994 | 9.84                         | 9.98                                  | 0.34            | 11.44           | 0.91 | 9.40                    | -4.36           |
| 08-24-1994 | 9.33                         | 9.45                                  | 0.34            | 13.42           | 0.85 | 8.55                    | -14.9           |
| 08-28-1997 | 9.30                         | 9.32                                  | NA <sup>1</sup> | NA <sup>1</sup> | —    | —                       | —               |
| 08-30-1997 | 9.39                         | 8.38                                  | 0.33            | 11.33           | 0.87 | 9.74                    | 3.83            |

<sup>1</sup> cloud contaminated

Table 4.12: Eysenckian recorded ET and remote sensing estimated ET for wetland marsh in four days

| Date       | Eysenckian<br>ET<br>(mm/day) | Peiman<br>ET <sub>0</sub><br>(mm/day) | NDVI | DETV  | VMC  | R. S.<br>ET<br>(mm/day) | Error<br>ET (%) |
|------------|------------------------------|---------------------------------------|------|-------|------|-------------------------|-----------------|
| 08-08-1994 | NA <sup>1</sup>              | 9.98                                  | 0.33 | 10.52 | 0.89 | 9.33                    | —               |
| 08-24-1994 | 8.38                         | 9.43                                  | 0.33 | 12.35 | 0.94 | 9.30                    | -10.14          |
| 08-28-1997 | 4.54                         | 9.33                                  | 0.33 | 12.54 | 0.94 | 9.04                    | -51.55          |
| 08-30-1997 | 8.43                         | 8.34                                  | 0.33 | 12.47 | 0.89 | 4.60                    | -44.95          |

<sup>1</sup> no Eysenckian record available

As shown in Table 4-11 and 4-12, the average error of remote sensing and lysimeter recorded ET reach 21 and 14-19 percent for anagras and canal, respectively. The largest estimation error (-21.92%) was with the canal lysimeter on March 28, 1997. On that date, the satellite image pixel at the canal lysimeter location was not identified as cloud-contaminated while the anagras pixel was. However, the NDVI of the canal was significantly lower than the average NDVI from other dates. The cause of the low NDVI value might be due to the existence of this cloud which was not detected by the cloud screening algorithm. The low NDVI resulted in a low YMC and consequently a low estimated ET. If we assumed this pixel was also contaminated by cloud-screen and excluded from the error calculation, the average error reduced to 10-15 and 5-1 percent for canal lysimeter and for the two lysimeters combined, respectively.

The existence of clouds was a significant problem in applying remote sensing methods for regional ET calculation. In the NDVI-MDSTY algorithm, both day- and night-time satellite images must be cloud-free in order to correctly derive the diurnal surface temperature variation. However, most of the NOAA AVHRR satellite images contain some clouds over an assessed area. This situation is particularly severe in the summer and fall seasons and, in most night satellite images, low cirrus clouds and fog are present in the images. In fact, there is no cloud-free-day-and-night Florida image pair in the more than seventy NOAA AVHRR images studied in the period from July and September, 1996.

The YMC values of the three corners of the NDVI-MDSTY triangle are important in determining YMC at each pixel. The two mid-day land YMC were assumed to be 0.59 and 0.61, respectively as the high and low actual ET to potential ET ratios for the entire year



However, VMC should be determined at least on a seasonal basis. Average monthly ratios of actual to potential ET in a long-term lysimeter study from north-west to south Florida could provide a more reliable monthly VMC for the ET assessment in Florida.

#### 4.7.7 Regional ET in South Florida

Regional ET in south Florida was calculated by using the VMC and the potential ET layers in the GIS. The ET contour map is plotted in Figure 4-28. ET contour map of interpolated ET on May 30, 1994 is also plotted in Figure 4-29.

As shown in both Figures 4-28 and 4-29, the highest ET rates appear over the Lake Okechobee. However, the interpolated ET in traditional method displays a higher value along the FFWMD boundary due to the extrapolation from further distance away ET contour map by the remote sensing method, on the other hand, displays a more evenly distributed and detailed contour due to the spatially distributed VMC from remote sensing method. The pattern of excessive values along the interpolating boundary is more noticeable if there are fewer weather stations in the region.

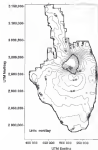


**Figure 4.28** Contour map of regional ET in south Florida by remote sensing method on May 30, 1997

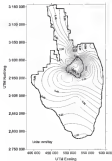


Figure 6.26 Contour map of regional ET in south Florida by interpolation of traditional ET method on May 30, 1997

## CHAPTER I CONCLUSIONS AND RECOMMENDATIONS

### 5.1 Conclusions

The hand-held spectroradiometer is useful in selecting the most efficient bands within the reflectance spectrum for discriminating between vegetation types. Spectrums measured in different months can be used to determine the optimal time span to perform land cover/cover classification of aerial images for areas with similar vegetation. In this study, the most efficient bands for vegetation and forest discrimination were blue/near red (425 to 675 nm), near infrared (715 to 800 nm) and first IR region (915 to 975 nm). As results shown in the measured reflectance comparisons, fall-early winter was the best season to distinguish wetland and vegetation. Hand-held radiometer measurements and satellite sensed data were found to have a higher correlation through vegetation indices as opposed to the raw spectral bands. By applying the ratio and difference, the vegetation indices can minimize the effects from different illumination and atmospheric attenuation and be able to produce a higher correlation between hand-held radiometer and satellite sensor. Normalized Difference Vegetation Index (NDVI) displayed the highest correlation among the vegetation indices studied.

Based on the results of maximal coefficient of variance (MCV) curves in this study, the optimum spatial resolution for classifying urban, agriculture, and wetlands is

Florida is 40–300 and 1200 m, respectively for the near infrared band. The optimum spatial resolution is 300, 400, and 1800 m for urban, agriculture and wetland, respectively, for the thermal infrared band. For south Florida, if only one resolution can be selected, the optimum spatial resolution is 300 m and 400 m for near infrared and thermal band, respectively. As in satellite imagery, these are the most appropriate resolutions to identify the land use categories for respective regions. A potential ET study using NOAA AVHRR thermal bands at a resolution close to the optimal spatial resolution resulted in a positive relationship between satellite and ground based ET.

Vegetation index and surface temperature extracted from the NOAA AVHRR data are related to the fractional vegetation cover and soil moisture content. A triangular shape appears by plotting various Florida land covers in the NDVI and the Diurnal Surface Temperature Variation (DSTV) scattergram. The three vertices of the triangle are agriculture, wetland, and urban for south Florida land use-cover types. By using the weighting factors derived from the NDVI and DSTV triangle relationship, the vegetation and moisture coefficients (VMC) can be calculated for areas with various vegetation covers and soil moisture contents.

The NDVI-DSTV triangle algorithm and the subsequently derived VMC were proven capable of estimating ET at a regional scale. Due to its fewer ground parameter requirements, the method developed in this study can be used for ET estimation over homogeneous land cover areas without the need for numerous ground stations. In other words, by choosing coefficients from three homogeneous land cover areas, one can then calculate values for areas with various vegetation cover and mixed soil moisture. If the

three cover types used in this study are not available, with this method, values from three other homogeneous land cover/cover areas can still be used.

### 3.3 Recommendations for Further Research

Vegetation species mapping is possible with high precision using spectral feature analysis of data from hand-held spectroradiometer. This information can be further applied to vegetation classification of multi-spectral data from two generations airborne or space-borne data.

Spectral reflectance of crops, natural vegetation, as well as different soil types and materials of Florida, can be measured from hand-held spectroradiometer reading, as a database of reflectance signatures. Such a database can be used as a knowledge bank to study the mixed spectrum in satellite images. A spectral unmixing model can then be applied to determine the components and percentage of vegetation species and soil backgrounds within each satellite pixel.

In order to establish reliable values of actual to potential ET, long-term ET study of wetland vegetation is recommended. These parameters should be developed locally and are important for the accurate application of remote sensing methods for the determination of regional ET estimates in Florida.

# APPENDIX I

## SPECTRAL REFLECTANCES OF NATURAL TARGETS IN FLORIDA

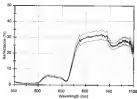


Figure A1-1 Spectral reflectance curves for low rate (Quartermaster) pigments. Solid line is the mean reflectance. The two lines are upper and lower 95% confidence intervals.



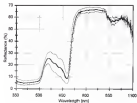


Figure 8.1.2 Spectral reflectance curves for slash pine (*Pinus elliottii*). Bold face line is the mean reflectance. The thin lines are upper and lower 95% confidence intervals.

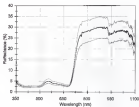


Figure A1-1 Spectral reflectance curves for Peak trees (*Mikolajewicz-palmgrenensis*). Solid line here is the mean reflectance. The two lines are upper and lower 95% confidence intervals.

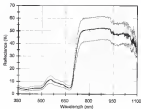
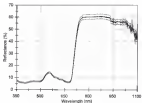


Figure A2-4 Spectral reflectance curves for sandpaper (*Dianzhipter-aspensicolaensis*). Solid line line is the mean reflectance. The two lines are upper and lower 95% confidence intervals.



**Figure 41-3** Spectral reflectance curves for a single-wavelength (monochromatic) source. Bold face line is the mean reflectance. The thin lines are upper and lower 95% confidence intervals.

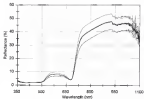


Figure A1-6 Spectral reflectance curves for green maize (*Cyperus (Cyperus) sp.*)  
 Solid black line is the mean reflectance. The thin lines are upper and lower  
 95% confidence intervals.

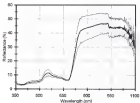


Figure A1-7 Spectral reflectance curves for sepius (*Sepioides*). Solid line line is the mean reflectance. The two lines are upper and lower 95% confidence intervals.

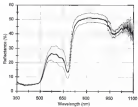


Figure A1-6 Spectral reflectance curves for new polymers (different types). Solid line is the mean reflectance. The two lines are upper and lower 50% confidence intervals.

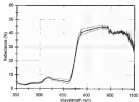


Figure A1-5 Spectral reflectance curves for casual. Bold line/line is the mean reflectance. The dashed lines are upper and lower 95% confidence intervals.



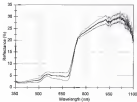


Figure A1.15: Spectral reflectance curves for St. Augustine grass (*Dactyloctenium aegyptium*). Solid line shows the mean reflectance. The thin lines are upper and lower 95% confidence intervals.

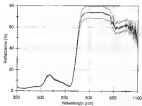


Figure A1-11 Spectral reflectance curves for Bilib lettuce. Bold line here is the mean reflectance

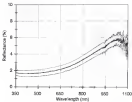


Figure A1.12. Spectral reflectance curves for dry rock wool. Solid line line is the mean reflectance. The two lines are upper and lower 95% confidence intervals.

## APPENDIX 2 PROGRAM CODES OF NOAA AVHRR PREPROCESSING

This is a group of programs written in C language to perform the NOAA AVHRR data extraction and image processing. The names of the subroutines and their functions are listed below.

1. **MAIN.CPP** : main program to manage all subroutines calls.
2. **EXPT.CPP** : subroutine to extract NOAA AVHRR raw image and header auxiliary data.
3. **FLIP.CPP** : subroutine to rotate a raw image file.
4. **SET.CPP** : subroutine to set the input and output parameters.
5. **ALBEDO.CPP** : subroutine to calculate surface albedo from NOAA AVHRR channel 1 and 2.
6. **TEMP.CPP** : subroutine to calculate surface temperature from NOAA AVHRR image channels 3, 4 and 5.
7. **GEOMIP.CPP** : subroutine to geo-rectify NOAA AVHRR image.
8. **COPY.CPP** : subroutine for image format conversion.

```

#
# NOAA/ASPT DATA AND IMAGE PROCESSING PROGRAM
#
#
# INCLUDE THE FOLLOWING FUNCTIONS
#
# 1 READ PACTED FILE
# 2 ROTATE IMAGE
# 3 ALIGNO-CALIBRATION
# 4 TEMPERATURE CALIBRATION
# 5 VEGETATION INDEX CALCULATION
# 6 FORMAT CONVERSION
# 7 GEOMETRIC CORRECTION
# 8 DOB SHELL
#
# Program Code: C++
# Author: C. H. Tan
# Version: 1.00
# Date: Jan 13, 1993

```

The following is the main program which call subroutines to implement the data extraction and image processing tasks

```

#
PROGRAM MAIN-CPP
#

```

```

# define included header files
#include <iostream>
#include <math.h>
#include <ctype.h>
#include <string.h>

```

```

# define external subroutines
extern void Read_IMAGE(void);
extern void Aligno(void);
extern void Vegetation_Index(void);
extern void Temperature(void);
extern void Psp(void);
extern void FLAS_Format(void);
extern void General(void);
extern void Set_File(char *);
extern void Set_Parameter(char *);

```

```

void Main_Help(void)
void Select_Command(void)

struct Header {
    int li, ll, ul, bl, rl, br;
} H;

FILE *out1,*out2,*out,*out3,*out4,*out5,*out6;
char out1_name[20],out2_name[20],out3_name[20],
out4_name[20],out5_name[20],out6_name[20];

void main(void) {
    struct H;
    printf("Welcome to NCMA486PT Data and Image Processing Program!\n");
    printf("Release/Versions : 04, Aug. 1992(Peter)",
    Main_Help(),
    Select_Command());
return;
}

void Select_Command(void) {
char *p; int i;
int i;
for(;;) {
    printf("\nPC-A&A-V7\n");
    p=getch(out);
    if(p!='\n'&&p!='\t') { out[i]=tolower(p);i++; }

    if(out[i]!='\n'&&out[i]!='\t'&&out[i]!='\r')
        Main_Help();
    else if(out[i]!='\n'&&out[i]!='\t'&&out[i]!='\r') {
        if(p=='\t') system("clear command out");
        else system(p+" ");
    }
    else if(out[i]!='\n'&&out[i]!='\t'&&out[i]!='\r'&&out[i]!='\r')
        Rand_FLOAT();
    else if(out[i]!='\n'&&out[i]!='\t'&&out[i]!='\r'&&out[i]!='\r')
        Pop();
    else if(out[i]!='\n'&&out[i]!='\t'&&out[i]!='\r'&&out[i]!='\r')
        A_Rotate();
    else if(out[i]!='\n'&&out[i]!='\t'&&out[i]!='\r'&&out[i]!='\r')

```

```

Temperature),
else if (val == "Kilometers") {
    Kilometers = Kilometers + 1;
}
Vegetation_Index(),
else if (val == "Kilometers") {
    Kilometers = Kilometers + 1;
}
Cover(),
else if (val == "Kilometers") {
    Kilometers = Kilometers + 1;
}
Kilometers(),
else if (val == "Kilometers") {
    Kilometers = Kilometers + 1;
}
else {
    print("Unknown command - " + val);
}

void Main_Menu() {
    print("\nHELP");
    print("\nHELP");
    print("\nKilometers");
    print("\nTemperature");
    print("\nVegetation Index");
    print("\nKilometers");
    print("\nCover");
    print("\nKilometers - command - the command - help");
    print("\nKilometers");
}
}

```

# SUBROUTINE TO EXTRACT NOMA HEFT RAW IMAGE AND RELATED AUXILIARY DATA

```

C PROGRAM HEFT.CPP

```

```

C Define included local files

```

```

#include <stdio.h>

```

```

#include <stdlib.h>

```

```

#include <string.h>

```

```

#include <ctype.h>

```

```

#include <math.h>

```

```

#include <unistd.h>

```

```

#define MPI_SIZE_M (assigned char 1,000,000,000)

```

```

void Read_HEFT(void)

```

```

void HEFT_Reader(void)

```

```

extern void Get_File(char *)

```

```

extern void Get_Parameters(char *)

```

```

extern struct Header { int d, B, m, b, m, b, } H;

```

```

extern FILE *fdata, *fcd, *fcd, *fcd, *fcd, *fcd,

```

```

void Read_HEFT(void) {

```

```

    int i,j,k,l,m,n,offset;

```

```

    long int size;

```

```

    int value[ MPI_SIZE_M/(512*1024) ];

```

```

    struct Hdr {

```

```

        unsigned d1: 10,

```

```

        unsigned d2: 10,

```

```

        unsigned d3: 10

```

```

        unsigned null: 2,

```

```

    } h;

```

```

    struct DM {

```

```

        long int;

```

```

        unsigned char ch[4];

```

```

        struct Hdr h;

```

```

    } dm[141*4];

```

```

    char read[ MPI_SIZE_M/(512*1024) ] = "NOMA-HEFT";

```







```

+factor(p+10^2561,+factor(p+11),
  atypep[i] = factor(p+10^2561^2561^2561,+factor(p+17^2561^2561,
    +factor(p+10^2561,+factor(p+15),
    fact[i]=2*fact(atypep[i])/10^2561424
    fact[i]=2*fact(atypep[i])/4+10/104,
    p+=6
  }
  fact.remaining=factor(10),
  for(i=0,+fact.remaining; i++) {
    fact.val[i]=factor(p+10/2,
    fact.val[i]=2*factor(p^4+100^2561+factor(p^4+107)/124
    fact.val[i]=3+124+factor(p^4+100^2561+factor(p^4+107)/p+10,
    }
  for(i=0,fact.n,for(j=fact(i),j,fact(i),
  fact.val,
  }

```













SUBROUTINE TO CALCULATE NARROW BAND ALBEDO IN NOAA SURF  
CHANNEL 1 AND 2

```

//
PROGRAM ALIBED0.CPP

//define matched local file
#include <stdio.h>
#include <ctype.h>

void Alibed0(void)
{
    extern void Set_Finisher ();
    extern void Set_Personnel(char *);
    extern struct Worker { int d, l, m, h; int hr, fr, } W;
    struct FILE *wfl, *wfl1, *wfl2, *wfl3, *wfl4, *wfl5,
    struct char wfl1_name[20]

    void Alibed0(void) {
        float alibed0[2][2048];
        int ab[1][2048];
        unsigned char alibed0[2][2048];
        int i,j,k,l,m,n,o,p,q,r,s,t,u,v,w,x,y,z;
        char wfl[20] "alibed0"-"MOAA-ALIB0",
        struct BAPT_HLAD {
            int day;
            int year;
            int julian;
            float time;
            float h[4];
            float l[4];
            int morning;
            int night[2];
            float day[11];
            float lat[11];
        } local;

    int j {
        printf("alibed0" "path");
        printf(wfl);
        float f=0.0; float i=0; float j=0.0; float k=0.0;

```

```

d[cond[0]]:=a.discard[1]--? let_fil[patk]
else d[cond[0]]:=a.discard[1]--? let_parameter[patk]
else d[cond[0]]:=a.discard[1]--? a.discard[1]--? ) (
  print "v4MP      set parameters";
  print "v4MP      set superoutput fil";
  print "v4M[5]      out";
  print "v4M4,MP  up- 5 to screen, 1 to test fil";
  print "v4M[X]      out";
  print "v4M[ELP]   the help message";
  print "v4valfil.  *DFT+image data, *DFT+test fil, "
    "OUP+output ( ) test(x)";
  print "  OUP+output (H type), OUPD+test dump "
    "T+superout fil(x) );

else d[cond[0]]:=a.discard[1]--? a.discard[0]--? ) (

  print "warning      ";
  element:=H in fil+1;
  for i in 0..H-1,
  do i:=H-1 fil(x)++ ) (
    print "v4M4,MP  OUP+?,"P400,fil(x)
    for j:=0..2*cond++ ) (
      d[cond[0]]:=element,out[0];
      d[cond[0]out:=d[cond[0]MP+_M4M[0],out[0];
      for j:=0..2*element++ ) (
        d[cond[0]]:=d[0][0]*cond[0]*cond[0];
        d[cond[0]]:=cond[0] out d[cond[0]] );
        d[cond[0]out[0] 4,element,out[0];
        d[cond[0]out[0] 4,element,out[0];
        for i in 1..4,element,M4M[0] OUP);
        d[cond[0]1, d[cond[0]2];
      )
    )
  )
else d[cond[0]]:=a.discard[1]--? a.discard[0]--? a.discard[0]--? ) (
  out[0]:=superout[0],name,"v4";
  for j:=0..2*cond++ ) (
    d[cond[0]out[0] 4,element,out[0];
    d[cond[0]out[0] 4,element,out[0];
    d[0]--? ) (
      print out[0], "v4out  Cb1  Cb2 ... "
        "v4v44444" fil(x);
      for j:=0..2*element++ ) (
        print out[0], "v4out  %d 2" MP fil(x),
          j+H as d[cond[0]]1, d[cond[0]]2 );
    )
  )

```

```

else {
    printf("%dPrint Out C1 C2 for %dAFor",
           B, B-1);
    B--;
    printf("%dPrint Out C1 C2 for %dAFor",
           B, B-1);
    B--;
}
}
else if (cond[0] == 'x' || cond[1] == 'x') cond[0] == '0'; return;
else printf("Unknown command: %s\n", cond);
}

/*for loop
/*program

```

# SUBROUTINE TO CALCULATE RADIANT TEMPERATURES FROM NOAA IRPT IMAGE CHANNELS 1, 4 AND 5

```

C     PROGRAM TEMP-RT

C     Define included head files
#include <stdio.h>
#include <stdlib.h>
#include <string.h>
#include <ctype.h>
#include <unistd.h>
#include <math.h>

void Temperature(void)
{
    extern void Set_File(char *);
    extern void Set_Parameter(char *);
    extern void Read(char *, int *, int *, int *, int *, int *);
    extern FILE *Get_Fmt(char *, char *, char *, char *, char *, char *)
    extern char *Get_Name(int)

    void Temperature(void) {

    float Temp[4][2048];
    unsigned char Temp_A[4][2048];
    int ch[4][2048];
    int i,j;
    counter=0;
    char cmd[256] *;
    flag=0;
    path[256]="/NOAA/IRPT/";
    float c1=1.736860e-5;
    float c2=1.438775e-3;
    float k[4][2048];
    float IRPT_READ [
        int line;
        int year;
        int julian;
        float time;
        float Q1;
        float Q2;
        int missing;
        int solar[3];
        float loc[14];
        float lat[14];
    ] local;
}

```





## SUBROUTINE TO GEO-RECTIFY NOAA AERIAL IMAGE

```

10      sub routine to geo-rectify a image with the Earth Locations extracted from the
      NAFT header. Also include subroutines to convert from Lat/Lon coordinates to
      UTM, affine transformations, and resampling.

40

80      PROGRAM GEORIP.CPP

100
110      ! define included local files
120      !include <stdio.h>
130      !include <stdlib.h>
140      !include <string.h>
150      !include <ctype.h>
160      !include <math.h>
170      !include <math.h>

180      void Geoaff(float)
190      double UTM_N,UTM_E,
200      double X[5]
210      int i,j,pxs,pye,
220      long int n,ms,ls,
230      char sample;
240      void LL_to_UTM(double double),
250      void Control_Point(void),
260      void Affine(void),
270      void Resample(void),
280      void readn(double, double, int),
290      unsigned char Read_UShort(int),
300      int read_int(FILE,char *),
310      int read_int_Parameter(char *),
320      int read_header (int n, int, int, int, int, int, int, int),
330      int read_FLE (int, int, int, int, int, int, int, int),

340      void Geoaff(void) {
350      int i,
360      char read[255] *p "ndpms,pxs,pye" "NOAA-GEORIP",

370      for(i,1)
380          printf("%d\n",pxs)

```











```

    g1=gd**2;
    g2=gd**2;
    B1 = gd**2*gd**2*(1+gd**2+11 *gd**2+gd**278 *gd**2+110 *gd**2*gd)
        *gd**28**2 / 128;

    B2 = gd**2*gd**2*gd**2*(1+18 *gd**2+gd**14 *gd**2*gd**58 *gd**2*gd)
        *gd**28**2 / 128;

    LTM4_N = (1+D**2+12**2+dB1
    dJacobian=0;
    LTM4_L = 100000-(2*N**2+4*N**2+dB1);
    else
    LTM4_L = 100000-(2*N**2+4*N**2+dB1)

return;
}

void Affine(void) {
    int ReadRow=0,L,point=0;
    double random_x,random_y,control_X,control_Y,B1,B2,B3,random_x;
    double A[1][1] ATA[1][1] A[1][1];
    double LB[1][1] V[1][1];
/* random matrix */

    for(row=0,row<L,row++) {
        A[0][row]=X[row]*0;
        for(col=0,col<L,col++) { ATA[row][col]=0; }
    }
    for(row=0,row<L,row++) {
        LB[row]=V[row]*0;
        for(col=0,col<L,col++) { A[0][row][col]=0; }
    }

/* read common points from input data file */
/* form A, LB, ATA, ATE matrix*/

do {
    Read=ReadData("N2P4P12P12" ,control_X,control_Y,
                    random_x & random_y);
    dJacobian=0;Read;

    A[0][0]=A[0][0]+1
    A[0][0]=A[0][0]+random_x;

```

```

A[0][0] ← A[0][0] * random_y;
A[0][1] ← A[0][1] * A[0][0] * 0.5;
A[1][0] ← A[0][0] * A[0][1] * 0.5;
L[0] ← control_X;
L[1] ← control_Y;

for (row = 0; row < 4; row++) {
    for (col = 0; col < 4; col++) {
        for (k = 0; k < 4; k++) {
            ATA[row][col] += A[k][row] * A[k][col];
        }
    }
}

for (row = 0; row < 4; row++) {
    for (k = 0; k < 4; k++) {
        ATL[row] += A[k][k] * row * L[k];
    }
}

} while (break == 0);
/* insert ATA, multiply inserted ATA by ATL to get X^2 */
memset(X, 0, 4);
for (row = 0; row < 4; row++) {
    X[row] = 0;
    for (col = 0; col < 4; col++) {
        X[row] += ATA[row][col] * ATL[col];
    }
}

// read in common points again, calculate residuals
memset(off, 0, 4);
do {
    break = 0;
    off[0] = (X[0] * off[0] + X[1] * off[1] + X[2] * off[2] + X[3] * off[3]) / (control_X * control_Y);
    break = random_y;
} while (break == 0);
A[0][0] ← A[0][0] * 0.5;
A[0][1] ← A[0][1] * random_y;
A[1][0] ← A[0][1] * random_y;
A[0][0] ← A[0][0] * A[0][1] * 0.5;
A[1][0] ← A[1][0] * A[0][1] * 0.5;
L[0] ← control_X;

```

```

L[1]=control_Y,

for (k=0;k<=L[k+1]) {
  Y[k]=0,
  for (j=0;j<=L[k+1]) {
    Y[k]=+A[k][j]*Y[j],
    Y[k]=+L[k]
  }
  Sum_sqr=(Y[k]**Y[k])+Y[k]**Y[k],
  pow=pow*
} while (head!=0)

// calculate standard error of var. weight

SE=sqrt(Sum_sqr/(head*(2**pow-1)),

// calculate standard errors of transformation parameters

for (row=0;row<=L;row++) { SE[row]=SE*sqrt(NTA[row][row]), }

printf("\nTRANSFORMATION PARAMETERS AND THEIR STANDARD
ERRORS ARE")
printf("Mapping Parameter      Standard Error")
printf("-----")
for (j=0;j<=L;j++) {
  printf("varial =%d (1) 7%varial =%d (2) 7%varial =%d (3) 7%varial =%d (4)",
for (j=0;j<=L;j++) {
  printf("varial =%d (1) 7%varial =%d (2) 7%varial =%d (3) 7%varial =%d (4)",
printf("\nSTANDARD ERROR OF UNIT WEIGHT = %d (4) SE",

return,
}

void main(void) { A[5][5]
{
  int i,j,k;

  for (k=0;k<=L;k++) {
    for (j=0;j<=L;j++) {
      A[k][j]=+A[k][j]+1, }
    }
    A[k][k]=+1, NTA[k]

```

```

for (i=0; i<N; i++) {
    if (i % 2) {
        for (j=0; j<N; j++) {
            if (j % 2) { A[i][j] = A[i][j]*A[i][j]; }
            A[i][j] = -A[i][j];
        }
    }
}
return;
}

void RunGraph() {
    int i, j, n, m;
    float t, p;
    unsigned char *a; a=(255);

    printf("HOW MANY LINKS IN GRG-CORRECTED IMAGE ?"),
    scanf("%d", &i), _getc();
    printf("HOW MANY ELEMENTS IN GRG-CORRECTED IMAGE ?"),
    scanf("%d", &m), _getc();
    printf("ADDRESS: ");
    for (j=0; j< i; j++) {
        printf("%d", &A[j][0]); printf(" ");
        for (j=0; j< m; j++) {
            n=(i*(j-0))+(j-0); m=(i*(j-1))+
            (j-1);
            p=(i*(j-0))+(j-0); q=(i*(j-1))+
            (j-1);
            if (p%2) { if (q%2) { a[p]=1; a[q]=0; } else {
                if (sample=="T") {
                    printf("ADDRESS = to be fixed\n");
                    return;
                }
                else if (sample=="F") {
                    printf("ADDRESS = to be fixed\n");
                    return;
                }
            } else { a[p]=Fixed_DP(a,p);

```

```

        }
        if (is_a_ptr)
            return (is, 1, a_ptr, null);
    }

    return 0;
}

unsigned char Read_Disk(int x, int y)
{
    long int disk;
    unsigned char ch;
    disk = (is_P) * 1;
    disk = disk * 10 + is_P;
    disk = disk * 10 + is_P;
    disk = disk * 10 + is_P;
    disk = disk * 10 + is_P;
    return disk;
}

```



## SUBROUTINE FOR IMAGE FORMAT CONVERSION

(\* The following is a subroutine to read PCDAAS (DEPT) images to BLAS file format  
PROGRAM LIBBY CPU

\*)

!> define included head files

include <ctype.h>

include <stdio.h>

define swap(x,y) {unsigned char t,x=a,b; t=x;}</p>
</div>
<div class="Text" data-bbox="102 370 519 460">
<p>void BLAS\_Format(void)<br>
{<br>
 struct read\_bin\_file{char \*,<br>
 struct read\_bin\_Parameters{char \*,<br>
 struct read\_header { int a, b, m, b0, m0, b1 | B,<br>
 where FILE \*mf1,\*mf2,\*mf3,\*mf4,\*mf5,\*mf6,</p>
</div>
<div class="Text" data-bbox="102 496 459 677">
<p>void BLAS\_Format(void) {<br>
 int i,j,m,dimension,<br>
 struct read{<br>
 int arg,<br>
 unsigned char b[2],<br>
 | m[10240],<br>
 unsigned char m0[10240],<br>
 unsigned char bin\_head[1024]<br>
 char read[10] \*p\_path[10]="PCDAAS-BLAS",<br>
 FILE \*mf1,\*mf2,\*mf3</p>
</div>
<div class="Text" data-bbox="102 696 750 934">
<p>for(i=1)<br>
 printf("mf1a>"\_path)<br>
 p=fopen(mf1)<br>
 for(j=1;j<26;j++) { printf("reading(mf1) j: ")<br>
 d[read(j)]=fgetc(p);d[read(j)]=fgetc(p);for (i=1;i<26;i++)<br>
 the d[read(j)]=fgetc(p);d[read(j)]=fgetc(p);for (i=1;i<26;i++)<br>
 the d[read(j)]=fgetc(p);d[read(j)]=fgetc(p);d[read(j)]=fgetc(p);<br>
 printf("mf2" int parameters (for output file)<br>
 printf("mf3" int outputoutput file">
 printf("mf4BLAS" "BLAS file format parameters">
 printf("mf5" n=1:2 bytes input, 1 byte output">
 printf("mf6" n=1:2 bytes input, 2 bytes output">
 printf("mf7" n=1:3 bytes input, 1 byte output">
</p>
</div>



```

else { if i type in, i type out
        thread(i, i, H, H*element, out);
        Forked(i+1, H, H*element, out, T1, 2)
    }
}
else if (out[i] == H*element[i]) return;
else printf("Element mismatch! %d\n", out[i]);
} //for loop
} //program

```

## APPENDIX 3

### ALGORITHM AND SOURCE CODE FOR TRADITIONAL SE CALCULATION

### Modified FAO-Penman Method

The original FAO-24 Penman combination method (Gowerdon and Penst, 1973) was revised by several authors in the late 90's. The modified Penman combination equation has the form

$$\lambda E T = \frac{R}{\Delta + \gamma} (\Delta R_a - G) + \frac{\gamma}{\Delta + \gamma} a_w W_f (e_d^0 - e_a)$$

$$W_f = u_a + b_w u_w$$

where  $\lambda$  = latent heat of vaporization ( $\text{MJ kg}^{-1}$ )

$\Delta$  = slope of vapor pressure curve ( $\text{kPa}^\circ\text{C}^{-1}$ ),

$\gamma$  = psychrometric constant ( $\text{kPa}^\circ\text{C}^{-1}$ ),

$R_a$  = net radiation ( $\text{MJ m}^{-2} \text{d}^{-1}$ ),

$G$  = ground heat flux ( $\text{MJ m}^{-2} \text{d}^{-1}$ ),

$u_a$  = wind speed at 2-m height ( $\text{m s}^{-1}$ ),

$a_w, b_w$  = wind function coefficients

### Latent Heat of Vaporization

Latent heat of vaporization was estimated by equation as follow:

$$\lambda = 2.504 - 2.341 \times 10^{-5} T, \text{ MJ kg}^{-1}$$

where  $T$  = air temperature ( $^\circ\text{C}$ )

### Saturated Vapor Pressure

The saturation vapor pressure was estimated by

$$e^* = \exp\left[\frac{16,780P - 11,637}{T + 237.3}\right], \text{ kPa}$$

where  $T$  = air temperature ( $^{\circ}\text{C}$ )

#### Slope of the Saturation Vapor Pressure Curve

The slope of the saturation vapor pressure curve was calculated by differentiating the equation for saturation vapor pressure

$$\Delta = \frac{4293e^*}{(T + 237.3)^2}, \text{ kPa}^{\circ}\text{C}^{-1}$$

where  $e^*$  = saturation vapor pressure (kPa),

$T$  = air temperature ( $^{\circ}\text{C}$ )

#### Psychrometric Constant

The psychrometric constant,  $\gamma$ , represents a balance between the sensible heat gained from air and the sensible heat (transformed into latent heat) and was calculated as

$$\gamma = \frac{c_p P}{0.622 h}, \text{ kPa}^{\circ}\text{C}^{-1}$$

where  $P$  = atmospheric pressure (kPa),

$c_p$  = specific heat of moist air at constant pressure, 1.013 kJ kg $^{-1}$   $^{\circ}\text{C}^{-1}$ ,

$h$  = latent heat of vaporization (kJ kg $^{-1}$ )

### **Panama Wind Function**

The wind function used in the Panama combination equation was set the form presented by Wright (1942)

$$W_z = u_z = k_z u_2$$

$$u_z = 0.4 + 0.4 \exp \left[ - \left( \frac{z - 1.17}{10} \right)^2 \right]$$

$$k_z = 0.001 + 0.005 \exp \left[ - \left( \frac{z - 3.07}{10} \right)^2 \right]$$

where  $u_z$  = wind speed at  $z$  meter height ( $m s^{-1}$ ).

$D$  = day of the year

### **Pearley-Taylor Method**

The Pearley-Taylor method is an empirical relation-based equation with the following general form (Pearley et al., 1990)

$$\lambda ET = a \frac{h}{h + \gamma} (R_a - Q)$$

where  $\lambda$  = latent heat of vaporization ( $kJ kg^{-1}$ )

$a$  = Pearley-Taylor constant

$h$  = slope of vapor pressure curve ( $kJ Pa^{-1} C^{-1}$ )

$\gamma$  = psychrometric constant ( $kJ Pa^{-1} C^{-1}$ )

$R_a$  = air radiation ( $kJ m^{-2} d^{-1}$ )

$Q$  = ground heat flux ( $kJ m^{-2} d^{-1}$ )

# Fennel-Monash-Christensen Method

The Fennel-Monash-Christensen method included a surface and aerodynamic resistance function to the Fennel equation:

$$A_s ET = \frac{a_s (E_s - E_a) + \frac{E_a}{\rho} (E_s - E_a)}{k + z^*}$$

where

$$a_s = \frac{\ln \left( \frac{z_{at} - d_s}{z_{ms}} \right) \ln \left( \frac{z_s - d_s}{z_{ms}} \right)}{k^2 u_s}$$

and

$$z^* = \rho \left( k + \frac{E_a}{u_s} \right)$$

where  $\rho$  = atmospheric density ( $\text{kg m}^{-3}$ ),

$u_s$  = speed of wind at ( $\ln \ln^{-1} u_{ref}$ ),

$k$  = aerodynamic resistance ( $\text{s m}^{-1}$ ),

$E_a$  = energy resistance ( $\text{J m}^{-2}$ ),

$z_s$  = height of the wind speed measurement (m),

$z_{at}$  = height of the humidity and temperature measurement (m),

$z_{ms}$  = roughness length for momentum transfer (m),

$z_{hs}$  = roughness length for vapor transfer (m),

$u_{ref}$  = wind speed at height  $z_{ref}$  ( $\text{m s}^{-1}$ ),



$k$  = von Karman's constant, 0.41 (dimensionless)

Some of the parameters can be computed as follows:

$u_{\text{ref}}$  = 0.125  $h_a$ ,  $h_a$  = mean height of crop canopy in cm,

$u_{\text{ref}}$  = 0.1  $u_{\text{max}}$

$d$  = (20)  $h_a$

### FAO Blaney-Weiss Method

The FAO Blaney-Weiss method is based on the general linear relationship found between measured reference ET and the Blaney-Weiss  $f$  factor for many worldwide sites that were investigated (Blaney and Weiss, 1927)

$$ET = a + bf$$

$$f = p (24 - T + 8.13)$$

$$a = 0.0043 RH_{\text{max}} - a/N + 1.43$$

$$b = 0.02 + 0.43 \times 10^{-5} RH_{\text{max}} + 10^{-5} (a/N) + 0.001 U_2$$

$$= 0.001 + 10^{-5} RH_{\text{max}} (a/N) + 0.001 + 10^{-5} RH_{\text{max}} U_2$$

where  $p$  = mean daily percent of annual daytime hours,

$a/N$  = related to possible maximum hours,

$RH_{\text{max}}$  = maximum relative humidity,

$U_2$  = mean daytime wind speed (in  $\text{m}^2$ )

## BT PROGRAM INPUT DATA FORMAT

| Line | Parameter   | Units   |
|------|---|---|
| 1    | Month, Day  | ()  |
| 2    | Latitude, Longitude,<br>Elevation   | decimal degree<br>m   |
| 3    | Solar radiation, Net radiation  | $\text{kJ m}^{-2} \text{d}^{-1}$                            |
| 4    | Air temperature,<br>Mean air temperature difference ( $T_{\text{air}} - T_{\text{air}}$ ) | $^{\circ}\text{C}$<br>$^{\circ}\text{C}$                    |
| 5    | Minimum relative humidity<br>Minimum relative humidity<br>Mean relative humidity          | %<br>%<br>%   |
| 6    | Atmospheric pressure  | kPa   |
| 7    | Wind speed at 2 meter height<br>Mean day-time wind speed<br>Mean night time wind speed    | $\text{m s}^{-1}$<br>$\text{m s}^{-1}$<br>$\text{m s}^{-1}$ |
| 8    | Pan evaporation   | $\text{mm day}^{-1}$  |
| 9    | $\alpha$ in the Blaney-Childs equation  | ()  |
| 10   | Grass fresh   | m   |
| 11   | Canopy cover  | $\text{cm}^2$   |
| 12   | Height of wind measurement  | m   |
| 13   | Height of humidity and temperature measurement  | m   |
| 14   | Crop height   | m   |

## RT Estimation Computer Program

```

//
//      Exponential Decay Calculation by
//      1. Purnan Method
//      2. Blumy-Cordis Method
//      3. Fick-Pan Exponential Method
//      4. Purnan_Monroth Method
//
//      Programmer:   Chih-Hung Yen
//      Date:         Oct.19, 1999 (version 1.00)
//

#include <stdio.h>
#include <stdlib.h>
#include <math.h>

#define PI 3.14159
#define Cp 1.00 /* specific heat of moist air, kJ/kg/C */

// declare global functions
void Read_Data(),
void Blumy_Cordis(void),
void Purnan(void),
void Fick_Pan(void),
void Purnan_Monroth(void),

// declare global variables
float Ra, Rb, Rf, Rfmax, Rfmin, Rfmean, x0, U1, U2, U3, P,
m, DPF,
float Lat=17.5, Elev=15, par=1.1,

void main(void) {
    Read_Data(),
    Purnan(),
    Blumy_Cordis(),
    Fick_Pan(),
    Purnan_Monroth(),
    graph()
}

void Read_Data(void) {

```



```

if print_gammas=1d 10d gammas,
if print_w=1d 10d w,
if print_bw=1d 10d bw,
if print_W0=1d 10d W0,
if print_U0=1d 10d U0, j(dims)(dims+gammas),
if print_c=1d 10d c,
if print_Fmax=1E9 = 1d 1E9 maxlog10_Fmax,
if print_F_min=1E0 = 1d 1E0 minlog10_F_min,

```

```

}

```

```

void Runny_Collide(void) {
    float d, p, A, B, C, EE;
    float L1, ddx, w, wdx, w0,
    float A1, B1, C1;
    int i;

    Runny_Collide_p=0; {
        ddx=0.0001*max( W0*(100 - C*(100)),
            w-w0*max(Lar*F0000 / max(ddx),
                W-w0*(24.75),
                w0d=0);
    }
}

```

```

A=0d 1d-0.75*Lar+0.0001*W0;
B=0d 1d+0.001*Lar+0.0001*W0;
C0=A-B*max( W0*(100-100) - C*(100),
if print_A=1d 10d A,
if print_B=1d 10d B,
if print_C0=1d 10d C0,
if print_c=1d 10d c,

```

```

ddx=0.0001*max( W0*(100 - C*(100)),
    w-w0*max(Lar*F0000 / max(ddx),
        W-w0*(24.75),
        p=W*(100-0.0001)

```

```

d(Wmax=100) B(Wmax=100),
d(Wmax=0) B(Wmax=0),
d(A=0) w=W,

```

```

d(LD+10) = LD+10;
w=0.0007854*area*(w0/10);
b=0.02+0.004*(Hmax+1)*w0+0.0009*(d
+0.0007854*area*w0+0.0007854*area*Ld)
B_C_ET=w0*w0*0.40*area+0.10;
if
    printf("w=%d.2f\n",w);
if
    printf("b=%d.2f\n",b);
if
    printf("w0=%f.1f\n",w0);
if
    printf("b=%f.1f\n",b);
printf("B_C_dts ET0 = %d.2f mm/day\n",B_C_ET);

}

void FAD_Pan(void) {
    float kg, ETpan;
    float Fadh=1000;
    kg=0.075+0.00044*(L2+0.04)*Hmax+0.01*(F*Wadh
+0.00044*Hmax*Hmax+0.00044*(F*Fadh*Fadh
+0.0000004*Hmax*Hmax*L2+0.000001*Hmax*Hmax*Fadh);
    ETpan=kg*pan;
if
    printf("kg=%f.2f\n",kg);
    printf("F*Wadh*ET0 = %d.2f mm/day\n",ETpan);

}

void Panmax_Mountb(void) {
    float w,VPD,panmax,Delta,L,E,G=0.20;
    float ra,r,panmax,R,P,ht,ET;
    float L,ra0,ra for ra (g);
    ra=20; //saturated vapor (g/s) from Appendix 1 (M)
    ra=2000; //wind speed measured at height ra (mm)
    ap=100; //temperature & humidity measured at height ap (mm)
    ht=700; //mean crop height for cotton & sugarcane (mm)

    Ld=0.001+0.00140*pan;
    w = 2.617*log(17.27+ap/(pan+17.27));
    VPD=w*(1-(Ld*Hmax+Ld*Hmax/200));
    Delta = (4000*(w0/pan+17.27)*(pan+17.27));
    panmax = (E*P*(P0/P)/(1+0.5*Ld/P)/(E-1);
    w0=0.100*pa;
    w0=0.1*w0a;
    d=0.0007854;
    w=(log)(w0-d)/(d*log)(ap-d)/(d*(d+1)*47%ET);

```

```

R=1750-4.85*wt;

gammag=gammag[1+wt/R];

P_M_ET=4*(Delta*(Delta+gammag)*((Rn-G)+gammag*(Delta+gammag)*((Kex*VPC)/L),
//      print("R= %f L/Et" ,R);
//      print("n= %f Wt" ,wt);
//      print("gammag= %f Wt" ,gammag);
//      print("P_Mock ET= %f Wt n/Lapre" ,P_M_ET);

}

```

## LIST OF REFERENCES

- Ashtons, G. E., J. D. Harbeck and R. H. Reed, 1968. Evaluating Landsat-Thematic Mapper derived vegetation indices for estimating above-ground biomass on semiarid rangelands. *Remote Sensing of Environment* 43: 143-175.
- Ashby, D., and B. Keady, 1976. Estimation of sea surface temperature from space. *Remote Sensing of Environment*, 1: 217-226.
- Ashby, T. C., J. P. Gustafson, and A. Perren, 1986. HAPEX-MOULMET: A hydrologic atmospheric experiment for the study of water budget and evaporation flux at the domain scale. *Bulletin of American Meteorological Society*, 67: 118-140.
- Atala, D. A., and W. H. Carnahan, 1981. Survey of monthly variability in climograph of urban areas. *Remote Sensing of Environment* 12: 363-369.
- Avry, T. E., and G. L. Berlin, 1980. *Fundamentals of Remote Sensing and Airphoto Interpretation*. 2<sup>nd</sup> ed. Macmillan Pub. Co., New York. pp. 42.
- Barnes, T. J., A. McFarquay, D. E. Collins, E. W. Saunders, and D. T. Llewellyn-Jones, 1987. Theoretical algorithm for satellite-derived sea surface temperatures. *Journal of Geophysical Research* 94: 11445-11479.
- Barnes, T. J., 1983. Satellite-derived sea surface temperatures—A comparison between operational, theoretical, and experimental algorithms. *Journal of Applied Meteorology* 21: 433-440.
- Berkel, P. W. Nijm, and M. P. Jodl, 1981. An active method for measuring derived infrared effective radiativities. Implications and perspectives for remote sensing. *Advances in Space Research* 1: 173-216.
- Buckley, F. and E. L. Lu, 1986. Towards a local split window method over land surfaces. *International Journal of Remote Sensing* 11(2): 369-387.
- Bullard, W. E., W. M. Woodham, and M. A. Lopez, 1966. *Evapotranspiration from Areas of Minor Vegetation in West-Central Florida*. U. S. Geological Survey Water-Supply Paper 2436, p. 23.



- Blaney, H. F. and W. D. Criddle, 1950. Determining consumptive use for water developments. *ASCE Irrigation and Drainage Special Conference Proceedings*, No. 2-4, pp. 1-18.
- Boman, B. J., 1994. Evapotranspiration from young Florida Sawcane citrus trees, *Journal of Irrigation and Drainage Engineering*, 120(1):40-44.
- Born, I. S., 1928. The rate of heat losses by conduction and by evaporation from any water surface. *Physics Review*, 27(5):770-777.
- Bracewell, R. N., A. E. Siegman, D. R. Chafin, R. R. Hale, D. J. Dine, and A. W. Springman, 1985. Reflectance stability analysis of Spectradex diffuse calibration panels. *SPSE Proceedings: International Society for Optical Engineering*, 1490:132-142.
- Bria, L. J., E. T. Kottawa, and W. L. Powers, 1972. Evapotranspiration from upland and highland fields. *Agronomy Journal*, 64(2):142-148.
- Brutsaert, W., 1982. *Evaporation into the Atmosphere*, Reidel-Pub. Co., Dordrecht, Holland.
- Brutsaert, W., 1988. Canopy-scale evaporation and atmospheric boundary layer. *Water Resources Research*, 24(5):58-68.
- Burns, S. J. K. and C. D. Kays, 1961. The determination of infrared emissivity of terrestrial surfaces, *Journal of Geophysical Research*, 66(1):1375-1377.
- Carlson, T. N., and M. J. Huellen, 1991. On estimating multi-day evapotranspiration from remote surface temperature measurements, *Remote Sensing of Environment*, 29:207-227.
- Carlson, T. N., E. M. Perry, and T. J. Schumaker, 1990. Remote estimation of soil moisture availability and fractional vegetation cover for agricultural fields. *Agricultural and Forest Meteorology*, 51:45-67.
- Castles, W., J. A. Schiman, and F. Becker, 1988. Determination of the effective emissivity and temperature under vertical observation of a citrus orchard. Application to direct forecasting. *International Journal of Remote Sensing*, 9:715-727.
- Castles, W., J. A. Schiman, and C. Coll, 1992. On the use of satellite thermal data for determining evapotranspiration in partially vegetated areas, *International Journal of Remote Sensing*, 13(14):2697-2712.
- Chandrasekhar, S. 1960. *Radiative Transfer*, Dover Publications, New York.

- Challa, A., N. A. Smit, and A. Barua, 1992. A single-channel double-viewing angle method for non-invasive temperature determination from collection MCTEOMs and TROUS microarray measurements. *Journal of Applied Microscopy*, 21: 613-618.
- Cleaverly, B. J., 1987. Relationships between vegetation indices, vegetation absorption and net photosynthesis evaluated by a sensitivity analysis. *Remote Sensing of Environment*, 22:209-211.
- Cleaverly, B. J., R. J. Ragsdale, and L. B. Jahn, 1984. An analysis of selected temperature observations over wheat and calculation of latent heat flux. *Agricultural and Forest Meteorology*, 57:71-81.
- Chow, V. T., D. R. Maidment, and E. W. Mays, 1988. *Applied Hydrology*, McGraw Hill, New York.
- Christensen, J. E., 1968. Estimating net evaporation and evapotranspiration from climatic data. *ADC Irrigation and Drainage Division*, 94:283-285.
- Croft, H. B., 1970. The spatial collection of American soils. *Photogrammetric Engineering*, 36(5):595-598.
- Curtis, P. J., 1983. Multispectral remote sensing for the estimation of green leaf index. *Philosophical Transactions of the Royal Society of London, A*, 389:317-330.
- Curtis, P. J. and G. M. Paoli, 1994. Environmental issues at regional to global scales. In *Environmental Remote Sensing from Regional to Global Scale* (G. Paoli and P. Curtis, editors). John Wiley & Sons, New York. pp. 1-7.
- Curtis, W. R., and P. K. Rao, 1969. Gulf Stream thermal gradients from satellite, ship and aircraft observations. *Journal of Geophysical Research*, 74, 6564-6586.
- Cutler, J. L., 1987. The interaction effect of spatial resolution and degree of internal variability within land cover types on classification accuracies. *International Journal of Remote Sensing*, 8(1):11-25.
- Dawley, D. W., J. W. Rouse, R. E. Rasm, and J. A. Schell, 1975. Measuring large production of grazing units from Landsat MSS data. *Proceedings of the 19th International Symposium on Remote Sensing of Environment*, 2:1169-1176.
- De, L. and D. C. Rudolph, 1988. A one-step algorithm for correction and calibration of AVHRR Level 1b data. *Photogrammetric Engineering and Remote Sensing*, 54(1):161-171.

- Dong, G., and Z. Li: 1993, 'The apparent sensitivity of vegetation canopies', *International Journal of Remote Sensing*, 14(5) 103-118.
- Disarcino, J., and W. G. Peairs, 1977, *Guidelines for Predicting Crop Water Requirements*, FAO Irrigation and Drainage Paper No. 24, 2<sup>nd</sup> ed., FAO, Rome, Italy, 156 pp.
- Doran, J. C.: 1993, 'The sensitivity of flux parameterizations to surface characteristics', *Proceedings of the Third Atmospheric Radiation Measurement Science Team Meeting*, March 3-4, Norman, Oklahoma, U.S. Department of Energy, Washington, DC, pp. 75-80.
- Katman, I. B.: 1995, *EDRS for Windows User's Guide - The EDRS Project*, Clark User, Worcester, MA.
- Engman, E. T., and R. J. Gurney, 1991, *Remote Sensing in Hydrology*, Chapman and Hill, London, U.K., pp. 325.
- ERDA, 1995, *ERDA's Field Guide*, 7<sup>th</sup> ed., Atlanta, Georgia, pp. 68.
- Fernald, S. A. and D. J. Petron, 1994, *Water Resources Atlas of Florida*, Florida State University, Tallahassee Florida, pp.293.
- Florida Game and Freshwater Fish Commission, 1992, *Florida Land Cover - Mangrove Wildlife Program*, Office of Environmental Services, Florida Game and Freshwater Fish Commission, Tallahassee, FL.
- Gallo, K. P., C. S. T. Daugherty, and M. S. Easar: 1993, 'Spectral estimation of absorbed photosynthetically active radiation across an aquatic', *Remote Sensing of Environment*, 47 321-333.
- GEO, 1996, *GEOP 1300 Spectroradiometer User Manual*, Geophysical & Environmental Research Corporation, Millbrook, NY.
- Gillies, S. R., J. Cai, T. H. Carlson, W. P. Kuster and K. S. Humes, 1993, 'Implications of the NDVI and surface radiant temperature relationship', *American Meteorological Society Conference on Hydrology Properties*, January 15-20, Dallas, Texas, pp. 135-148.
- Graham, M. H., D. G. Jenkins, M. T. Kalos, B. W. Kalos, B. W. Freeman, and D. R. Seyler, 1993, *ELAS-Gate Receiver Laboratory Applications Software*, National Aeronautics and Space Administration, National Space Technology Laboratories, Mississippi.

- Griggs, M. 1968. Sensitivity of natural surfaces in the 8 to 14 micron spectral region. *Journal of Geophysical Research*, 73(24): 7034-7037.
- Gurney, R. J. and P. J. Canfield, 1984. Modeling daily evapotranspiration using remotely sensed data. *Journal of Hydrology*, 69: 305-324.
- Gurney, R. J. and D. E. Hall 1983. Satellite-derived surface energy balance estimates in the Alaska tundra-tundra. *Journal of Climate and Applied Meteorology*, 22(2): 103-120.
- Hartley, M. A., F. C. Dalzer, C. T. Korman, and Y. Korman, 1984. Remote sensing of biomass and annual net aerial primary productivity of a salt marsh. *Remote Sensing of Environment*, 14: 51-106.
- Hargreaves, G. H., 1964. Defining and using reference evapotranspiration. *Journal of Irrigation and Drainage Engineering*, 110(6): 1031-1139.
- Hartog, D. A., and W. J. Bailey, 1970. The Advanced Very-High Resolution Radiometer (AVHRR): A brief reference guide. *Photogrammetric Engineering and Remote Sensing*, 36(2):1031-1038.
- Hartfeld, J. L., E. T. Rasmussen, G. Auer, R. D. Jackson, P. J. Foner, R. J. Ragsdale, and S. B. Idso, 1980. Leaf area estimates from spectral measurements over various planting dates of wheat. *International Journal of Remote Sensing*, 1: 163-173.
- Hartfeld, J. L., A. Perera, and R. D. Jackson, 1983. Estimation of evapotranspiration at one time-of-day using remotely sensed surface temperatures. *Agricultural Water Management*, 7: 140-149.
- Hartfeld, J. L., R. J. Ragsdale, and S. B. Idso, 1984. Evaluation of canopy temperature-evapotranspiration models over various crops. *Agricultural and Forest Meteorology*, 32: 41-52.
- Holman, J. L., E. P. Karaman, W. J. Rouseby, and B. L. Ebel, 1978. Thermal water measurement of canopy temperature to estimate evapotranspiration. *Remote Sensing of Environment*, 9: 333-440.
- Hu, D., A. Auer, and P. Y. Deshaies, 1986. Atmospheric correction for air surface temperature using NOAA-T AVHRR and Météosat 2 infrared data. *International Journal of Remote Sensing*, 7: 1221-1233.
- Hulsh, R. M., C. J. Tucker, and C. J. Foa, 1980. Spectral assessment of soybean leaf area and leaf biomass. *Photogrammetric Engineering and Remote Sensing*, 46: 651-656.

- Hogg, A. S., and T. P. McIlwain, 1963. The relationship between surface temperature and a spectral vegetation index of a tallgrass prairie: effects of burning and other landscape controls. *International Journal of Remote Sensing*, 13: 2649-2661.
- Hogg, A.S., D.E. Fitzcald, E.M. Goward and R.M. Ragan, 1986. Combined analysis of canopy reflectance and thermal response for estimating evapotranspiration. In *Remote Sensing Applications for Agriculture and Environmental Management*. American Water Resources Association monograph series No. 5, pp. 1-11.
- Horton, D. N. B., M. Dooling, J. Rader, and A. R. Hartgering, 1985. Red edge measurements for remotely sensing plant chlorophyll content. *Advanced Space Research*, 1: 271-277.
- Hunt, A. R., 1984. A soil-adjusted vegetation index (SAVI). *Remote Sensing of Environment*, 31: 335-349.
- Hunt, A. R., R. D. Jackson, and D. F. Post, 1985. Spectral response of a plant-canopy with different soil backgrounds. *Remote Sensing of Environment*, 17: 23-33.
- Hunter, E., W. F. Ragan and T. J. Schlegel, 1963. Effects of soil moisture and ground insulation on the surface temperature/insulation index relationship for a tallgrass prairie. *American Meteorological Society Conference on Hydrology* Preprints January 15-19, Dallas, Texas, pp. 163-165.
- Hunt, G. E. 1975. Radiative properties of terrestrial clouds at visible and infrared thermal window wavelengths. *Quarterly Journal of Royal Meteorological Society*, 91: 345.
- Idso, S. B., R. D., Jackson, R. J., Reginato, 1973. Estimating evaporation: a technique adaptable to remote sensing. *Science*, 180: 954-957.
- Jackson, R. D., 1982. Soil moisture inferences from thermal infrared measurements of vegetation temperatures. *IEEE Transactions on Geoscience and Remote Sensing*, GA-20(3): 245-254.
- Jackson, R. D., P. J. Pinter, Jr., and R. J. Reginato, 1983. Net radiation calculated from remote multispectral and ground station meteorological data. *Agricultural Forest Meteorology*, 55: 133-144.
- Jackson, R. D., R. J. Reginato, and S. B. Idso, 1977. What canopy temperature: a practical tool for estimating water requirements. *Water Resources Research*, 13: 651.

- Jackson, R. D., P. N. Glaser, and P. J. Pinter, Jr., 1983. Documentation of ground-water stress in wheat by various vegetation indices through clear and turbid atmospheres. *Remote Sensing of Environment*, 13, 337-358.
- Jensen, M. E., 1968. Water consumption by agricultural plants. In *Water Deficits and Plant Growth*, (T. Kozlowski, ed.), Academic Press, New York, pp. 1-33.
- Jensen, M. E., R. D. Rasmussen, and R. G. Allen, 1990. *Evapotranspiration and Irrigation Water Requirements*. ASCE Manuals and Reports on Engineering Practice No. 79, American Society of Civil Engineering, New York.
- Jones, J. W., L. H. Allen, S. F. Sells, J. E. Rogers, L. C. Hammond, A. G. Samra, and J. D. Matfield, 1984. *Estimated and Measured Evapotranspiration for Florida Cereals, Crops, and Soils*. Technical Bulletin 693, Institute of Food and Agricultural Sciences, University of Florida, Gainesville.
- Kauf, R. J. and C. E. Thomas, 1979. The coastal map—A graphic description of the spatial-temporal development of agricultural crops as seen by LANDSAT. In *Proceedings, Symposium on Machine Processing of Remote Sensing Data*, Purdue University, West Lafayette, IN, pp. 489-513.
- Kerr, Y. H., J. Ingham, G. Dalrym, G. Hachem, J. P. Laguarda and E. Rogers, 1989. NOAA AVHRR and its use for rainfall and evapotranspiration monitoring. *International Journal of Remote Sensing*, 10(9):945-954.
- Kerr, Y. H., J. P. Laguarda, and J. Ingham, 1992. Advances in surface temperature retrieval from AVHRR, data with use of an improved split window algorithm. *Remote Sensing of Environment*, 41, 193-209.
- Kubick, C. B., 1991. *NOAA Polar Orbiter Data User's Guide*. NOAA/NEADS WDC02024, Washington, DC.
- Kusler, L. Jr., 1978. *Estimation of Evapotranspiration in the Rainbow Springs and Silver Springs Areas in North-Central Florida*. Water Resources Investigations Report 78-6024, U.S. Geological Survey, p. 37.
- Rouse, W. F., M. S. Mulla, R. D. Jackson, L. W. Gay, L. F. Daugh, K. E. Kutiel, A. D. Mathias, 1990. Relationships and daily values of the surface energy balance over agricultural fields using remote sensing and a reference field to an and environment. *Remote Sensing of Environment*, 33(3): 129-140.

- Laguarda, J. P.: 1980, 'Use of NOAA AVHRR data combined with an agro-meteorological model for vegetation mapping', *International Journal of Remote Sensing*, 1(5) 833-844.
- La Violette, P. E. and P. J. Chabon, 1968, 'Midwest II satellite sea surface temperatures versus historical data in a selected region: A comparative study', *Deep-Sea Research*, 15, 419-433.
- Latty, R. S. and R. M. Hoffman, 1981, 'Computer-based classification accuracy due to the spatial resolution using per-pixel versus per-field classification techniques', *Symposium of Machine Processing of Remotely Sensed Data*, pp. 344-352.
- Lillesand, T. M. and R. W. Kiefer, 1987, *Remote Sensing and Image Interpretation*, 2<sup>nd</sup> ed. John Wiley and Sons, New York, NY.
- Malaprade, J. P.: 1966, 'The vegetation index and the study of vegetation dynamics', in *Applications of Remote Sensing to Agrometeorology*, (P. Tardif, ed.), Kluwer Academic Pub., London.
- McClain, E. P., W. G. Pichel, C. C. Wilton, E. Altnad, and J. Nelson, 1983, 'Multichannel improvements to satellite-derived global sea surface temperatures', *Advanced Space Research*, 1, 43-47.
- McClain, E. P., W. G. Pichel, and C. C. Wilton, 1985, 'Comparative performance of AVHRR based multichannel sea surface temperature', *Journal of Geophysical Research*, 90, 11187-11600.
- McMillin, L. M.: 1975, 'Estimation of sea surface temperatures from two infrared window measurements with different absorption', *Journal of Geophysical Research*, 80(34-35) 8115-8117.
- Milano, M.: 1979, *Defining Relationships Between Surface Characteristics and Actual Evapotranspiration Rate*, Note 1146, Institute for Land and Water Management Research, Wageningen, The Netherlands.
- Miyahara, H. and W. Tobler: 1972, 'Geographical variance', *Geographical Analysis*, 4, 35.
- Munro, J. L.: 1973, *Principles of Environmental Physics*, American Elsevier Pub. Co., New York, 241 pp.
- Monterey, J. L.: 1981, 'Evaporation and surface temperature', *Quarterly Journal of Royal Meteorological Society*, 107, 1-27.

- Morse, M. S., R. D. Jackson, L. H. Reynolds, E. W. Gray, and P. W. Stein, 1989. Mapping surface energy balance components by combining Landsat Thematic Mapper and ground-based meteorological data. *Remote Sensing of Environment*, 30:77-87.
- Morse, M., S. T. B. Clark, Y. Liang, and A. Vidal, 1994. Estimating crop water deficit using the relation between surface-air temperature and spectral vegetation index. *Remote Sensing of Environment*, 40:149-158.
- Martin, P. A., 1975. Remote sensing and vegetation damage: a theory for detection and assessment. *Photogrammetric Engineering and Remote Sensing*, 44:1143-1158.
- Neftci, M. D., and J. M. Briggs, 1989. The effect of spectral scale on Kansas landscape classification using neural analysis. *Landscape Ecology*, 2:18.
- Nelson, R. L., and S. W. Running, 1989. Evaluation of regional surface resistance to evapotranspiration from NDVI and thermal IR AVHRR data. *Journal of Applied Meteorology*, 28:326-334.
- Nielsenhoist, G.F.A., E.H. Smith and H.A.M. Thomsen, 1985. Estimation of regional evapotranspiration of arable crops from thermal infrared images. *International Journal of Remote Sensing*, 6(3):1135-1154.
- Obeng, G., E. Galle, A. Goshen, W. Pagan, L. Brown, and J. D. Topping, 1995. Climate and Global change, Characterization of NOAA Satellite data. *JGIM*, 79(41):494-500.
- Omernik, J. P., B. J. Choudhury, and M. Goss, 1987. Vegetation spatial variability and its effect on vegetation indices. *International Journal of Remote Sensing*, 8:1107-1126.
- Pao, H. L., 1986. A single parameterization scheme of evapotranspiration over land for the NCEP medium-range forecast model. *Atmospheric Research*, 176:2506-2512.
- Pruefer, H. L., 1958. Microclimate over open water, bare soil, and grass, *Proceedings of the Royal Society, A*, 193(1002):126-145.
- Pruefer, H. L., D. B. Arpaci and C. H. M. van Bavel, 1967. Microclimate factors affecting evaporation and transpiration. Chapter 36. In: *American Society of Agronomy No. 74, Physiology of Agricultural Crops*. Madison, WI.
- Pury, C. R., Jr. and L. P. Luchtmeijer, 1984. Functional equivalence of spectral vegetation indices. *Remote Sensing of Environment*, 14:319-332.
- Pruitt, R. T., 1983. Determination of surface fluxes from satellite. *Advances in Space Research*, 9(3):311-341.



- Fisher, R. T., and J. A. Dwyer, 1988: Effect of surface properties on the narrow to broadband spectral relationship in clear sky satellite observations. *Remote Sensing of Environment*, 26: 247-261.
- Flann, W. G., 1988: *Data Acquisition and Calibration of DROS-ANCOG Radiometers*, NOAA Technical Memorandum FDSN-107, Washington, DC.
- Freidenreich, C., G. Dalu, and V. G. Kondo, 1978: Estimation of sea surface temperature from remote sensing in the 10-12  $\mu$ m window region. *Journal of Geophysical Research*, 79: 5039-5044.
- Frue, J. C., 1980: Estimating surface temperature from satellite thermal infrared data-a guide. Consideration for the atmosphere effect. *Remote Sensing of Environment*, 10: 211-261.
- Frue, J. C., 1984: Land surface temperature measurements from the split window channels of the NOAA/AVHRR. *Journal of Geophysical Research*, 89: 7010-7020.
- Frue, J. C., 1988: Using spatial context in satellite data to infer regional scale evapotranspiration. *EGU Transactions on Geoscience and Remote Sensing*, 26(3): 940-948.
- Frue, J. C. 1992: Estimating vegetation amount from visible and near infrared reflectances. *Remote Sensing of Environment*, 41: 25-34.
- Price, C. H. B., and R. J. Taylor, 1975: On the assessment of surface heat flux and evaporation using large scale parameters. *Monthly Weather Review*, 103: 81-82.
- Rastel, E., B. Lacroix, E. Maranda, and G. Delbecq, 1983: Comparison of hydrologically measured and remotely sensed actual evapotranspiration from some Quebecian vegetation formations. *International Journal of Remote Sensing*, 4: 1475-1481.
- Roe, W.G. 1976: *Physical Principles of Remote Sensing*. Cambridge University Press, Cambridge, New York, 187pp.
- Rogers, R.J., R.D. Jackson and P.J. Potts, Jr. 1983: Evapotranspiration calculated from remote multi-spectral and ground station meteorological data. *Remote Sensing of Environment*, 15: 75-89.
- Rogers, R. J., J. P. Yedler, E. B. Inou, R. D. Jackson, M. B. Blumhail, and E. Gerdineau, 1977: An evaluation of total solar reflectance and spectral band mixing techniques for estimating soil water content. *Journal of Geophysical Research*, 82(11): 2191-2194.

- Roberts, A. J. and C. L. Wignall, 1977. Densifying vegetation from satellite ground. *Photogrammetry Engineering and Remote Sensing* 43: 1344-1352.
- Rosenberg, N. J., B. L. Blad, and S. B. Verma, 1983. *Microclimate - The Biological Environment*. John Wiley and Sons, New York, pp. 489.
- Saltzman, J. W. and D. M. D'Arcy, 1982. Recovery of terrestrial mammals in the 4-14  $\mu$ m atmospheric windows. *Remote Sensing of Environment* 42: 81-104.
- Saunders, R. W., 1984. An automated scheme for removal of cloud contamination from AVHRR radiances over western Europe. *International Journal of Remote Sensing* 7(7): 847-864.
- Saunders, R. W. and E. T. Riedel, 1988. An improved method for detecting clear sky and cloudy radiances from AVHRR data. *International Journal of Remote Sensing* 13: 1487-1509.
- Schmugge, T. J. 1986. Remote Sensing of surface soil moisture. *Journal of Applied Meteorology* 25: 1149-1159.
- Schmugge, T. J. and P. Eagles, 1991. Remote sensing observations for the monitoring of land surface fluxes and water budgets. In *Land Surface Experiments: Measurement and Parameterization* (T. J. Schmugge and J. Adler, editors). Springer-Verlag, New York, pp. 217-238.
- Schmidt, A., 1978. *The TIROS-N/NOAA A/G Satellite Series*. NOAA Technical Memorandum NESG 54. U.S. Department of Commerce, NOAA/NESDIS, Washington, DC.
- Scott, N. A. and A. Chedin, 1981. A fast line by line method for atmospheric absorption computation, the concentration of atmospheric absorptions "ml". *Journal of Applied Meteorology*, 20: 820-832.
- Segin, B., and B. Tiesi, 1980. Using midday surface temperature to estimate daily evaporation from satellite thermal IR data. *International Journal of Remote Sensing* 4: 771-783.
- Segin, B., E. Asad, J. P. Richey, J. Anderson, V. Kari, and J. P. Lagarias, 1985. Use of meteorological satellites for water balance monitoring in Sahelian regions. *International Journal of Remote Sensing* 10: 1104-1117.
- Segin, B., D. Cornsby, and M. Gaud' 1984. Surface temperature and evaporation from local to regional scale. *Remote Sensing of Environment* 46: 287-305.

- Sellers, P. J., P. G. Hall, G. Asner, D. B. Stednick, & E. Shugart, 1989. The First GLEJOP Field Experiment (GLEJOP): Bulletin of the American Meteorological Society, 70(1):22-27.
- Sellers, Y. Y., 1987. Estimation of the evapotranspiration using surface and satellite data. *International Journal of Remote Sensing*, 8(10):1547-1562.
- Shib, S. F., 1981. Evapotranspiration as related to climatic factors in south Florida. *Florida Scientist*, 44(2):109-118.
- Shib, S. F., and G. Gueche, 1983. Water requirement for sugar cane production. *Transactions of American Society of Agricultural Engineering*, 26(4):804-807.
- Shib, S. F. and G. S. Shib, 1983. Pan evaporation as related to sugarcane leaf area index. *Soil and Crop Science Society of Florida Proceedings*, 42:85-89.
- Shib, S. F., L. H. Allen, L. C. Hammond, J. W. Jones, J. S. Rogers, and A. G. Sengupta, 1983. Baseline water requirement estimation in southern Florida. *Transactions of American Society of Agricultural Engineering*, 26:165-168.
- Shib, S. F., 1983. Data requirement for evapotranspiration estimation. *Journal of Irrigation and Drainage Engineering, American Society of Civil Engineering*, 109(3):262-274.
- Shib, S. F., and C. H. Tao, 1988. The assessment of 18 and 19 Jan. 1987 drought in Florida using NOAA satellite AVHRR data. *Proceeding of Florida State Meteorology Society* (in press).
- Stokke, P., and V. Minnis, 1983. Influence of land-surface evapotranspiration on the earth's climate. *Science*, 215:1496-1500.
- Stullweber, W. J. 1983. *Evaporation: An Overview of Hydrology*, (D. R. Maidment, ed.), McGraw-Hill Inc., New York, pp. 4-1-4-31.
- Stullweber, W. J. and J. S. Wallace, 1985. Evaporation from sparse crops-An energy conservation theory. *Quarterly Journal of the Royal Meteorological Society*, 111:405-415.
- Suckale, T. R., M. M. Schreiner, and B. M. Voth, 1973. Diffuse reflectance algorithm for the pathway of solar radiation through leaves. *Agronomy Journal*, 45:273-283.
- Sugli, S. M., 1985. Remarks on the use of a Stefan-Boltzmann type relation for estimating surface temperatures. *International Journal of Remote Sensing*, 6(5):741-747.

- Smith, B. M., A. P. Crutwell, and A. F. Raza, 1985. The estimation of atmospheric corrections to microwave Q11 (only) data from the AVHRR, simulation using AIRSIS-2. *International Journal of Remote Sensing*, 6: 933-945.
- Soupiria, A. G., G. A. Clark, S. F. Eds, P. B. Zanatta, and D. S. Harrison, 1984. Characteristics of potential evapotranspiration in Florida. *Soil and Crop Science Society of Florida Proceedings*, 63: 40-46.
- Smith, R. C. G., and B. J. Choudhury, 1991. Analysis of normalized difference and surface temperature observations over cropland areas, Australia. *International Journal of Remote Sensing*, 12(10): 2023-2044.
- Solomon, J. A., C. Coll, and Y. Cavazos, 1986. Atmospheric correction for land surface temperature using NOAA-11 AVHRR channels 4 and 5. *Remote Sensing of Environment* 18: 19-24.
- Stewart, G. L., 1983. Comparison of Penman-Monteith, Shuttleworth-Wallace, and modified Priestley-Taylor evapotranspiration models for aridified regions in semiarid rangeland, *Water Resources Research* 19(5): 1279-1285.
- Stoner, E. R., and M. P. Elzinga (eds), 1980. *Physico-chemical, Soil and Subsoil Profile Reference Factor Characteristics of Unplowed Moist Soils*. USDA pub. CR-146171.
- Stewart, D. M., 1966. *Evapotranspiration from Governmental Properties in a Depleted Area of the Lake Wales Ridge, Florida*. Water-Resources Investigations Report 54-4244, U.S. Geological Survey, Tallahassee, Florida, 19pp.
- Tarbot, O. R., R. Howard and D. Vaid-Madjar, 1985. Evapotranspiration over an agricultural region using a surface flux-temperature model based on NOAA-AVHRR data. *Journal of Climate and Applied Meteorology*, 23: 104-107.
- Tanner, C. B. and W. L. Polzin, 1969. Potential evapotranspiration estimated by the approximate energy balance method of Penman. *Journal of Geophysical Research*, 69(10): 1895-1897.
- Tanner, B. D., M. S. Tanner, W. A. Dugas, E. C. Campbell, and B. L. Ebel, 1982. Evaluation of an operational eddy correlation system for evapotranspiration measurements in alfalfa in evapotranspiration. *American Society of Agricultural Engineering, Publication No. 14-25*.
- Tapley, J. B., 1981. Some climatological aspects of satellite-observed surface heating in Kansas. *Journal of Applied Meteorology*, 21: 20-27.

- Thom, A. S., 1975. *Moisture: Air and Heat Exchange of Plant Communities in Vegetation and the Atmosphere*, Vol. 1, Academic Press, London.
- Thornthwaite, C. W., and B. Holzman, 1959. The determination of evaporation from land and water surfaces. *Monthly Weather Review*, 87: 4-11.
- Thornthwaite, H. A. M., and Stoyanovich, G. J. A., 1959. A simplified method to estimate regional 24h evapotranspiration from thermal infrared data. *Remote Sensing of Environment*, 3: 121-125.
- Townsend, J. R. G., and Aronson, C. G., 1969. Selecting the spectral radiation of satellite sensors required for global monitoring of land transformations. *International Journal of Remote Sensing*, 9(2): 187-226.
- Tucker, C. J. and E. S. Maxwell, 1970. Remote sensing for monitoring vegetation changes. *Photogrammetric Engineering and Remote Sensing*, 42: 1286-1302.
- Tucker, C. J., B. M. Holben, J. H. Egan, and J. E. McElroy, 1981. Remote sensing of total dry matter accumulation in winter wheat. *Remote Sensing of Environment*, 11: 171-189.
- Yamada, M., S. R. Wiers, B. Bernard, and J. L. Harbeck, 1982. Spatial variability of surface temperatures along two instrumented lakes and. *Water Resources Research*, 18, 1673-1684.
- Van de Grand, A. A., P. J. Canfield, and R. J. Garney, 1985. Determination of soil physical parameters, thermal inertia, and soil moisture from thermal surface temperature fluctuations. *Water Resources Research*, 21: 993-1009.
- Van de Grand, A. A., M. Owe, M. Cohen, and M. P. Smith, 1986. Measurement and spatial variation of thermal infrared surface emissivity in a semiarid environment. *Water Resources Research*, 22(2): 271-279.
- Van de Grand, A. A., and M. Owe, 1990. On the relationship between thermal emissivity and the normalized difference vegetation index for natural surfaces. *International Journal of Remote Sensing*, 10(8): 1119-1121.
- Yild, A. and A. Piner, 1989. Analysis of a simplified relation for estimating daily evapotranspiration from satellite thermal IR data. *International Journal of Remote Sensing*, 9(3): 1023-1037.

- Vidal, A. and A. Ferrat: 1990, Irrigation monitoring by following the water balance from NOAA-AVHRR thermal infrared data. *IEEE Transactions on Geoscience and Remote Sensing* 28(2) 166-174.
- Warren, H. L., E. P. Weeks, G. S. Campbell, D. I. Sacknerd, and B. B. Turner: 1986, Photosynthetic water use measured by eddy correlation methods. *Proceedings of Water Forum 1986*, American Society of Civil Engineering, pp 317-324.
- Wegst, F. J. and J. T. Chang: 1983, Evapotranspiration from agricultural surfaces: a first approach for short term numerical weather prediction. *Monthly Weather Review* 111 600-611.
- Whittingham, C. P.: 1974, *The biochemistry of Photosynthesis*, Edward Arnold, London.
- Wendisch, C. B. and Strickler, A. B.: 1987, The factor of scale in remote sensing. *Remote Sensing of Environment* 20 311-322.
- Wentley, J. T.: 1979, Reflection and transmission of light by leaves. *Plant Physiology* 47 634-637.
- Wright, J. L.: 1981, New evapotranspiration crop coefficients. *Journal of Irrigation and Drainage Division ASCE*, 106(IR2) 73-74.
- Wyck, J. E., P. A. Bova and A. Graetz: 1987, Estimation of broad-band planetary albedo from operational satellite-based radiation measurements, *NOAA Technical Report NC356* 21, U.S. Dept. of Commerce, Washington, DC: 10pp.
- Yeh, T. C., E. T. Wehnerhoff and S. Masebe: 1984, The effect of soil moisture on the short term climate and hydrology changes-a numerical experiment. *Monthly Weather Review* 112 474-490.

## BIOGRAPHICAL SKETCH

Chih-Hung Yen was born in Taipei, Taiwan, in 1963. He attended Chien Kuo High School in Taipei, Taiwan. He has earned a Bachelor of Science degree in agricultural engineering at the National Taiwan University. After two years of military service, he attended graduate school at the National Taiwan University and earned a Master of Science degree in agricultural engineering in 1990.

He started his Ph.D. studies with a major in the agricultural engineering and a minor in crop processing in the Agricultural and Biological Engineering Department at the University of Florida in August 1990. His research interests include water and natural resources, remote sensing applications, and geographic information systems.

I certify that I have read this study and that in my opinion it conforms to acceptable standards of scholarly presentation and is fully adequate, in scope and quality, as a dissertation for the degree of Doctor of Philosophy.

  
\_\_\_\_\_  
Van F. Smith, Chairman  
Professor of Agricultural and Biological  
Engineering

I certify that I have read this study and that in my opinion it conforms to acceptable standards of scholarly presentation and is fully adequate, in scope and quality, as a dissertation for the degree of Doctor of Philosophy.

  
\_\_\_\_\_  
Allan R. Overman  
Professor of Agricultural and Biological  
Engineering

I certify that I have read this study and that in my opinion it conforms to acceptable standards of scholarly presentation and is fully adequate, in scope and quality, as a dissertation for the degree of Doctor of Philosophy.

  
\_\_\_\_\_  
Brian J. Boman  
Associate Professor of Agricultural and  
Biological Engineering

I certify that I have read this study and that in my opinion it conforms to acceptable standards of scholarly presentation and is fully adequate, in scope and quality, as a dissertation for the degree of Doctor of Philosophy.

  
\_\_\_\_\_  
Bryan C. Smith  
Professor of Civil Engineering



I certify that I have read this study and that in my opinion it conforms to acceptable standards of scholarly presentation and is fully adequate, in scope and quality, as a dissertation for the degree of Doctor of Philosophy

  
George H. Meyer  
Professor of Soil and Water Science

This dissertation was submitted to the Graduate Faculty of the College of Engineering and to the Graduate School and was accepted as partial fulfillment of the requirements for the degree of Doctor of Philosophy

May, 1998

  
Richard M. Phillips  
Dean, College of Engineering  
Karen A. Holbrook  
Dean, Graduate School